ON DISENGAGING A PEG FROM A HOLE

by

JOEY ZHONG YI LIM

A thesis submitted to the University of Birmingham for the degree of
DOCTOR OF PHILOSOPHY

Department of Mechanical Engineering
School of Engineering
College of Engineering and Physical Sciences
University of Birmingham
March 2022

To my family.

Abstract

In the field of manufacturing and remanufacturing, robots are employed in assembly tasks. Robotics researchers often use a cylindrical peg and a cylindrical hole as a model to understand high-precision insertion operations. During those operations, two main obstacles were identified, namely, jamming and wedging. Jamming occurs when the force is applied in the wrong direction and can be rectified easily by changing the direction. Wedging occurs when the peg appears to be stuck in the hole. The wedging of a peg is more complex than jamming, and it involves the deformation of the components. Many studies have been performed in the area of peg-hole assembly. Although researchers have mentioned the necessary conditions for wedging, the peg-hole jamming problem was the main focus.

This thesis aims to better understand the peg-hole wedging problem to find methods to dislodge a wedged peg and to design a remote-centre-compliance (RCC) device to avoid the wedging and jamming of a peg that can be used in both assembly and disassembly. Using the definition and necessary conditions of peg-hole wedging, the systematic process of wedging a peg is analysed and illustrated. There are four steps to wedge a peg in a hole. First, the peg and hole must be in 2-point contact, and the two contact points must be within each other's friction cone. A force or moment is then applied to deform the peg and hole, and the peg tilting angle increases. The force or moment is then released in the third step, and the peg tilting angle will be reduced by a small amount. Finally, when the peg tilting angle reduces, the reaction forces at the contact points will be collinear, and the peg is wedged. In the simulation and experiment in this research, the hole is divided into two sides, and a force-torque (FT)

sensor is installed beneath each hole. The readings obtained from the sensors have shown that the hypothesis of the wedging process is correct, and when the peg is successfully wedged, the resultant force experienced by the FT sensors is balanced.

The dislodging of a peg is also investigated in this thesis. To dislodge a wedged peg, intuitively, the peg is either shaken, twisted or knocked. Depending on the application, some would use a low force to dislodge the wedged peg to avoid damaging the components, while others would prefer a quicker disassembly process. In this investigation, the wedged peg is dislodged using different methods, such as applying a constant force and pulsating forces with different frequencies and magnitudes. The time needed to dislodge the peg is recorded to compare the effects of different combinations of parameters used. The result from the simulation shows that the peg can be dislodged at low impulses within a specific range of pulling force magnitudes. Adopting a pulsating force helps reduce the impulse required to dislodge the peg compared to using continuous force in the low magnitude region. However, in the lowest magnitude region, using a continuous force resulted in a lower impulse as the time for dislodging the peg was shorter compared to when a pulsating force was employed.

Many techniques have been proposed and investigated to aid the peg-hole assembly process, and one of them is by using an RCC. At the University of Canterbury (New Zealand), researchers designed a passive compliant device, which was an inverted Gough-Whitehall-Stewart mechanism, to assist the peg-hole insertion process. This thesis analyses a modified version of that compliant device, where the legs do not meet in pairs at the platform but at points located remotely from it. This allows the device to have the features of an RCC mechanism, which has been proven by other researchers to be effective for precise peg-hole

assembly tasks. This device is also suitable for both assembly and disassembly processes. Unlike the currently available RCC design, which can only withstand high compressive forces, the proposed compliant device can resist both compressive and tensile forces. The compliance matrix of the new design and the location at which it is diagonal are derived using small approximations, proving that the centre of compliance is situated away from the platform. The correctness of the small motion assumptions and the RCC properties of the new compliance device have been confirmed by performing the sensitivity analysis.

Acknowledgement

First of all, I would like to thank my supervisor Prof. Duc Truong Pham OBE, Chance Professor of Engineering and Director of Research at the University of Birmingham, for his patient guidance, lavish encouragements and the opportunity to pursue my PhD research. He was my inspiration to continue my studies on the subject of peg-hole problem after my Masters in Engineering Degree. When I was doing my final year project in 2016-17, he was also my supervisor then. I was surprised when he mentioned that a simple peg and hole has been a popular research topic for over half a century. His professional and wise advice has always been useful to my research and it broaden my horizons.

I would also like to thank everyone in the Autoreman Group, including the Under-Grad students who assisted me in many forms: exchanging ideas, providing constructive criticism and helping me to obtain my components for my experiments.

Last and most importantly, I would like to express my utmost gratitude my parents and my family for all their support, morally and financially, throughout my PhD.

Contents

List of Figures

List of Tables

List of symbols

b	Length of base plate
C	Flexibility constant
$[C]$	Flexibility matrix
D	Hole diameter
d	Peg diameter
$\Delta\vec{d}$	Displacement of the wrist plate in the global coordinate system
F_{NA}	Normal force at Point A
$F_{\mu A}$	Friction force at Point A
F_{NB}	Normal force at Point B
$F_{\mu B}$	Friction force at Point B
F_R	Resultant force
F_x	Force acting along the x-axis
F_y	Force acting along the y-axis
F_z	Force acting along the z-axis
f	Frequency

h	Height of the RCC device
$[I]$	Identity matrix
k	Spring constant
L	Length of peg
l	Length of the link
Δl	Small change in the length of link
$\overrightarrow{\Delta l}$	Local displacement vector
$l_{2p.Crit}$	Critical distance between 2 contact points
l_{2pMax}	Maximum distance between 2 contact points
l_{Crit}	Critical peg insertion depth
l_d	Peg insertion depth
l_{ext}	Length of the external of the peg
l_{Max}	Maximum peg insertion depth
M_x	Moment acting about the x-axis
M_y	Moment acting about the y-axis
M_z	Moment acting about the z-axis

$[S]$	Global stiffness matrix.
$[s]$	Local stiffness matrix
x	Translation along the x-axis
y	Translation along the y-axis
z	Translation along the z-axis
θ	Peg tilting angle
θ_{Crit}	Critical peg tilting angle
θ_L	Link tilting angle
θ_{Max}	Maximum peg tilting angle
θ_x	Rotation about the x-axis
θ_y	Rotation about the y-axis
θ_z	Rotation about the z-axis
μ	Coefficient of friction
φ	Maximum friction cone angle

Nomenclature

CAD	Computer-Aided Design
EoL	End of Life
FEA	Finite Element Analysis
FT	Force-Torque
I4.0	Industry 4.0
LITF	Leaf-type Isosceles-Trapezoidal Flexural
LVDT	Linear Variable Differential Transformers
MoL	Middle of Life
OEM	Original Equipment Manufacturer
PID	Proportional–Integral–Derivative
PLC	Programmable Logic Controller
RCC	Remote-centre-compliance

Chapter 1

Introduction

1.1 Background

Manufacturing as an organised industry started during the Industrial Revolution in the 18th century, and it began to flourish in the 2nd Industrial Revolution almost a century later, which provided a process framework for the future. However, with the help of machines, many of the processes still use the hand production method and are labour intensive. In the late 1960s, the invention of computers, electronics, programmable logic controllers (PLCs) and robots contributed to the 3rd Industrial Revolution, and many of the manufacturing processes can be automated and mass produced and even at lower cost. Nearly five decades later, I4.0, the 4th Industrial Revolution, comes, where machines and products are connected via the Internet (iED Team, 2019).

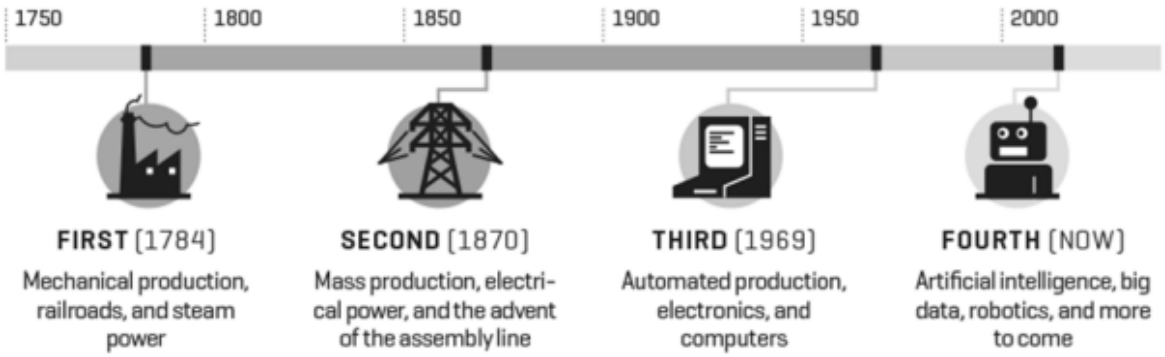

Figure 1-1. The four stages of industrial revolutions (Horvath, 2018)

In the older days, faulty parts of a product were repaired/replaced, and the product was refurbished if it was generally worn and continued to be used for as long as possible. With the advancement in technology, not only are Original Equipment Manufacturers (OEM) able to guarantee their products, but they can also estimate the life expectancy of their products, i.e., when its End-of-Life (EoL) would be. Once the product reaches its EoL, it can be remanufactured.

What is remanufacturing? There are many terms that are associated with remanufacturing: repair, reconditioning, reuse, and recycling (Amezquita, et al., 1995). According to the British Standard, remanufacturing is "a process of returning a used product to at least its original performance with a warranty that is equivalent (to) or better than of the newly manufactured product" (British Standard Institute , 2010). Figure 1-2 shows a comparison of the product lifecycle process, which involves reuse, remanufacturing and recycling.

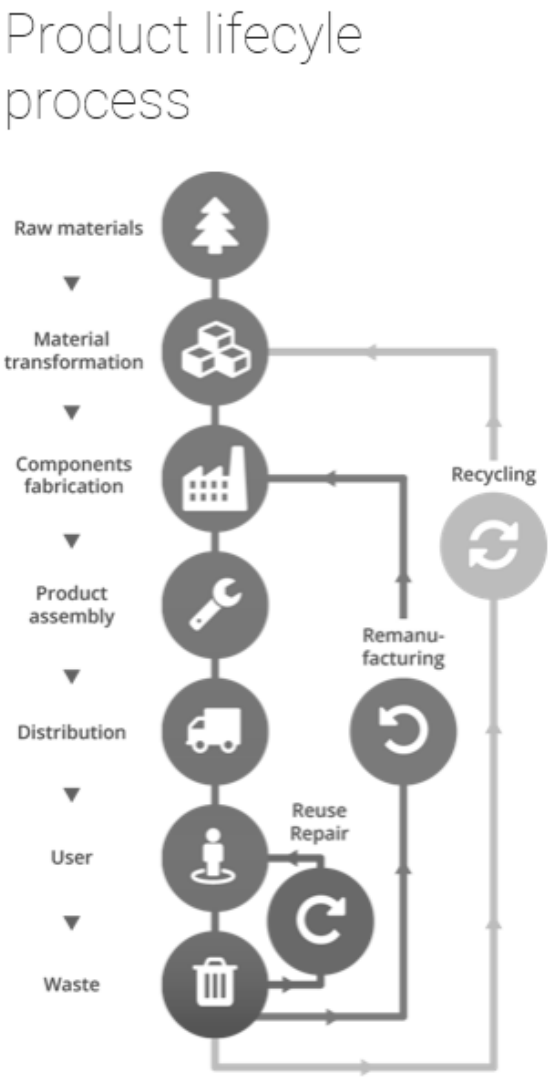

Figure 1-2. The product life cycle process (Hollins, 2020)

There are many benefits for remanufactured products that have reached their EoL. Remanufacturing plays a critical role in sustaining the environment; it releases less carbon emissions, uses less raw material and retains approximately 85% of its initial value. Remanufacturing only requires 20%-25% of the energy required to manufacture the same

product (Colledani, et al., 2014). By doing so, the cost of remanufactured products will be cheaper compared to a newly manufactured one (Ijomah, et al., 2004).

In manufacturing, the process uniformly handles new parts. On the other hand, in remanufacturing, the EoL products received will be in various conditions depending on how they have been used. These uncertainties are the main challenge in remanufacturing, as they complicate the process and require intensive human labour to handle them. Using the Middle of Life (MoL) data may help with failure diagnostics and decisions on repair or replacement products (Kerin & Pham, 2019). Additionally, greater product and process information can be shared at the shop floor level in remanufacturing with the aid of I4.0 technologies; however, the accuracy, timeliness, and completeness of the data have yet to be managed appropriately (Kerin & Pham, 2020).

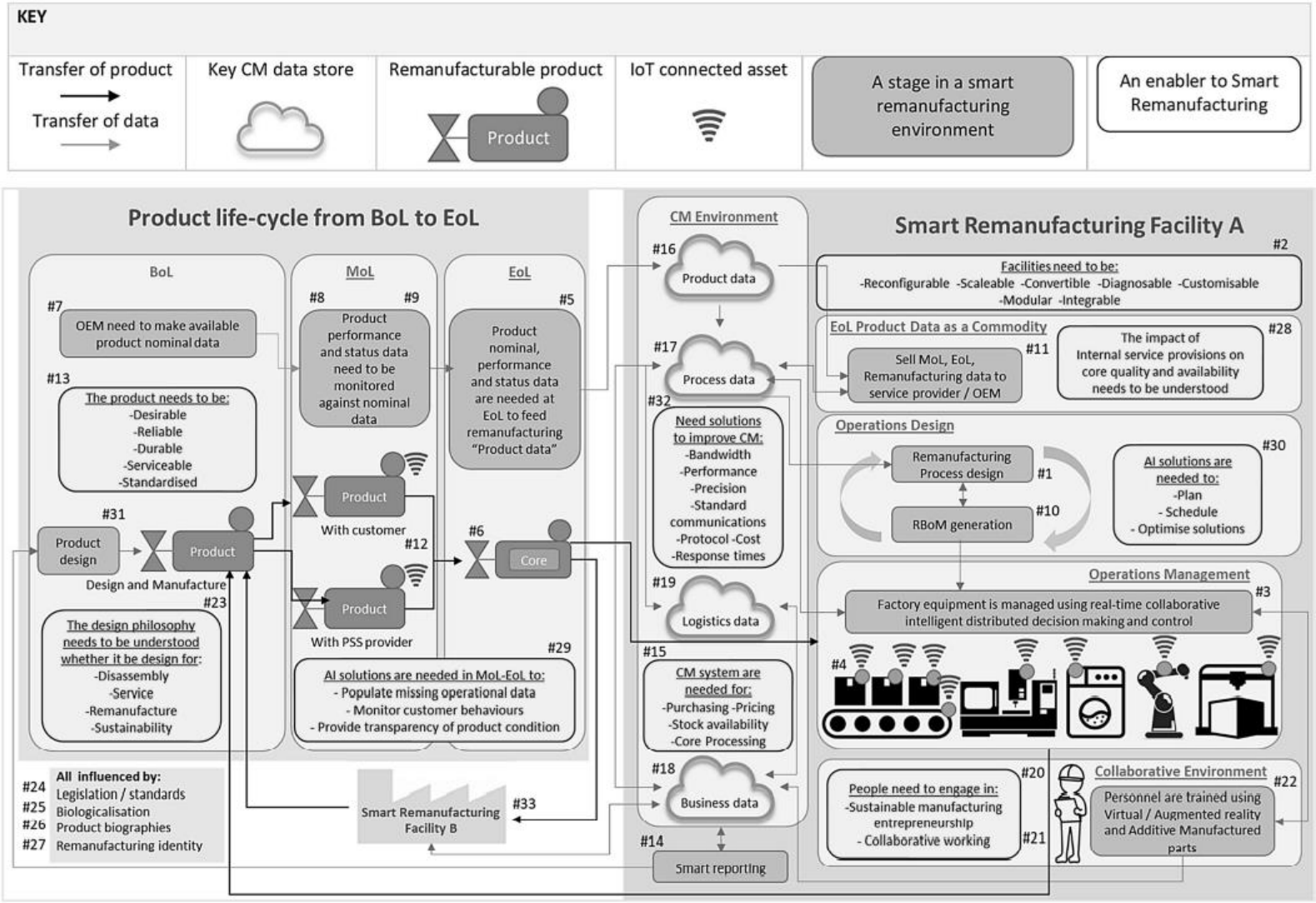

Figure 1-3. *Proposed framework for I4.0 in remanufacturing for the circular economy by (Kerin & Pham, 2020)*

The assembly of parts is the final process in manufacturing a product. It has been a topic of research since the 1960s. Many researchers have been investigating ways to improve the assembly process and to make the system more efficient. Such techniques include FT sensor feedback, the use of compliant devices, machine learning and algorithms, product design, etc. In regard to remanufacturing, there is another key task needed: disassembly. Without disassembly, remanufacturing cannot proceed.

The simplest assembly and disassembly operation can be modelled as the insertion of a peg into a hole or the withdrawal of a peg from a hole. Two common challenges are encountered in peg-hole assembly and disassembly, namely, jamming and wedging. The jamming of a peg occurs when the force is applied in an incorrect direction, and it can be rectified easily by redirecting the force. The wedging of a peg, in layman's terms, is when the peg is 'stuck' in the hole, and it is a more complex problem. Using an old wooden drawer as an example, when the drawer is not drawn properly, it will get stuck, and a certain amount of force is required to dislodge it. Many investigations have been published on the topic of jamming, especially in peg-hole assembly, but only a handful can be found on wedging.

On the other hand, when parts are stuck together, there are many ways of dislodging them, including applying brute force, shaking, cutting, vibration, etc. Depending on the nature of the process, different disassembly methods are used; for example, destructive disassembly is more suitable for material recycling, and non-destructive disassembly is more suitable for product remanufacturing.

There are three types of misalignments for peg-hole insertion and extraction that will lead to jamming and wedging of the peg: lateral misalignment, angular misalignment, and a combination of both.

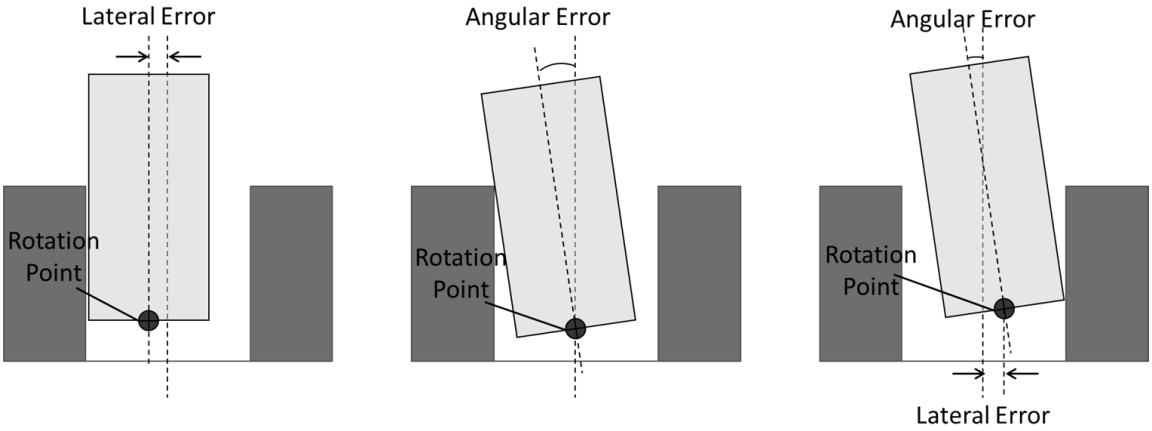

Figure 1-4. The three types of misalignments of the peg

Under normal circumstances, the end effector of the robot or machine grips onto the peg in a rigid manner. One of the solutions to deal with the misalignments is by using a compliant device on the end effector of the robot or machine. The compliant device is able to absorb the misalignments, which gives freedom to the peg and allows the peg to correct its orientation. There are a handful of designs for compliant devices, but the most popular is the RCC Device.

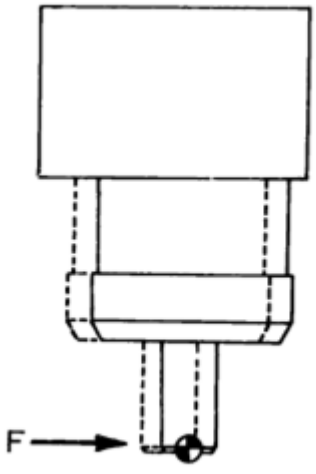

Figure 1-5. Desired response of the compliance system to applied force (Drake, 1977)

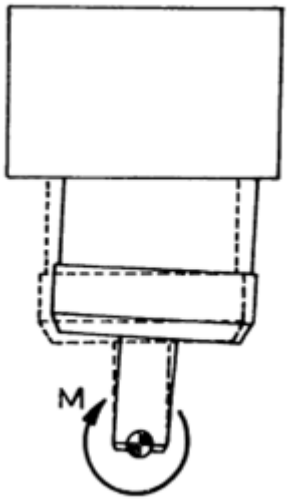

Figure 1-6. Desired response of the compliance system to an applied moment (Drake, 1977)

Having the compliance centre remote and at the tip of the peg, the RCC device is able to manoeuvre the peg to minimise misalignments. When the tip of the peg is in contact with

the chamfer of the hole, a force will be transferred through the centre of compliance, which causes the translation of the peg. As the peg is inserted deeper into the hole, the contact forces will result in a moment about the centre of compliance that rotates the peg about the centre. Figure 1-5 and Figure 1-6 show the behaviour of the peg when a force and moment are applied to the centre of compliance.

1.1 Aim and Objectives

The aim of this research was to better understand the problem of peg-hole wedging in disassembly and find ways to avoid it. The objectives were as follows:

1. To define a systematic process of wedging a peg.
2. To investigate the parameters that produce low impulses to dislodge a peg.
3. To observe the time taken to dislodge the peg.
4. To design an RCC device for peg-hole assembly and disassembly.
5. To develop a simplified theoretical model for the RCC device.
6. To analyse the sensitivity of the RCC device theoretical model.

1.2 Outline of the thesis

Chapter 1 gives an overall introduction to remanufacturing and the aim and objectives of this research.

Chapter 2 reviews the literature on peg-hole assembly and disassembly, which includes the techniques and tools used to avoid peg-hole jamming and wedging problems. From this review, the research agenda is proposed.

Chapter 3 demonstrates a systematic approach to wedging a peg in a hole when the necessary conditions are fulfilled. The simulations carried out illustrate the wedging process in detail and are then proven by experiments.

Chapter 4 describes the investigation of dislodging a peg using impulses with different frequencies. The study was carried out through simulation, and the time taken to dislodge the peg was observed.

Chapter 5 shows the derivation of a simplified RCC device model using the approximation method. The design of the RCC device is a modification of the design in (McCallion, et al., 1979). Analyses were carried out to examine the sensitivity of the model.

Chapter 6 concludes the thesis and provides suggestions for further research.

Chapter 2

Literature Review

2.1 Preliminaries

Assembly and disassembly are key operations in manufacturing and remanufacturing. To achieve high productivity, these repetitive tasks are assigned to robots to perform. However, two possible problems might occur during these processes: jamming and wedging of parts. These are caused by three types of misalignments: lateral misalignment, angular misalignment and a combination of both. The insertion of a peg into a hole or the withdrawal of a peg from a hole has been used as proxies of real assembly and disassembly operations to investigate jamming and wedging problems.

As already mentioned, the misalignment of the peg will lead to peg jamming and wedging. Jamming is caused by ill-proportioned forces applied on the peg. On the other hand, wedging is different from jamming and is a geometrical problem where the reaction forces of the contact points are collinear (Simunovic, 1979). In layman's terms, wedging is a phenomenon where a peg is "stuck" in a hole. According to Simunovic (1979), wedging is

defined as the condition where the reaction forces at the contact points are nonzero in the absence of an externally applied force. This chapter reviews the literature on peg-hole assembly and disassembly and covers the techniques and tools used to avoid peg-hole jamming and wedging problems.

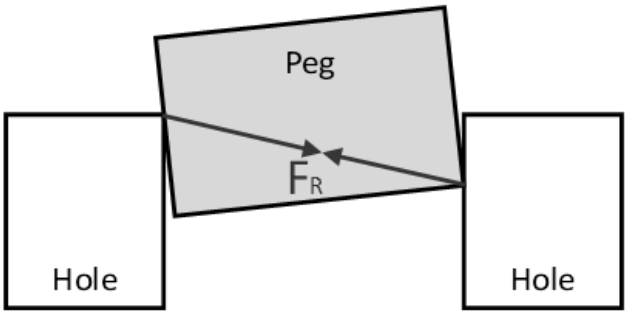

Figure 2-1. Notation of reaction force when the peg is wedged

2.2 The peg-hole contact problem.

Many methods have been investigated by researchers to aid the process of peg-hole assembly and disassembly. First, the contact problem must be considered. (Liao & Leu, 1998) utilised Lagrange's impact model to generate a general form of impact equations for robots when carrying out peg-in-hole assembly. The impact equation shows how the parameters of the system influence the force impulse and departure peg angle. The problem of contact impulse forces has also been considered by (Haskiya, et al., 1999) for peg hole insertion analysis. The optimum wrist stiffness was derived to overcome the contact forces, especially when the peg

is in three-point contact. The MATLAB-Simulink simulation results enabled the design and optimisation of peg-hole assembly strategies.

2.3 Using vision system in assembly and disassembly operations.

A vision system has been used in the process of peg-hole assembly and disassembly to increase the efficiency and success rate. (Weigl & Seitz, 1994) demonstrated a disassembly process with the aid of three cameras: one mobile camera attached to the robot arm to capture 3-D workspace information and two static cameras to guide the robot to plan a stable grasp for the gripper. A combination of sensors and vision systems has also been used by others. (Wang, et al., 2015) had a vision system for detection and localisation and a camera combined with three 1-D laser sensors to accurately measure the position and orientation of the hole. Similarly, (Zhao, et al., 2020) combined the vision system and FT sensor on a six-legged robot to perform peg hole insertion.

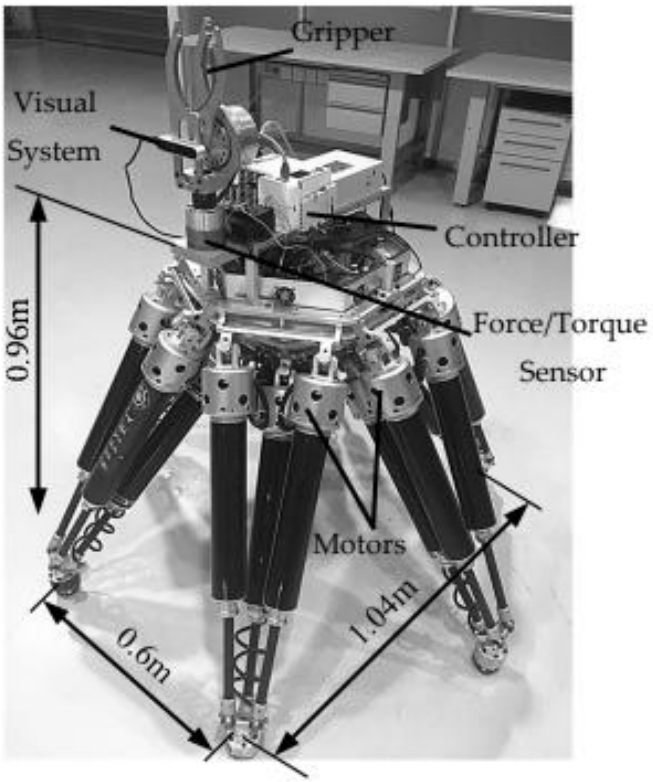

Figure 2-2. Prototype of the six-parallel-legged robot (Zhao, et al., 2020)

2.4 Using force-torque sensor in assembly and disassembly operations.

FT sensors play a crucial part in autonomous peg hole assembly and disassembly. (Tang, et al., 2016) demonstrated the alignment of robotic peg-hole assembly by analysing force and geometry and designing a compensation trajectory to avoid 3 contact points before insertion. By using the force feedback from the sensor, (Wang, et al., 2018) generated a prediction and

analysis model for the assembly of a large length-diameter ratio peg and hole. (Zhang, et al., 2019) presented control strategies for the flexible dual peg-hole insertion task by analysing the contact state, deriving the force-moment relationship and obtaining jamming states for different stages. Instead of inserting a peg in a hole, (Li, et al., 2020) have performed a spiral search motion whereby the tool (as the hole) engages onto the screwhead (as the peg). Merging the spiral search with active compliance and force sensing, the success rate is as high as 96.5%.

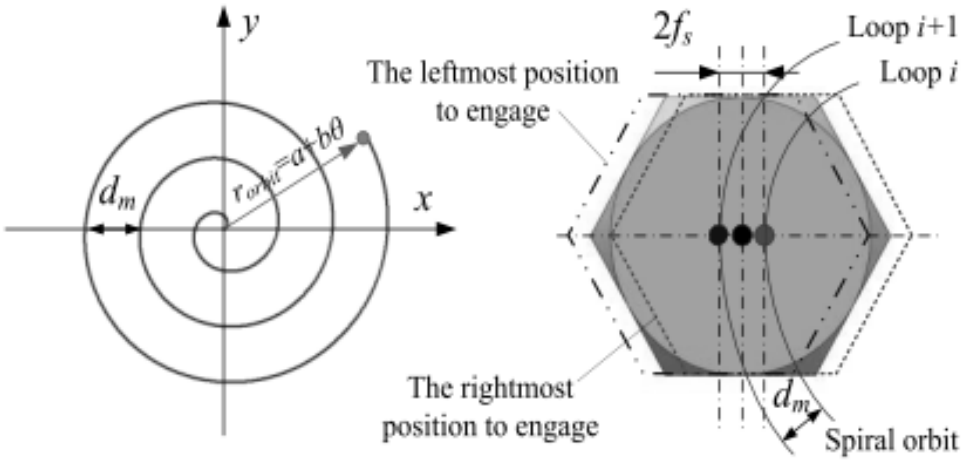

Figure 2-3. Maximum distance d_m between different circles of the spiral orbit (Li, et al., 2020)

2.5 Using machine learning in assembly and disassembly operations.

(Su, et al., 2012) utilised no sensors for inserting a crankshaft into a bearing, but with the help of cameras, the high-dimensional configuration space is reduced to a lower dimension subspace, and analysis is carried out on the attractive region. This will allow the robot to be manipulated within the configuration subspace.

The principle of remote centres is also applied in the field of medicine. Using a KUKA LWR4+ robot to perform the trajectory control of redundant robot manipulators during surgery, (Su, et al., 2020) improved a recurrent neural network (RNN) scheme to enable accurate task tracking that incorporates the constraints on the remote centre of motion (RCM). Another similar application can be found in (Begey, et al., 2020). There were two types of manipulation of the X-shaped tensegrity mechanisms: one is bar actuated; one is cable actuated. Both designs have shown satisfactory results.

Another type of neural network has also been used for assembly. First, (Jin, et al., 2021) perform a tilt-then-rotate motion on the peg to capture the contact patterns; then, the data are processed using a convolutional neural network (CNN) to locate the error direction. After that, the robot will insert the peg, and if it fails, the process repeats.

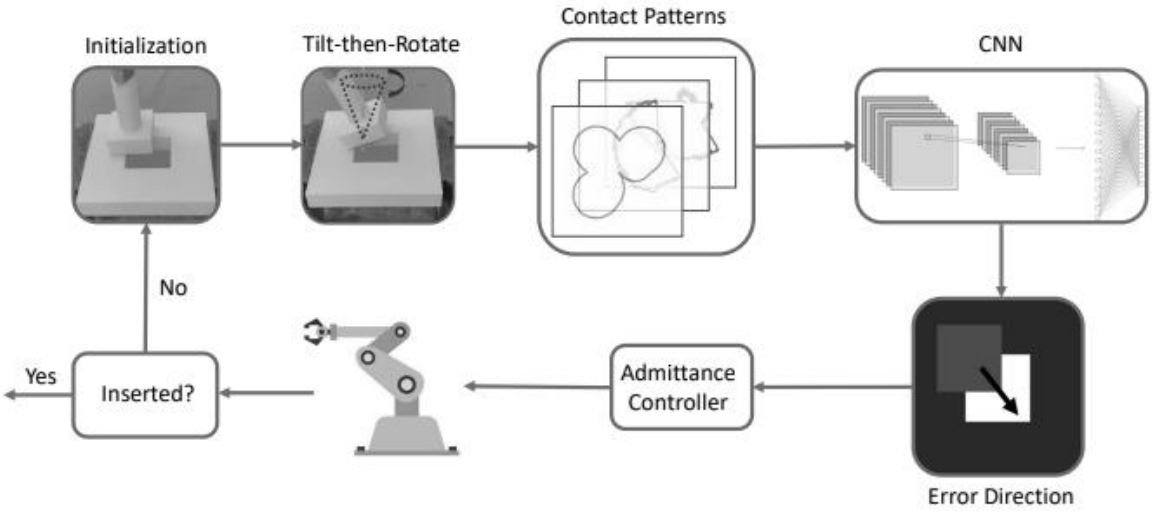

Figure 2-4. Framework of the proposed method (Jin, et al., 2021)

2.6 The interlocking of parts and disassembly sequence.

A common product consists of multiple parts and multiple “peg-in-hole” connections. Depending on the design of the product, there is more than one way of disassembling the components. Some products might have parts interlocking each other, and this is no longer a simple peg-hole insertion or extraction. The interlocking of parts also affects the sequence of disassembly. To find the relationship between interlocking components, (Wang, et al., 2020) have created a contact matrix, a space interference matrix and a relation matrix by using simple logic gates and the assembly matrix of the interlocking components. When failures occur during robotic disassembly, (Laili, et al., 2019) suggested a two-pointer detection strategy to detect the remaining subassemblies and components. Then, the disassembly

direction and order of the remaining subassemblies and components were incorporated with a ternary bee algorithm to generate a replanning disassembly solution.

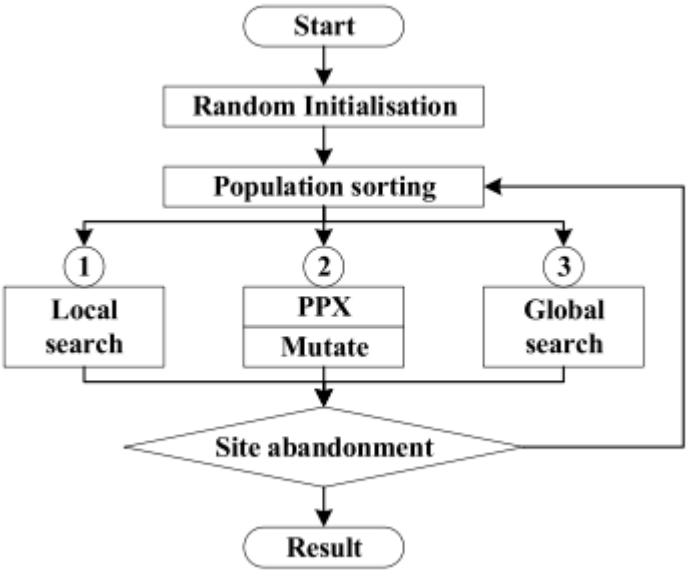

Figure 2-5. The mainframe of the ternary bee algorithm (Laili, et al., 2019)

2.7 Remote-centre-compliance systems.

Different modes of robot control can be used for peg-hole assembly and disassembly. (Chen, et al., 2009) investigated the use of a soft servo to carry out peg-hole insertion. This has the same effect as using an RCC or force control system, and it is less sensitive to environmental contact. However, this method is limited to small position error, and as a result, it generates a larger contact force compared to using the force control method.

(Wang, et al., 2019) designed an elastic displacement device that was integrated into the end effector of the robot. The displacement sensors in the elastic displacement device are connected to a signal converter and a programmable logic controller (PLC), which will process the change in displacement of the peg and feedback to the robot during a spiral search. The centre of compliance is variable by manipulating the elasticity of the spring.

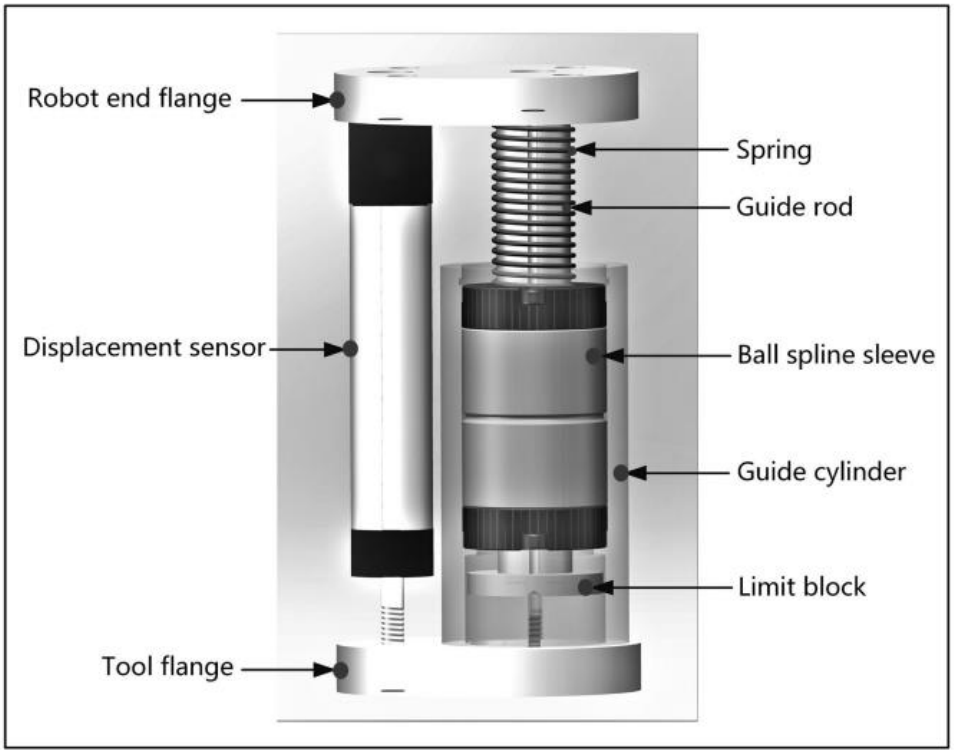

Figure 2-6. Elastexttic displacement device (Wang, et al., 2019)

Due to the rigidity of robots, compliant systems and devices were introduced to adapt the misalignment errors during peg-hole assembly and disassembly. (Drake, 1977) is one of the earliest studies that discussed the design and application of RCC. This compliant device is

able to yield lateral and rotational displacement in response to lateral forces and moments of peg during the insertion process. It is then able to correct the misalignment errors of the peg.

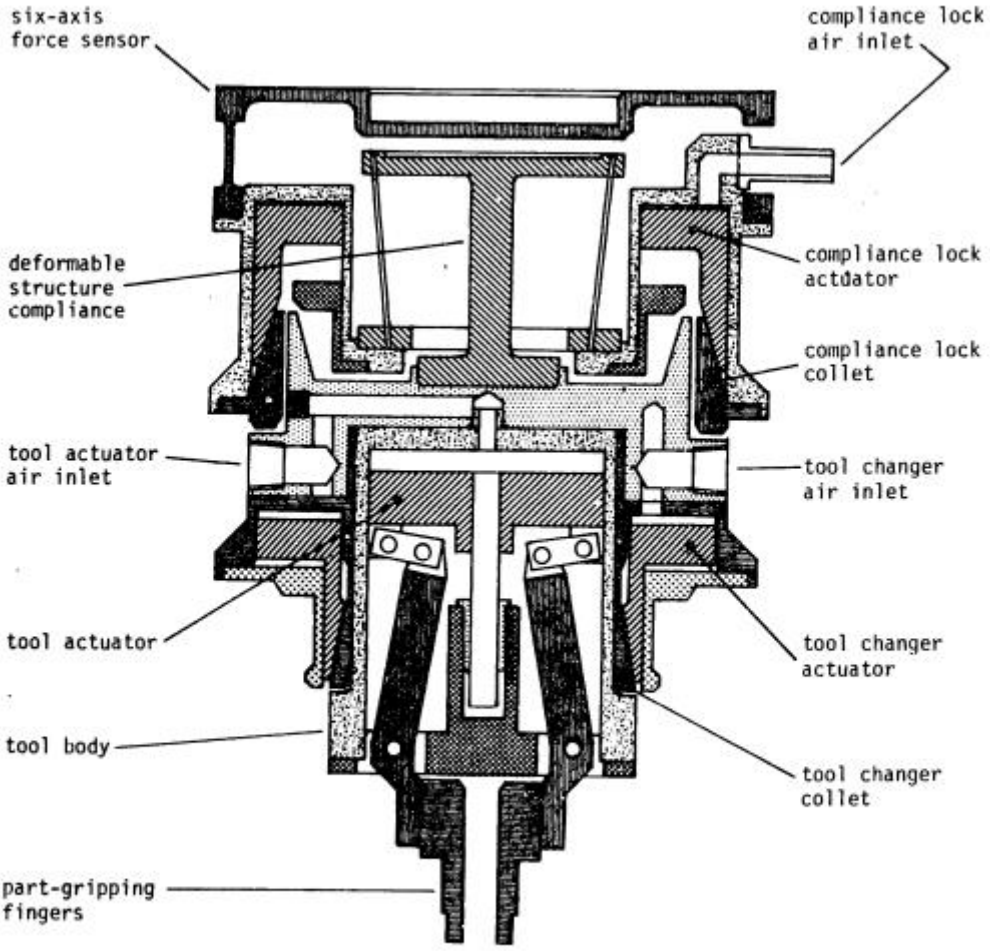

Figure 2-7. Cross-sectional drawing of complete compliance system (Drake, 1977)

Another design of the compliant device was created by (McCallion, et al., 1979). Similar to the Gough-Whitehall-Stewart Platform, it was constructed with six cylindrical links; however, the centre of compliance is on the device itself and not remote.

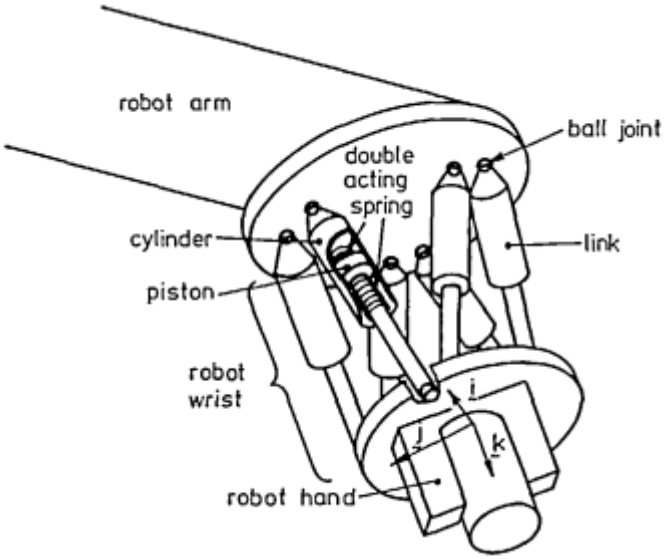

Figure 2-8. The insertion device as a robot's compliant wrist (McCallion, et al., 1979)

Unlike the conventional RCC, which only has one fixed remote centre with a predetermined stiffness, (Zhao & Wu, 1998) have developed a variable remote compliant centre (VRCC), which improves the flexibility and reliability in the assembly operation. The VRCC consists of a few components: optical-electronic sensors, electromagnetic drivers and computer control technology that controls the mechanical impedance.

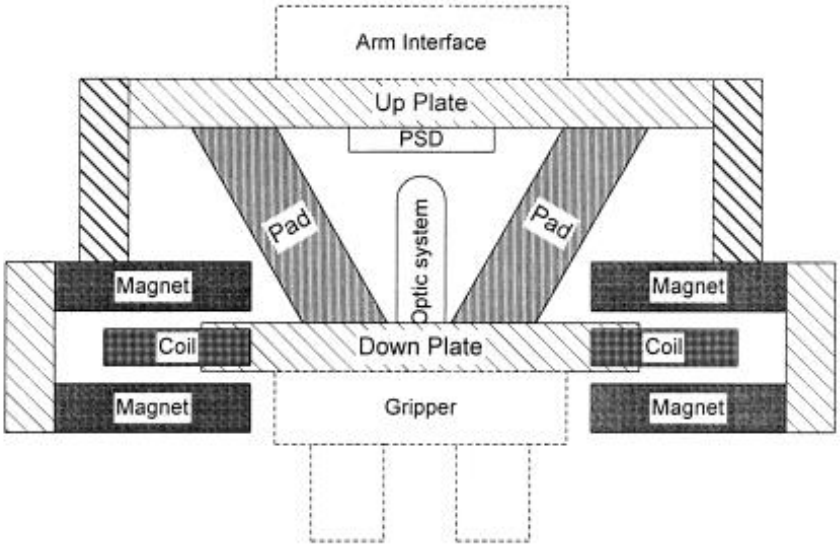

Figure 2-9. The mechanical body of the VRCC device in (Zhao & Wu, 1998)

The effects of compliance in peg-hole assembly have been studied by (Whitney, 1982). By studying the compliant support of the peg, the derived model was able to predict the possibility of jamming and the number of contact points. On the other hand, (Zhang, et al., 2019) investigated the same problem but for disassembly.

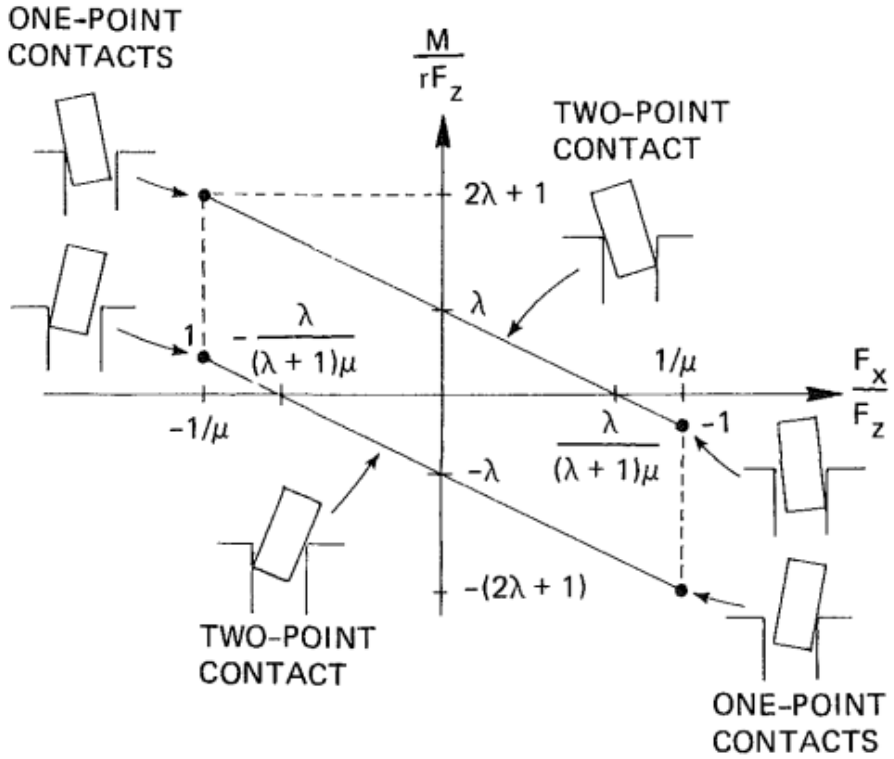

Figure 2-10. The jamming diagram (Whitney, 1982)

For many years, researchers have been looking at ways to improve the design of RCC devices. (Joo, et al., 1996) investigated the design of the Elastomer Shear Pads (ESP) of the RCC device to predict its mechanical behaviour. It was also recommended to have hinge/ball-jointed ESPs to enhance the performance of the ESPs.

At a smaller scale, a spatial remote centre of compliance mechanism has been designed and investigated for the use of micro/nanofabrication by (Lai, et al., 2013). The mechanism comprises two sets of leaf-type isosceles-trapezoidal flexural (LITF) arranged in a parallel manner, and the leaves are equally spaced at intervals of 90^o. An improved version of the device is proposed by (Lai & Zhu, 2016), whereby the leaf flexures have been changed into

round beams instead. The compliance factor is derived by generating the stiffness matrix in the rotational and compliance precision analysis.

A different approach has been taken to design an RCC device. (Liu & Wang, 2014) first began designing an RCC device by having a continuous circular structure as the link between the upper and lower plates, which was then optimised into a circular periodic structure, i.e., an RCC device with three links. These two designs were compared and studied, and the results show that the latter is a better design because it requires less material and is able to achieve lower stiffness.

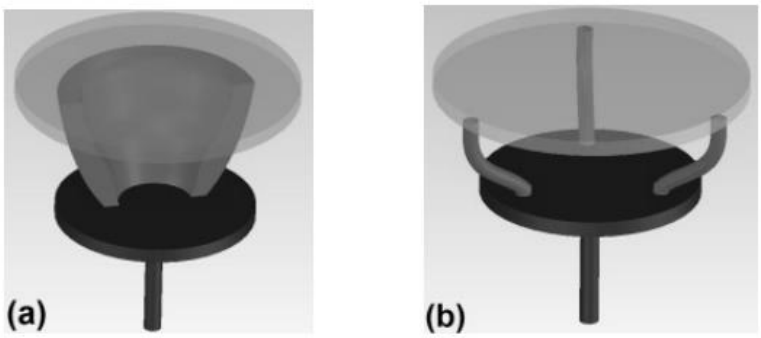

Figure 2-11. Realisation of the rotational symmetry property: (a) revolutionary symmetric structure (only half is shown); (b) circular periodic structure (Liu & Wang, 2014)

(Ciblak & Lipkin, 2003) carried out a thorough evaluation of the sensitivity of the distance between the elastic centre and geometrical centre. The findings suggested that for an RCC to perform at optimal, one should calculate and use the elastic centre instead of using the geometry.

Understanding the compensation had to be made by the RCC device for a repetitive operation allows the measurement of the misalignments of the peg. If trends can be observed from the measurement of misalignments, errors can be traced, and corrections can be made. (Park, et al., 2018) integrated a linear variable differential transformer (LVDT) sensor into each of the legs of the RCC device, and it measures the change in length of the legs. With that, the new position and orientation can be calculated using the simple kinematics equations. (Kim, et al., 2021) proposed another way of measuring the compliance of the RCC. There are three sets of triangle prism-shaped blocks with a pair of capacitive sensing printed circuit boards at the bottom of each prism block, which is constructed in the middle of the RCC and arranged circularly equally apart. Different types of translation and rotation misalignments between the two plates will result in different types of contact patterns of the prism blocks and the sensors.

Figure 2-12. The sensing printed circuit board grounded part of the developed sensor (Kim, et al., 2021)

The design of RCC has been further diversified to accommodate different peg lengths, which are normally called VRCC. The common way would be manipulating the links between the two plates of the RCC. (Lee, et al., 2000) designed rotational disk plates at the top and bottom of each ESP to alter its angle with respect to the vertical axis. With the distance between the plates being constant, the change in ESP tilting angle will affect the position of the compliance centre.

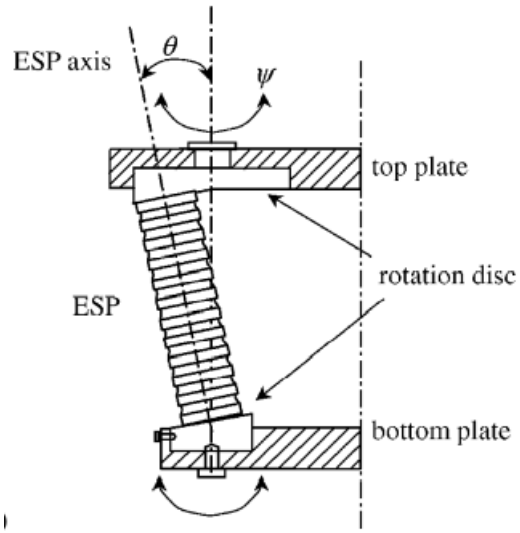

Figure 2-13. Cross-sectional view of the ESP in (Lee, et al., 2000)

(Choi, et al., 2001) introduced stiffness adjusters in the middle of the ESPs to clamp layers of the ESPs to limit the lateral stiffness of the RCC device. The position of the compliance centre is varied according to the number of EPS layers being clamped.

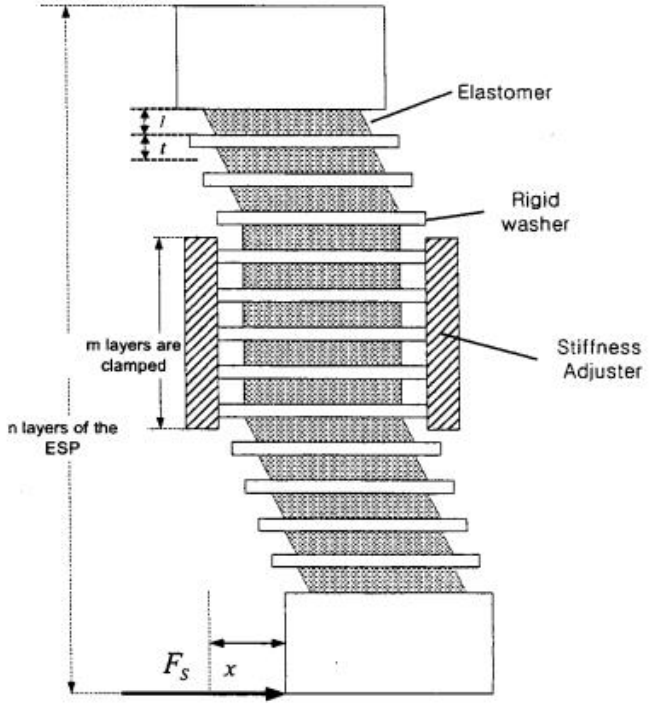

Figure 2-14. Using the stiffness adjuster to clamp the ESP (Choi, et al., 2001)

A similar approach was taken by (Lee, 2005), whereby the stiffness of the ESPs is controlled from the top end of the material. With a simple modification, a stiff rod is easily inserted into each ESP, limiting layers of the ESPs or even locking the device for other means.

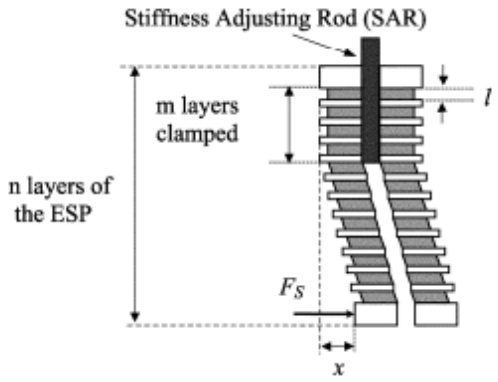

Figure 2-15. Deformation of the ESP with the Stiffness Adjusting Rod (Lee, 2005)

Another ESP shear control technique was studied by (Lee, 2009). The position of the top of the ESPs was made to be adjustable, changing the tilting angle of the axis of the ESPs, which varies the lateral and lateral coupling stiffness. A new type of RCC device link is developed by (Zhao, et al., 2021), which employs an electromagnetic variable stiffness spring, and the stiffness is controlled by adjusting the current of the coil of the electromagnetic spring.

There are also other methods of designing VRCCs. The idea of merging multiple RCC devices into one was proposed by (Park, et al., 2017). There were multiple sets of compliant bars, each set with different stiffnesses and lengths, and they could be engaged via different plates on top of the device, as shown in Figure 2-16. LVDTs are used to measure the displacement between the plates.

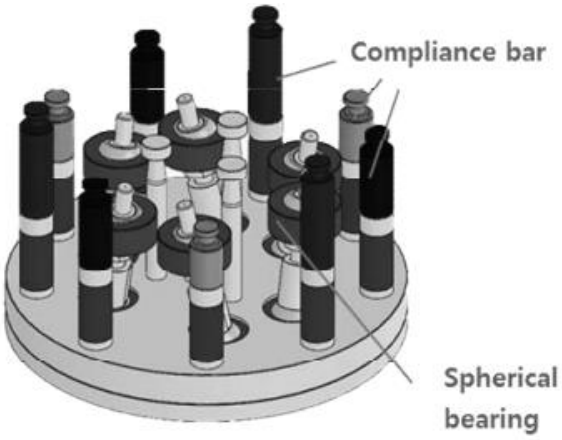

Figure 2-16. Composition of the compliance bar sets in (Park, et al., 2017)

The art Origami is also used in developing an RCC device. The structure of the RCC device designed by (Zhang, et al., 2020) consists of two elastic trapezoid four-bar linkages arranged orthogonally as the inner skeleton of the device, while the outer Origami shell provides torsion resistance. The stiffness is controlled by four sub pneumatic actuators in the skeleton. In contrast, (Bottero, et al., 2020) have taken the softer approach to make the stiffness of the device lower. The device is manipulated by controlling the fluid pressure in the chambers partitioned by a hyperelastic membrane, which allows the membrane to have a different grip on the piston.

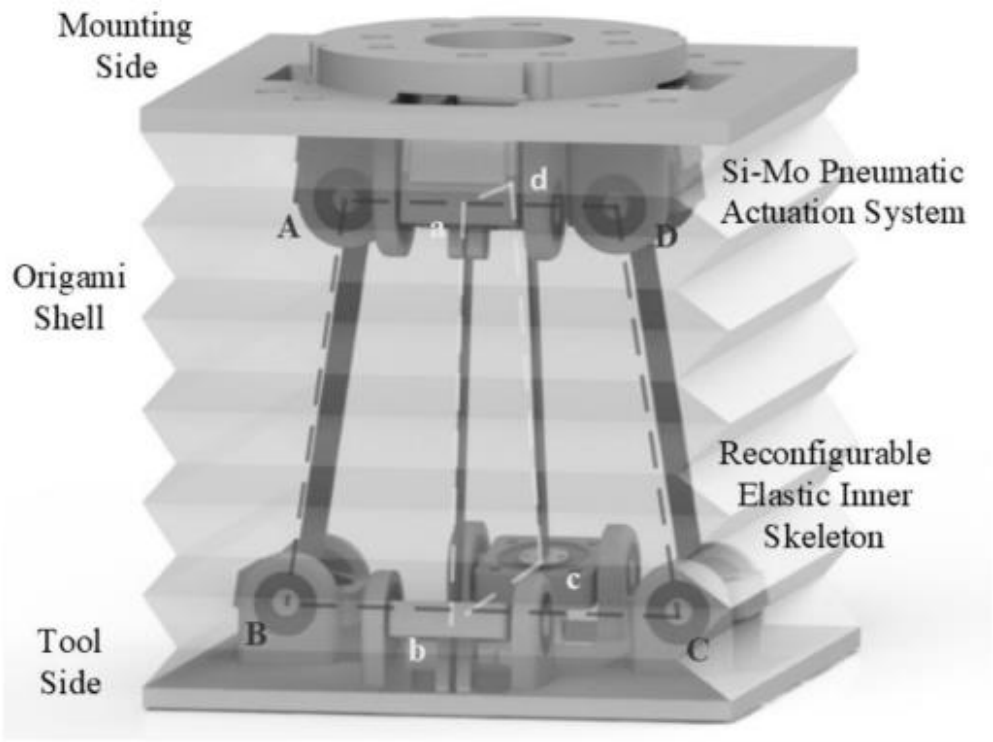

Figure 2-17. Structure of the proposed variable stiffness device in (Zhang, et al., 2020)

In 1947, Gough and Whitehall designed a machine and completed the prototype in 1955 at Dunlop Rubber Co., Birmingham, UK (Gallardo-Alvarado & Garcı´a-Murillo, 2012). The machine is called the Universal Tyre Test Machine (Gough & Whitehall, 1962).

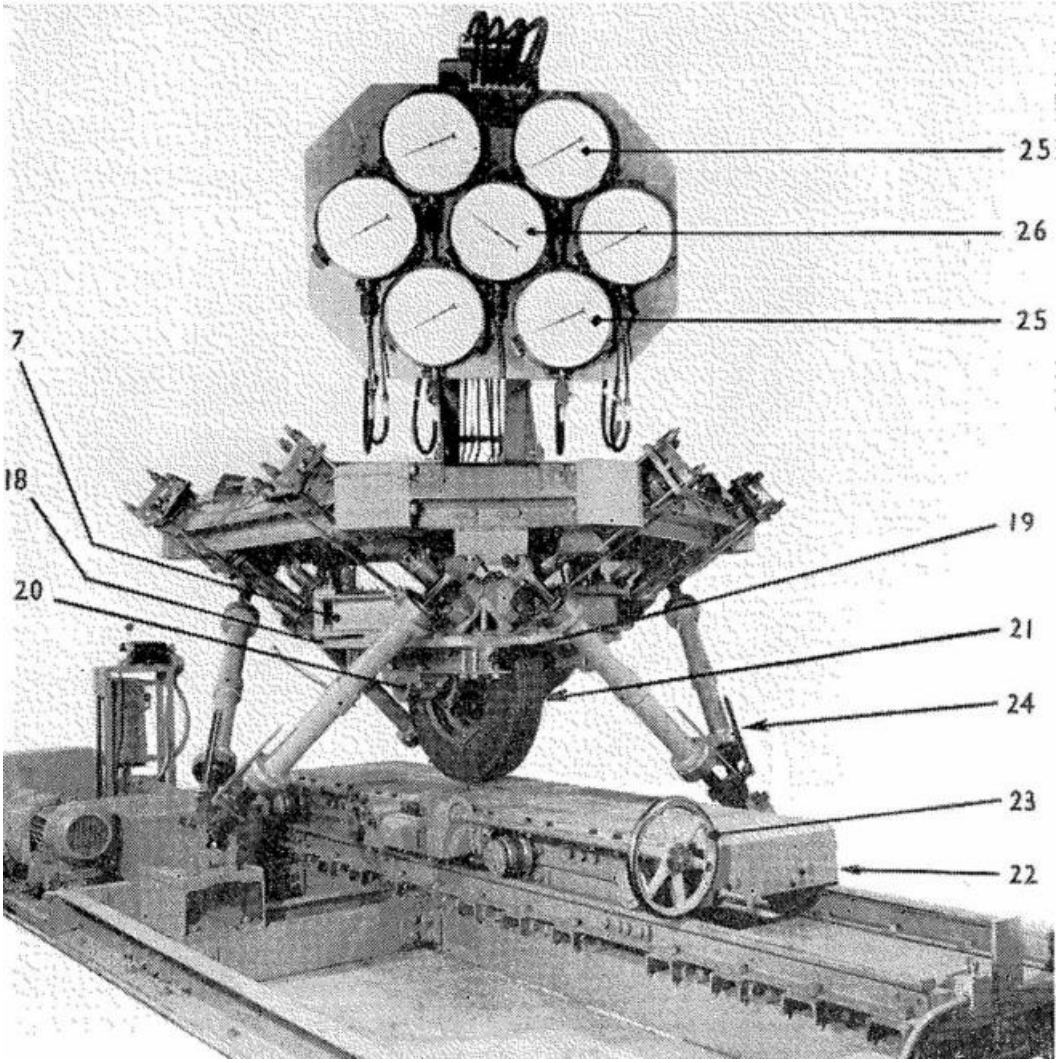

Figure 2-18. The Universal Tyre Testing Machine (Gough & Whitehall, 1962)

In 1966, Stewart devised a machine, unaware of the work done by Gough and Whitehall, to simulate flight conditions for pilot training for Elliott Automation Co. in Frimley, Hampshire, UK (Stewart, 1965). Although the principle of design is similar, the mechanisms are different (Fichter, et al., 2008) (Gallardo-Alvarado & Garcı´a-Murillo, 2012).

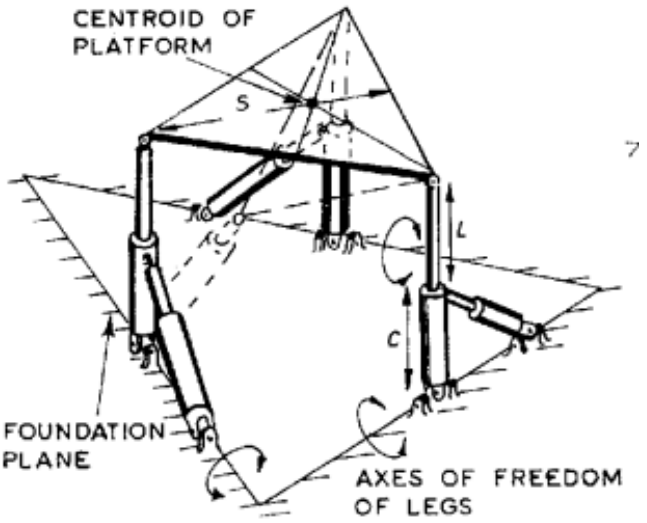

Figure 2-19. The arrangement of the Stewart Platform (Stewart, 1965)

This has inspired many works and research in the field of engineering. Like many researchers, (McCallion, et al., 1979) adapted the idea and designed the design of the Gough-Whitehall-Stewart mechanism. Using the approximation method, the theoretical model is simplified, where the relationships between compliance translations, rotations, forces, and moments are established and can be inversed directly.

Vibration is one of the popular methods used in peg-hole assembly. (Wohlert-Jensen, 1978) has modelled the equation of motion for peg-hole assembly under different scenarios: different types of contact, different peg diameter to length ratio, etc. Two spiral search strategies for peg-hole engagement in the assembly were proposed by (Katz & Wyk, 1997): circular and square spiral patterns. The vibration was taken into account to correct the lateral error of the peg. The strategies were proven applicable even for dual peg-in-hole assembly.

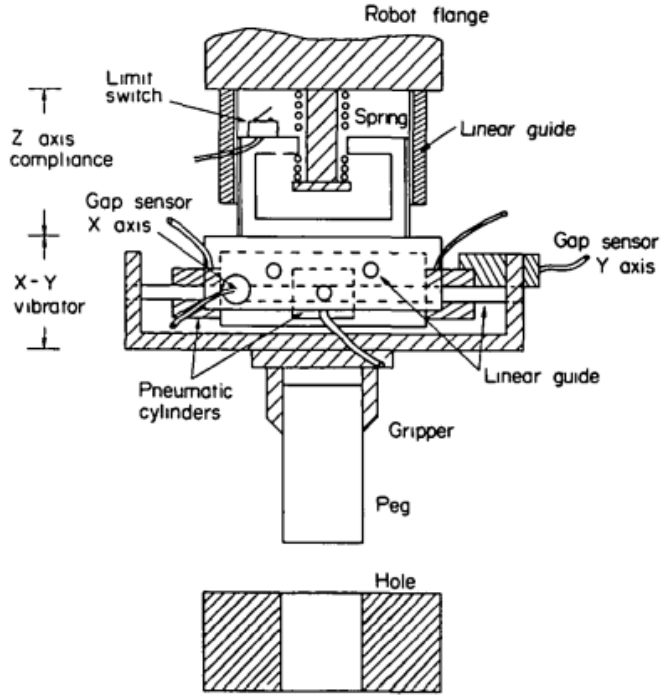

Figure 2-20. Schematic diagram of the vibratory assembly in (Jeong & Cho, 1989)

(Jeong & Cho, 1989) developed a pneumatic vibratory wrist that vibrates the peg in the horizontal plane. Only lateral error was considered in this investigation, and it was also found that the carrier frequency was the effect of the magnitude of vibration. With the combination of a fine positioning device, an FT sensor and other components, (Oh, et al., 1993) designed a magnetically levitated wrist, the Magic Wrist, which was programmed to work like an RCC device. Another method of vibration was introduced by (Kang & Cho, 1995). The vibratory wrist was powered pneumatically and consisted of x-y displacement sensors, vibrators and a gripper. The wrist was able to vibrate horizontally on the x-y plane and

rotationally vibrate about the z-axis. The neural network model was able to compensate for the positioning error and resulted in a lower interactive force between parts.

Low-frequency vibrations have been introduced to the bush as well by (Vartanov & Martynovich, 2016) for clearance fit assembly, while the shaft was held by an adaptive gripper. With the mathematical model developed, the reaction forces at contact points can be calculated, which are used to select the optimal mode of assembly.

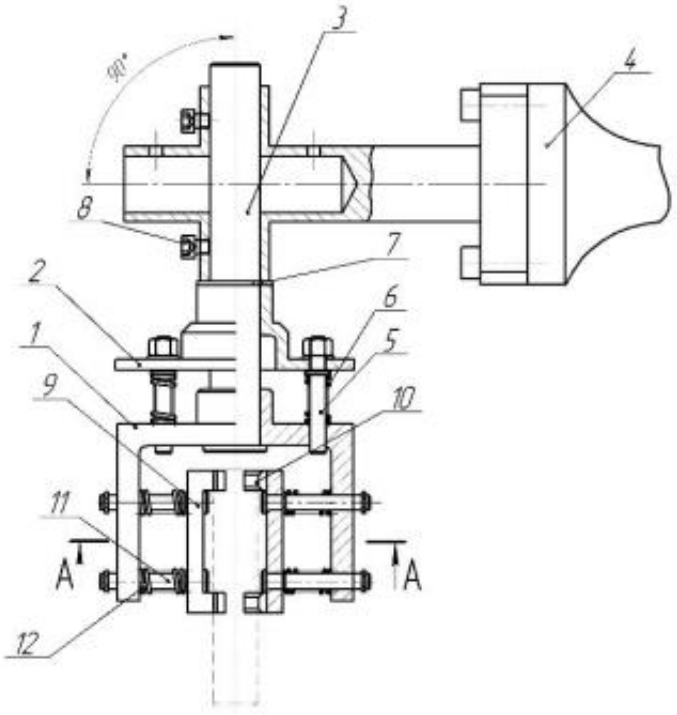

Figure 2-21. The adaptive gripper developed by (Vartanov & Martynovich, 2016)

Similar to (Vartanov & Martynovich, 2016), without using the adaptive gripper, (Vartanov, et al., 2020) rotated the shaft into the vibrating bush. It was proven that the assembly force is decreased by 14-30% in various experiments, which were influenced by

variable parameters. (Liu, et al., 2019) investigated the method of using screw insertion motion for peg hole assembly. This method was applied to both clearance and interference fit insertion. It was concluded that this method greatly reduced the axial friction and even overcame the maximum static friction force.

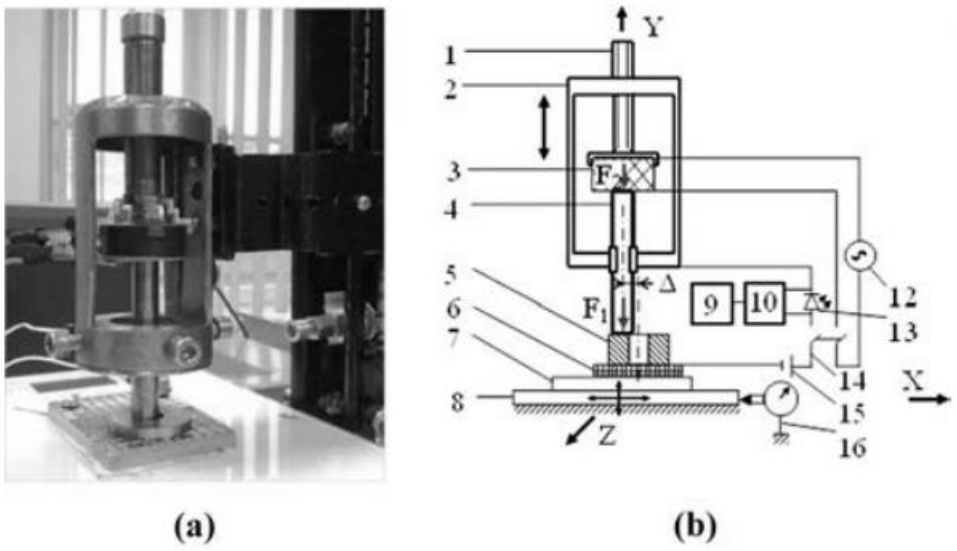

Figure 2-22. The piezoelectric vibrator in (Sadauskas & Baksys, 2014)

The combination of frequencies to create different path trajectories of the peg have been studied by (Sadauskas, et al., 2013) and (Sadauskas & Baksys, 2014). The compliant device is also integrated into the assembly of the peg with the aid of vibration. The device is installed onto the peg, while the vibration is applied to the bush. Axial vibration was implemented in (Bakšys, et al., 2010), (Kilikevicius & Baksys, 2011), (Bakšys, et al., 2011), (Bakšys, et al., 2014), and (Baksys, et al., 2017); on the other hand, the vibration was applied

on the peg with the compliant device in (Pitchandi, et al., 2017). These investigations come to similar conclusions, where the force and time needed to insert the peg decreases, and (Pitchandi, et al., 2017) found that when the vibration was applied to the peg instead, it produces a smoother damping effect than when the vibration was applied to the bush.

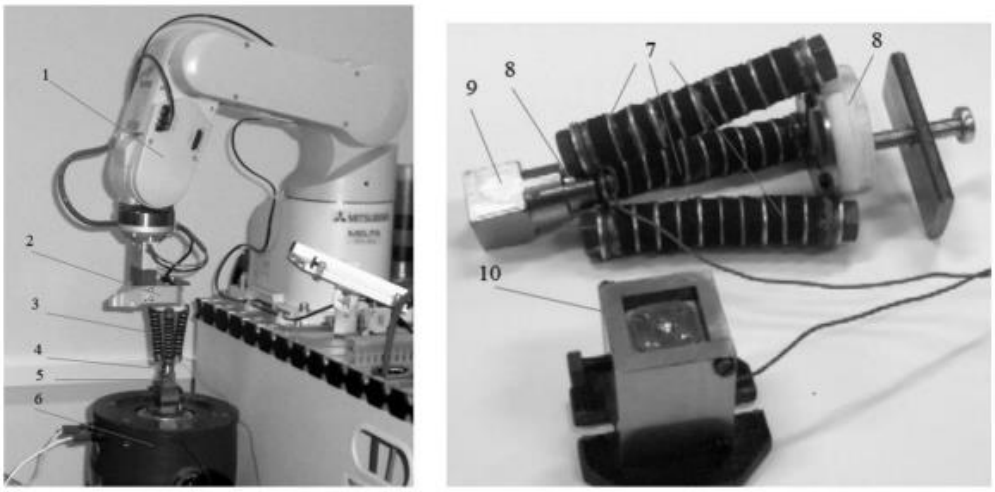

Figure 2-23. The vibratory system and RCC device in (Baksys, et al., 2017)

In disassembly, (Yoshida, et al., 2001) demonstrated the removal of fastening joints such as screws and rivets from circuit boards using impact tools, which is also known as destructive disassembly. The magnitude of the impact force required to destroy the joints was derived using simulation models. (Bakšys & Mikolainis, 2011) applied vibration on the bush rather than on the shaft in an interference fit assembly while the load was applied onto the shaft. The force applied on the shaft, the time taken for a complete assembly, the depth of

insertion with respect to time and vibration frequencies were observed, and the relationships between those parameters were established.

2.8 The disassembly of interference fit components.

In the turbine blade disassembly process, the solidification force between joints is the main barrier to having a reproducible disassembly process. (Wolff, et al., 2016) have taken the estimation of solidification force into account when disassembling interference fit turbine blades. Using higher frequencies of impulse with just enough force, the average force amplitude was reduced, and a consistent disassembly time was achieved compared to low frequency with high amplitude of force.

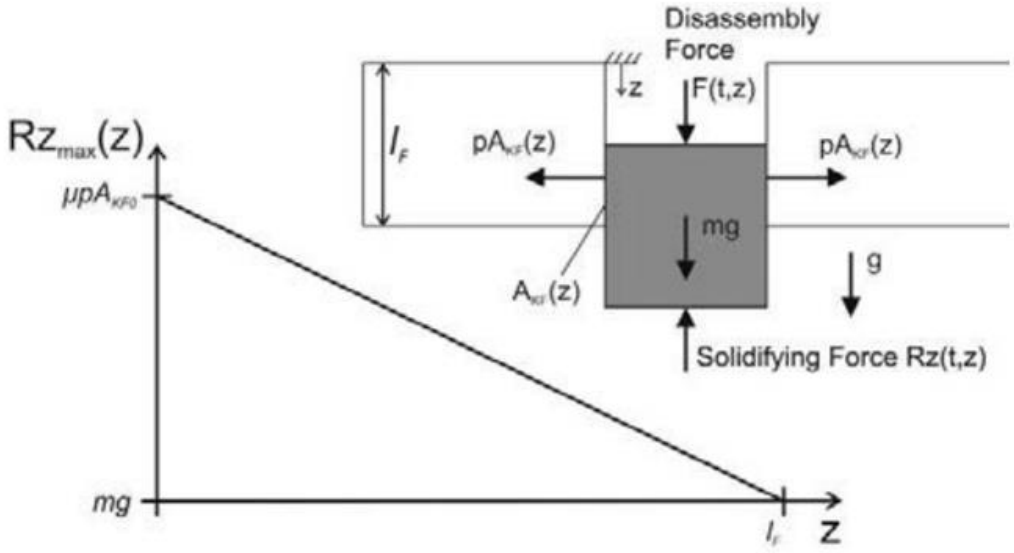

Figure 2-24. Simplified solidification model with the function of maximal solidification in (Wolff, et al., 2016)

(Wolff, et al., 2018) looked into the estimation of solidification force in detail by comparing two different geometries of turbine blades with similar usage histories using constant estimated parameters. The simulation results showed a linear relationship between the geometries of turbine blades and solidification force. (Mullo, et al., 2018) developed a model to better control the vibration disassembly force in turbine blade disassembly by designing a proportional–integral–derivative (PID) controller based on FM modulation. With the decrease in disassembly force, the strain and wear of the components were reduced as well.

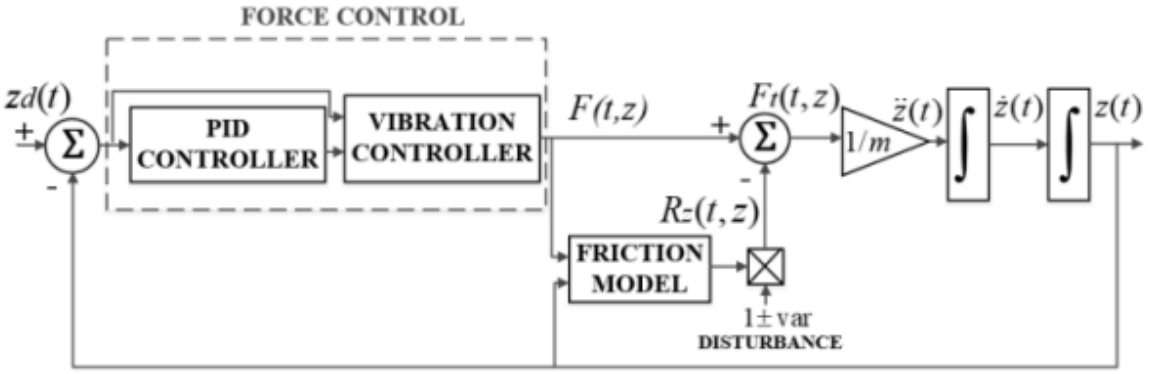

Figure 2-25. Model developed by (Mullo, et al., 2018)

(Dieudonné, et al., 2020) investigated the use of low-frequency vibration waves in the disassembly of press-fit joints. The vibration has been applied in two manners: along or perpendicular to the axis of the pin. It was found that both methods of vibrations are beneficial in separating the pin without damaging the surface of the parts.

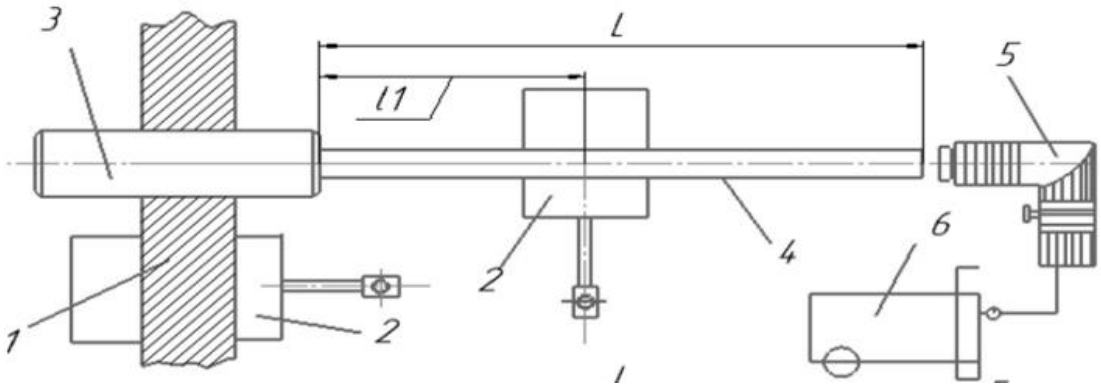

Figure 2-26. Loading of the press-fit joint using a waveguide along the shaft (Dieudonné, et al., 2020)

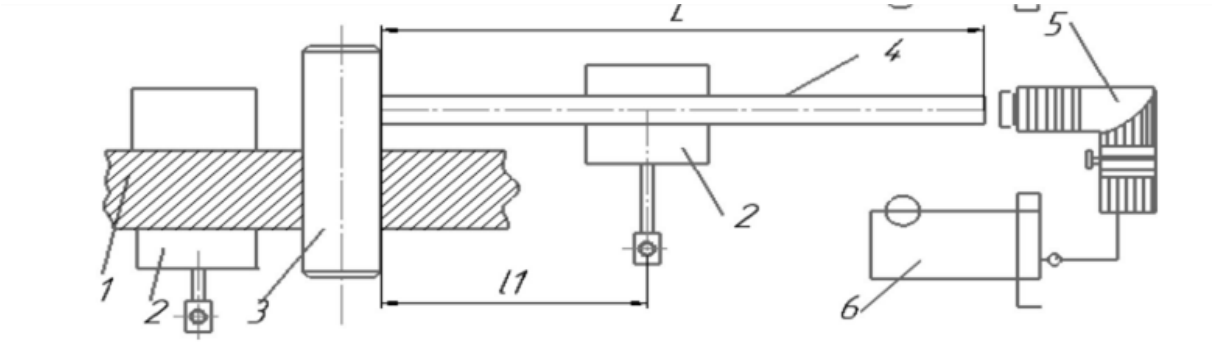

Figure 2-27. Loading of the press-fit joint using a waveguide perpendicular to the shaft (Dieudonné, et al., 2020)

2.9 Summary

Many publications so far have suggested ways to increase the success rate of peg-hole assembly by preventing jamming and wedging. As mentioned, jamming is a problem that can be easily understood and addressed, but wedging is more complex. Jamming has been the focus of many researchers. The conditions for wedging to happen have been defined, but until now, they have not been deeply examined. Thus, there is a need to investigate the problem of peg wedging, peg dislodging and tools that are more disassembly friendly.

Chapter 3

The Wedging of a Peg

3.1 Preliminaries

In the literature review carried out in Chapter 2, many researchers only mentioned the phenomenon of peg-hole wedging but have suggested numerous ways of avoiding it, and none of the literature explained or proved this phenomenon.

The wedging of a peg in a clearance hole is different from that in an interference hole. In the interference fit peg-hole, the surfaces of the peg and the hole are in contact when the peg is in the hole. Even when the contact is reduced down to two dimensions, it is still in two-line contact. However, in a clearance hole, there are only two contact points. This is the reason why the peg-hole wedging problem could be delicate and challenging when defining boundary conditions for dislodging the peg. Thus, there is a necessity of knowing and understanding the process of wedging a peg.

In this chapter, the definition and conditions for wedging are reiterated, and the process is shown in detail. Abaqus simulation is used to help visualise the process.

3.2 Wedging: Definition and Conditions

What is wedging? According to (Simunovic, 1979), the definition of wedging is that the reaction forces at the contact points are nonzero in the absence of an applied force. A more detailed description will be when the reaction forces are collinear, pinching the peg, without any external force. Figure 3-1 illustrates the reaction force at the contact points of a wedged peg when there is no external force acting on the system.

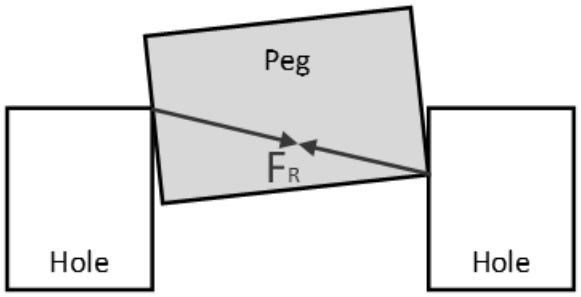

Figure 3-1. Notation of reaction force when the peg is wedged

As discussed in (Simunovic, 1979), the wedging conditions are listed below:

1. 2 of the contact points are within its opposite friction cone to allow collinear reaction forces,
2. Elastic deformation of part(s).

The conditions listed are necessary but not sufficient by themselves. Condition 1 is the most important condition among all. This claim is based on the definition of wedging. It is the collinearity of reaction forces that dictates a successful wedge. The elastic deformation of part(s) allows the storing of the reaction forces in the absence of an external force.

Condition 1 is highly dependent on the diameter of the peg and hole and the coefficient of friction. With a large clearance and small coefficient of friction, the friction cones will not be able to intersect. Figure 3-2 to Figure 3-4 illustrate the critical peg insertion depth, l_{Crit}, and maximum peg insertion depth, l_{Max}, respectively, to fulfil condition 1.

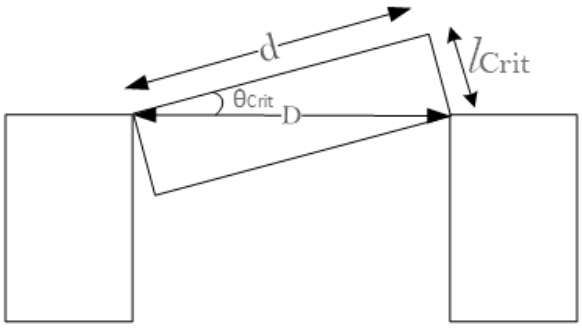

Figure 3-2. Critical length of the peg to have 2-point contact

$$l_{2P.Crit} = D \tag{3.1}$$

$$l_{Crit} = \sqrt{D^2 - d^2} \tag{3.2}$$

where $\boldsymbol{l_{2p.Crit}}$ is the critical length of the 2 contact points.

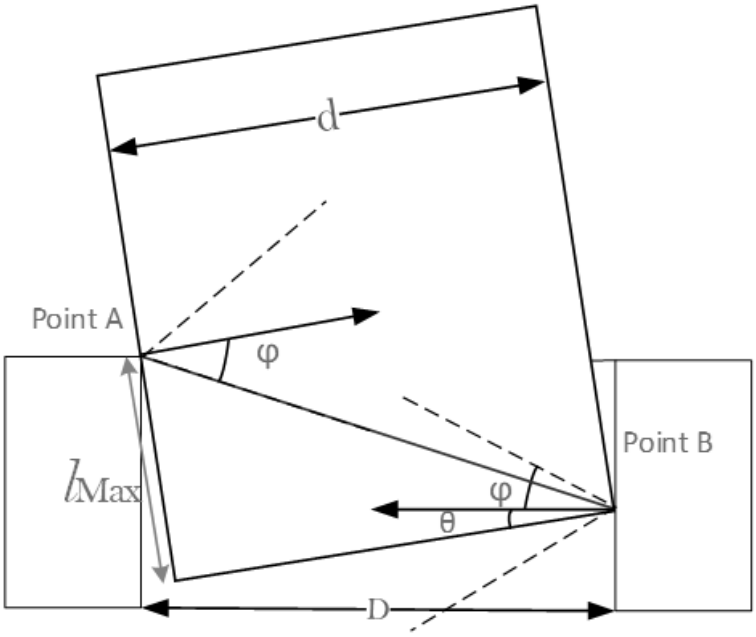

Figure 3-3. Maximum friction cone for wedging to happen

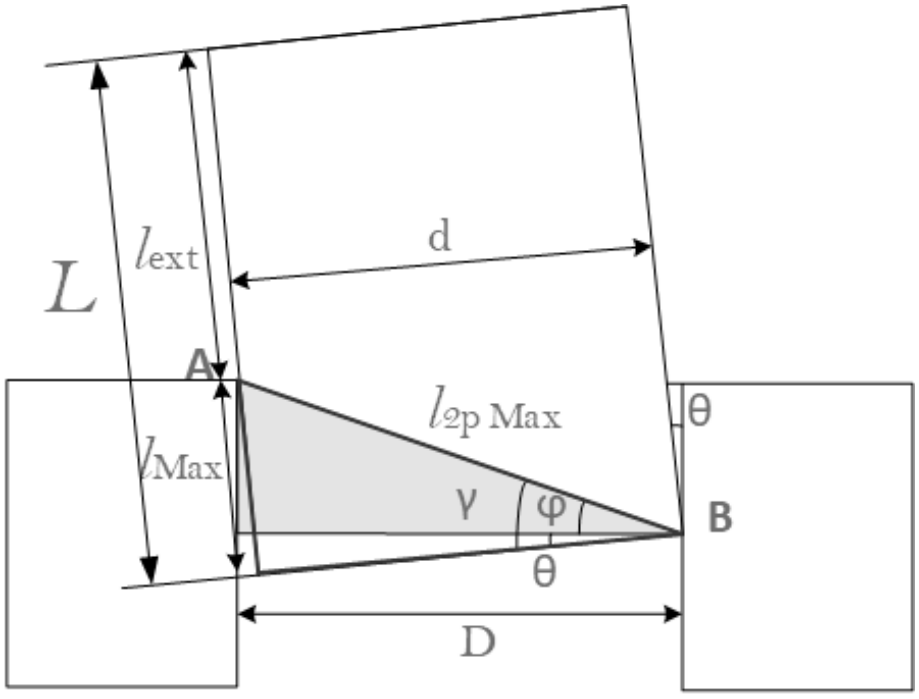

Figure 3-4. Peg at the maximum peg tilting angle to allow wedging to occur

where

$$\varphi = \tan^{-1}\mu \tag{3.3}$$

$\varphi = Maximum\ friction\ cone\ angle$

$\mu = Coefficient\ of\ friction$

The distance between 2 contact points (collinear line), l_{2P}, can be calculated, which also creates two triangles, as shown in Figure 3-4. l_{Max} is the maximum peg insertion depth where the peg is still able to wedge, which means the collinear line falls on the lower limit of the friction cone of Contact Point A and the two friction cones intersect.

$$l_{2P\,Max} = \sqrt{d^2 + l_{Max}^2} \tag{3.4}$$

$$\begin{aligned} l_{Max} &= d\ \tan\varphi \\ &= d\,\mu \end{aligned} \tag{3.5}$$

For wedging to occur, the peg insertion depth, l_d, should be within:

$$l_{Crit} \leq l_d \leq l_{Max}$$

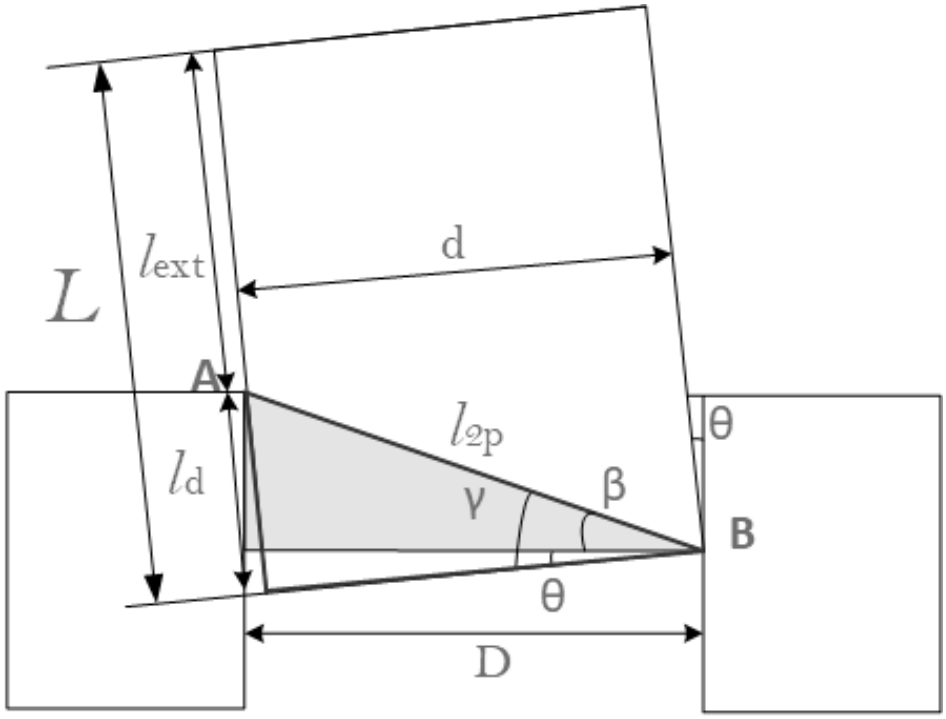

Figure 3-5. Geometry of the peg and hole when the peg insertion depth is $\boldsymbol{l_d}$

The peg tilting angle, θ, is modelled below:

$$l_{2P} = \sqrt{d^2 + l_d^2} \tag{3.6}$$

$$\gamma = \cos^{-1}\frac{d}{l_{2P}} \tag{3.7}$$

$$\beta = \cos^{-1}\frac{D}{l_{2P}} \tag{3.8}$$

$$\theta = \gamma - \beta \tag{3.9}$$

Substituting Equations (3.6) to (3.8) into (3.9) yields

$$\theta = \cos^{-1}\frac{d}{l_{2P}} - \cos^{-1}\frac{D}{l_{2P}} \tag{3.10}$$

When $l_d = l_{Crit}, l_{2P} = l_{2PCrit} = D$. Substitute Equation (3.1) into (3.10),

$$\theta_{Crit} = \cos^{-1}\frac{d}{D} \tag{3.11}$$

When $l_d = l_{Max}, l_{2P} = l_{2P\,Max}$. Substitute Equation (3.4) into (3.10),

$$\theta_{Max} = \cos^{-1}\frac{d}{l_{2P\,Max}} - \cos^{-1}\frac{D}{l_{2P\,Max}} \tag{3.12}$$

3.3 Wedging Process

Peg wedging is a complex problem; however, it can be simplified into four steps. Figure 3-6 illustrates the process of how wedging occurs.

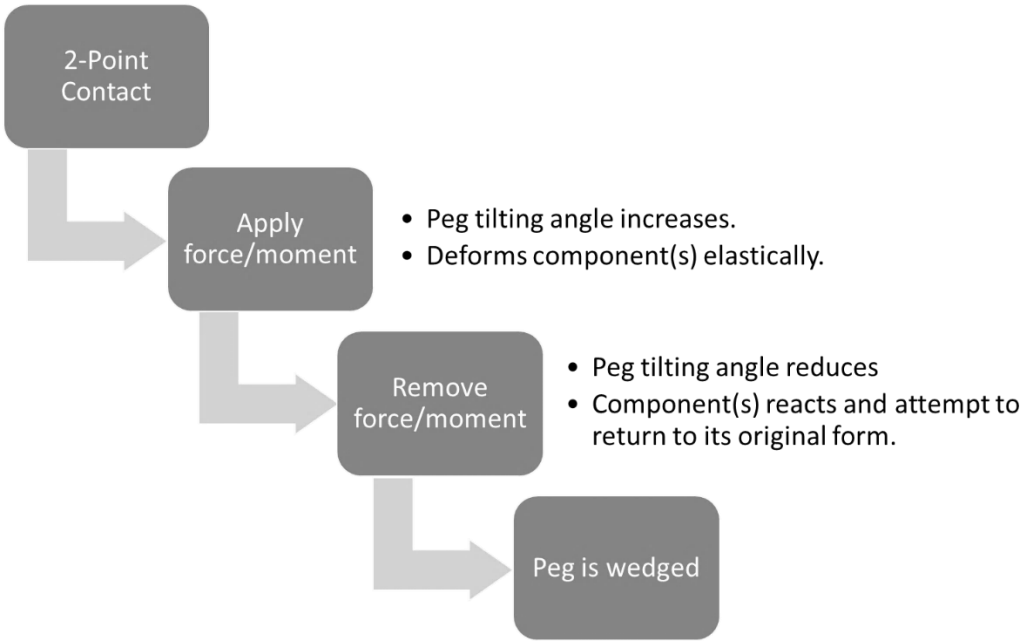

Figure 3-6. The process of wedging a peg

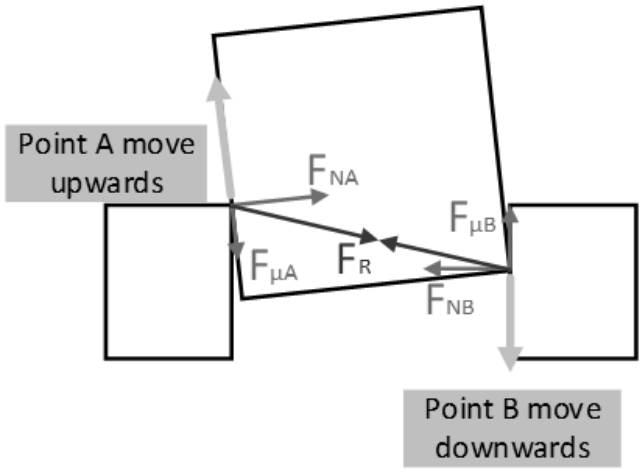

Figure 3-7. Peg rotation in step 3 for wedging to occur

By resolving the reaction forces in Figure 3-1 into normal forces and friction forces, the friction forces indicate that Contact Point A on the peg is moving upwards (downwards along the peg) and Contact Point B is moving downwards along the hole, as shown in Figure 3-7. However, this rotation of the peg reduces the angular error and will lead to 1-point contact or even no contact point. This can be seen by looking at each side of the peg and hole with the assumption of maintaining 2-point contact and without any deformation.

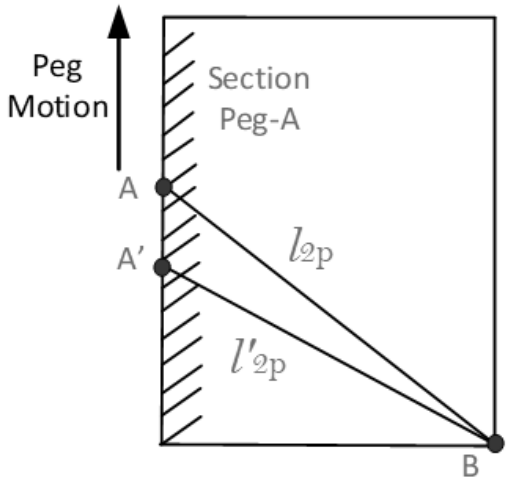

Figure 3-8. Section Peg A with upwards motion

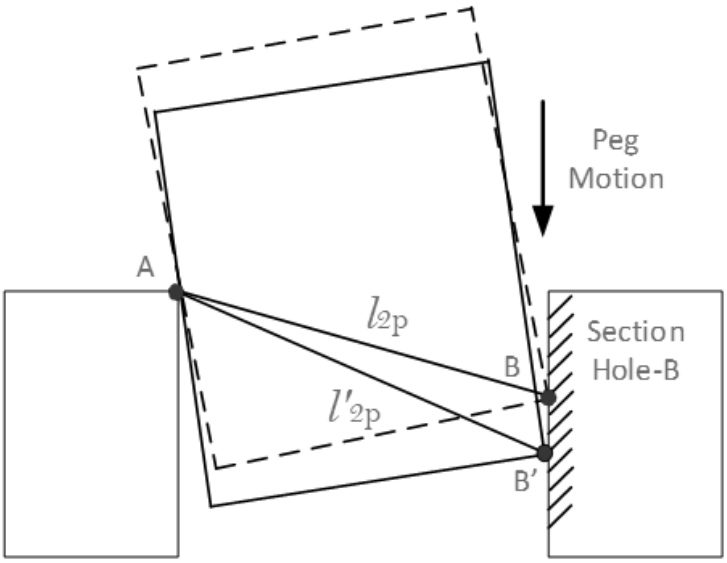

Figure 3-9. Section Peg B with downwards motion

By focusing on Contact Point A in Figure 3-8, assuming the parts are in 2-point contact with no initial deformation, Contact Point A moves downwards along the peg as Section Peg-A moves upwards because the friction force is supposed to react downwards, and Contact Point B will always be at the bottom right of the peg. This shows that the distance between the two contact points, l_{2p}, decreases.

On the other hand, Contact Point B in Figure *3-9* must move downwards along Section Hole-B to allow the friction force to react upwards. This shows that the distance between the two contact points, l_{2p}, increases.

With the assumption of maintaining 2-point contact and no initial deformation, the two observations lead to two contradictory results. Thus, to maintain 2-point contact, this peg movement is impossible. However, if the part(s) is/are already deformed elastically, this peg

motion is deemed possible. Only with the prior deformation will the peg and hole be able to remain in contact during the rotation of the peg.

3.4 Simulation of Peg Wedging

In this section, simulations are carried out to verify the theory of the wedging process. Abaqus is used for the simulations.

3.4.1 Simulation Set-Up

The simulation model setup is shown in the appendix. The parameters are determined and shown in Table 3-1. By using Equations (3.2) and (3.5),

$$l_{Crit} = 2.83\ mm$$

$$l_{Max} = 8.00\ mm$$

Table 3-1. The parameters of the simulation.

Simulation	1	2	3	4
Coefficient of Friction, μ	0.20	0.20	0.20	0.20
Peg diameter, d (mm)	40.00	40.00	40.00	40.00
Peg length, l (mm)	10.00	10.00	10.00	10.00
Inner hole Diameter, D (mm)	40.10	40.10	40.10	40.10
Peg insertion depth, l_d (mm)	4.00	5.00	6.00	10.00
Peg critical tilting angle, θ_{Crit} (deg)	1.6784	1.2560	1.0148	0.5977

The pulling force to wedge the peg applied on top of the peg is shown in Figure 3-10, and the magnitudes are:

$$F_X = -5N \; ; \; F_Y = 1N$$

The materials used for the peg and hole are mild steel and stainless steel, respectively. By comparison, the peg will be much harder to deform, in which it will be considered rigid. The peg insertion depths in Simulations 1, 2, and 3 are within the permitted range, and Simulation 4 does not investigate whether it will wedge.

There are several assumptions made in these simulations:

1. The peg is rigid.
2. The hole is deformable.
3. No gravity acts on the system.

Based on the definition of wedging by S. Simunovic, the elastic deformation of parts stores the reaction forces of contact points when no external force is present. In this simulation, 2 steps were created: in step 1, a force is applied on top of the peg, as shown in Figure 3-10; in step 2, the force is then removed to allow the hole to react.

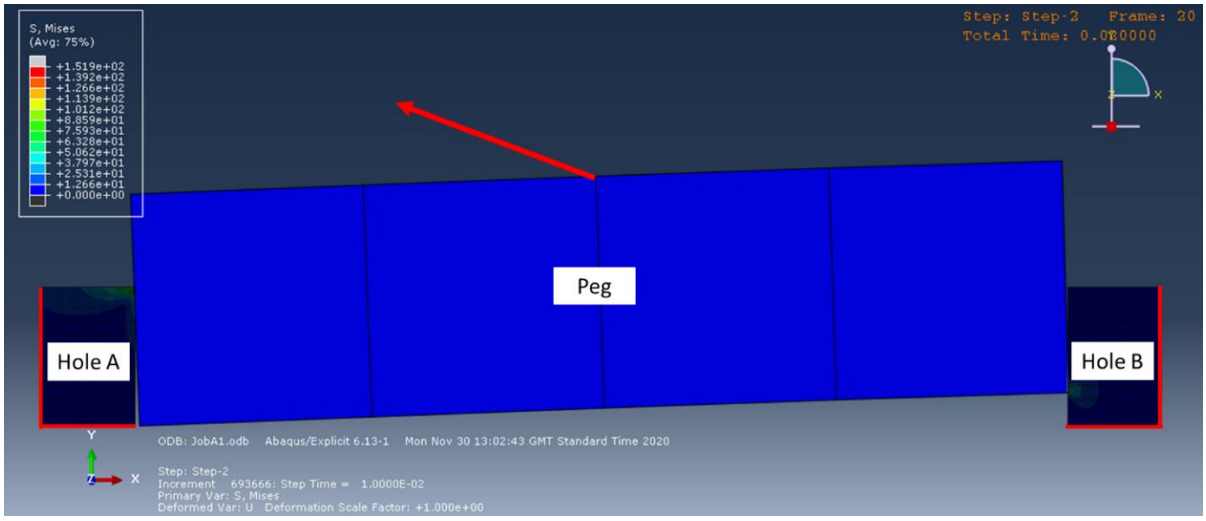

Figure 3-10. External force is applied on top of the peg in step 1 to wedge the peg

The red lines on Hole A and Hole B in Figure 3-10 are fixed boundary conditions, in which the reaction forces will be obtained. In the initial step, the peg is in 2-point contact at the critical angle, θ_{Crit}. In step 1, the hole is deformed by applying a force on the peg, and the peg tilting angle exceeds θ_{Crit}. In step 2, the force is removed and allows the peg and hole to react and return to their original form.

3.4.2 Simulation results and discussion

There are two results obtained from the simulations: reaction forces and peg angle, which are tabulated in Table 3-2 and Table 3-3, respectively.

Table 3-2.Simulation results: Reaction forces at the hole after the peg is wedged

Simulation	Reaction Forces at Hole A		Reaction Forces at Hole B		Difference between forces	
	Fx (N)	Fy (N)	Fx (N)	Fy (N)	Δ Fx (N)	Δ Fy (N)
1	13.256854	-0.434447	-13.25735	0.435108	0.000493	0.000661
2	11.723917	-0.987158	-11.72399	0.986820	0.000080	0.000338
3	9.400392	-1.106843	-9.400339	1.106558	0.000053	0.000285
4	0	0	0	0	0	0

Table 3-3. Simulation result: Peg tilting angle during the wedging process

Simulation	Peg angle (degree)		
	Initial	Step 1	Step 2
1	1.6784	3.6418	3.6224
2	1.2560	2.0619	2.0402
3	1.0148	1.4898	1.4629
4	0.5977	0.6196	N.A.

To ensure that the components are not plastically deformed, the maximum stress value from the simulation is compared to the stress–strain diagram of the material in Figure 3-11.

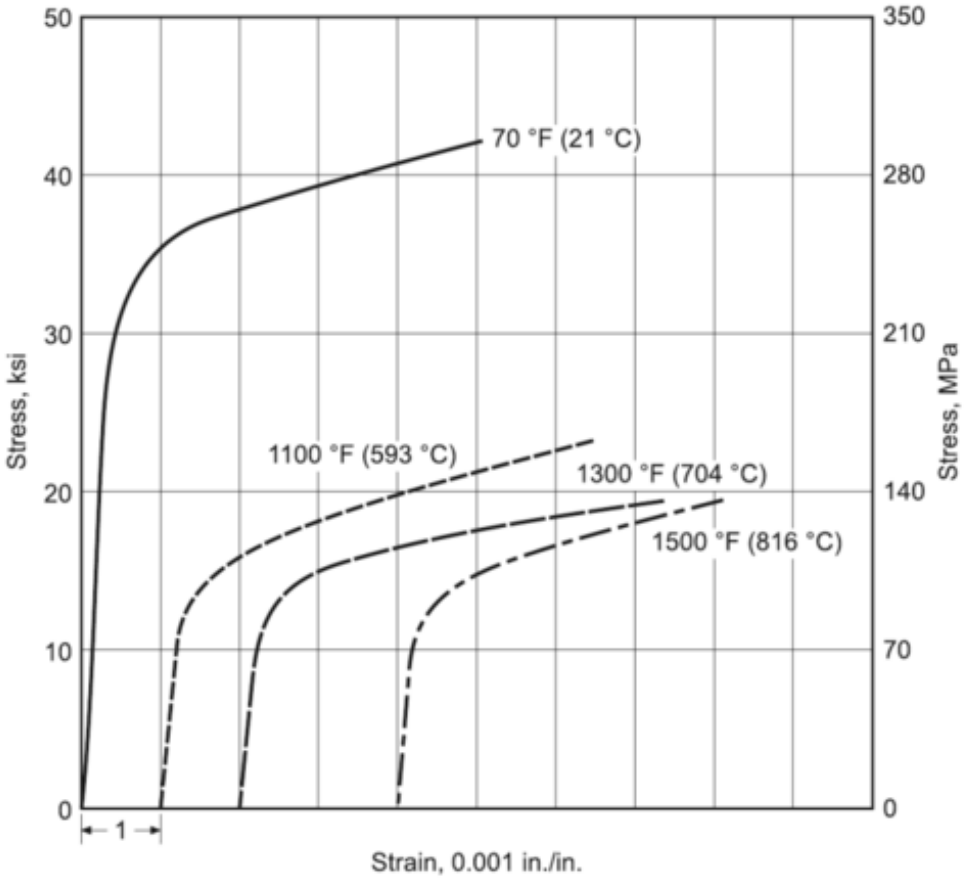

Figure 3-11. Stress–strain diagram of stainless steel 316. (Fritz & Koster, 1977)

Table 3-2 shows the final reading of the reaction forces obtained from the fixed boundary condition at Holes A and B at the end of step 2 when the peg is wedged. Comparing the x- and y-axis reaction forces of Holes A and B, the differences are very small and close to zero. Although there is no difference between the reaction forces in Simulation 4, the peg did not wedge, which explains why there are no reaction forces. This can also be seen in the simulation animation. The maximum stresses in the simulations are within the elastic limit.

The peg angles during the wedging process are recorded in Table 3-3. The initial peg angle is when the peg is in 2-point contact without deforming the hole; the peg angle in step 1 is when the external force is still acting on the peg; the peg angle in step 2 is when the external force is removed, and the hole returns to its original form due to elastic deformation. In Simulations 1 to 3, the peg angle increases in step 1 and decreases slightly in step 2. However, in Simulation 4, the peg was “floating” at the end of simulation (example shown in Figure A - 2) and does not have contact with the hole, which means there is no need to consider the peg angle at the end.

These simulation results showed that when the peg is wedged:

1. The 2 contact points are within the insertion limit with respect to the friction cone.
2. The peg angle increases in step 1 and decreases in step 2, creating a small rotation.
3. The hole is elastically deformed.
4. The reaction forces are collinear/balanced.
5. Stresses are present in the absence of an external force.

3.5 Wedging Experiment

Experiments were carried out to further verify the hypothesis of the peg-hole wedging process. However, the peg and hole consist of three metal blocks similar to the simulation instead of a cylindrical peg and a cylindrical hole. This allowed the FT sensor to be installed on each side of the hole, and the readings can then be compared.

3.5.1 Experimental Set-Up

As mentioned, the peg and hole are represented by using three metal blocks, as shown in Figure 3-12. The FT sensors used are ATI-Theta and OnRobot Hex-E, where the ATI-Theta sensor is installed on the left and the OnRobot Hex-E sensor is installed on the right. The width of the peg block (peg diameter) is 49.9 mm, and the distance between the hole blocks (hole diameter) is 50 mm.

Depending on the insertion depth of the peg, once the peg is wedged, the hole diameter will increase. Using the method of wedging mentioned before, the peg is rotated to tilt the peg at point A to wedge the peg. Three sets of experiments were carried out.

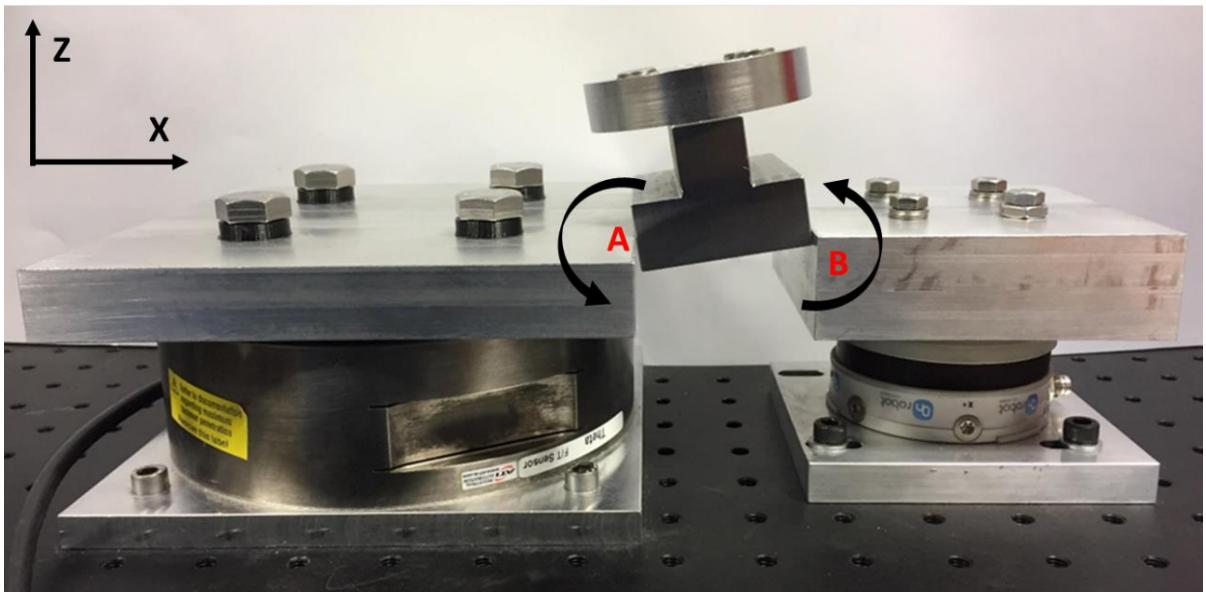

Figure 3-12. Peg-hole wedging experimental setup.

3.5.2 Experiment results and discussion

In this section, one of the three experimental results is shown and discussed. Figure 3-13, Figure 3-15 and Figure 3-17 are the summary of the wedging experiment, and Table 3-4 and Figure 3-18 show the summary of the resultant forces and the errors between the two sensors. The full results are shown in Appendix A.

Region 1 in the table and figures is where the peg is in contact with the hole, Region 2 is where the peg is rotated, Region 3 is where the peg is released, and Region 4 is where the peg is successfully wedged.

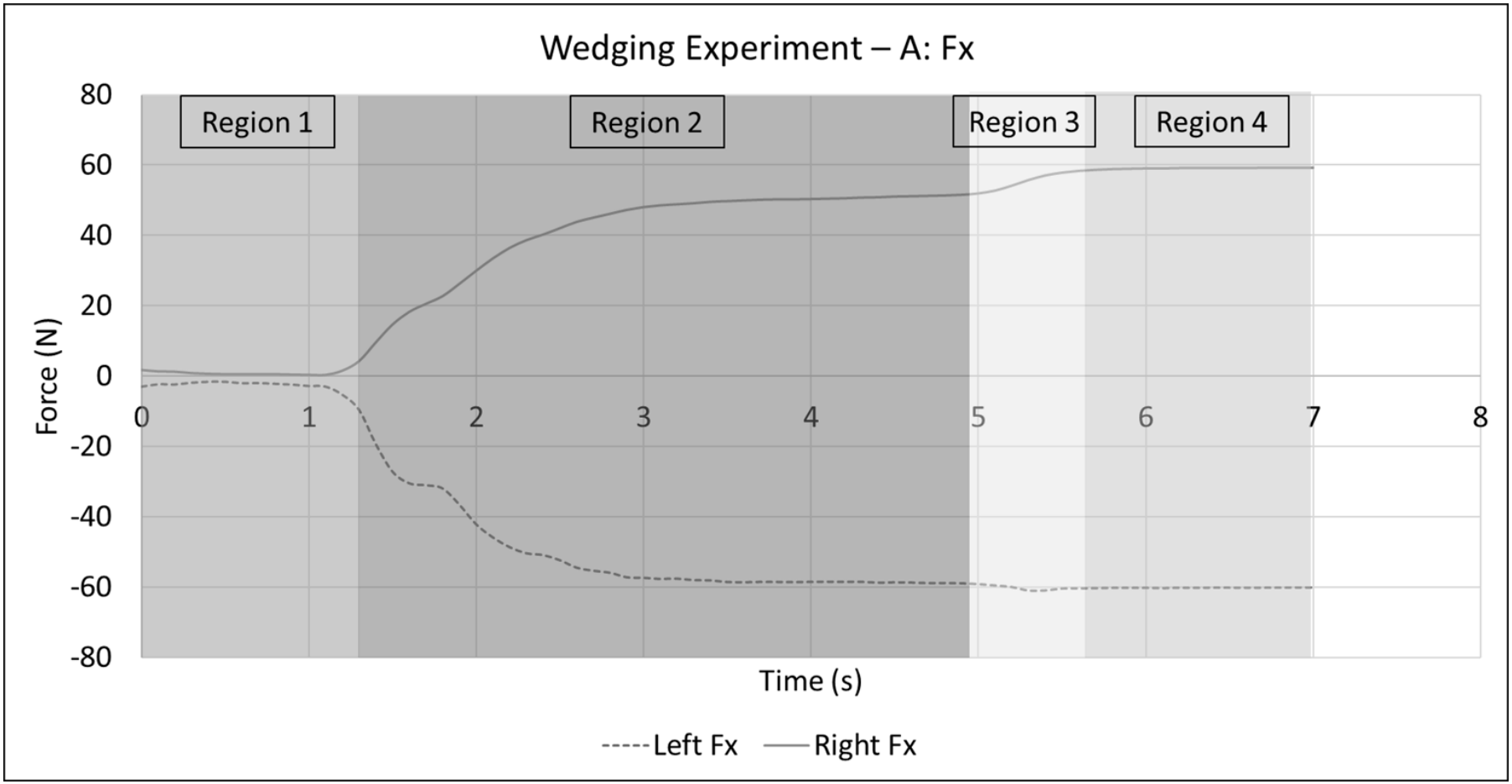

Figure 3-13. Wedging Experiment - A: Fx

When the moment is applied on the peg, Figure 3-13 shows that the left sensor and right sensor experienced a negative and positive force along the x-axis, respectively. Therefore, there were normal forces acting on the peg at the contact points, as shown in Figure 3-14. The magnitude of the force acting along the x-axis experienced by both sensors was fairly balanced.

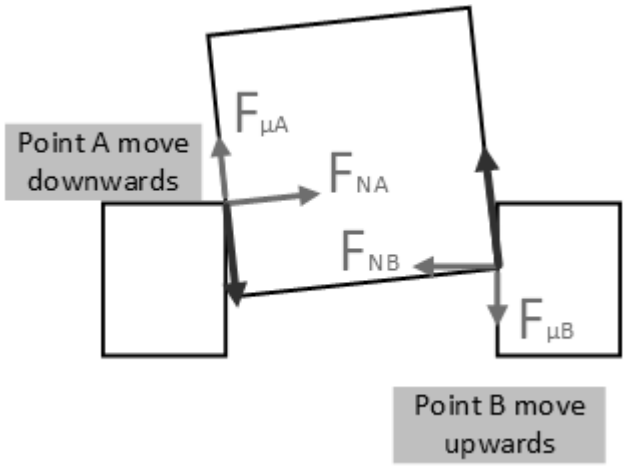

Figure 3-14. The reaction forces when the moment is applied (Step 2 of wedging process).

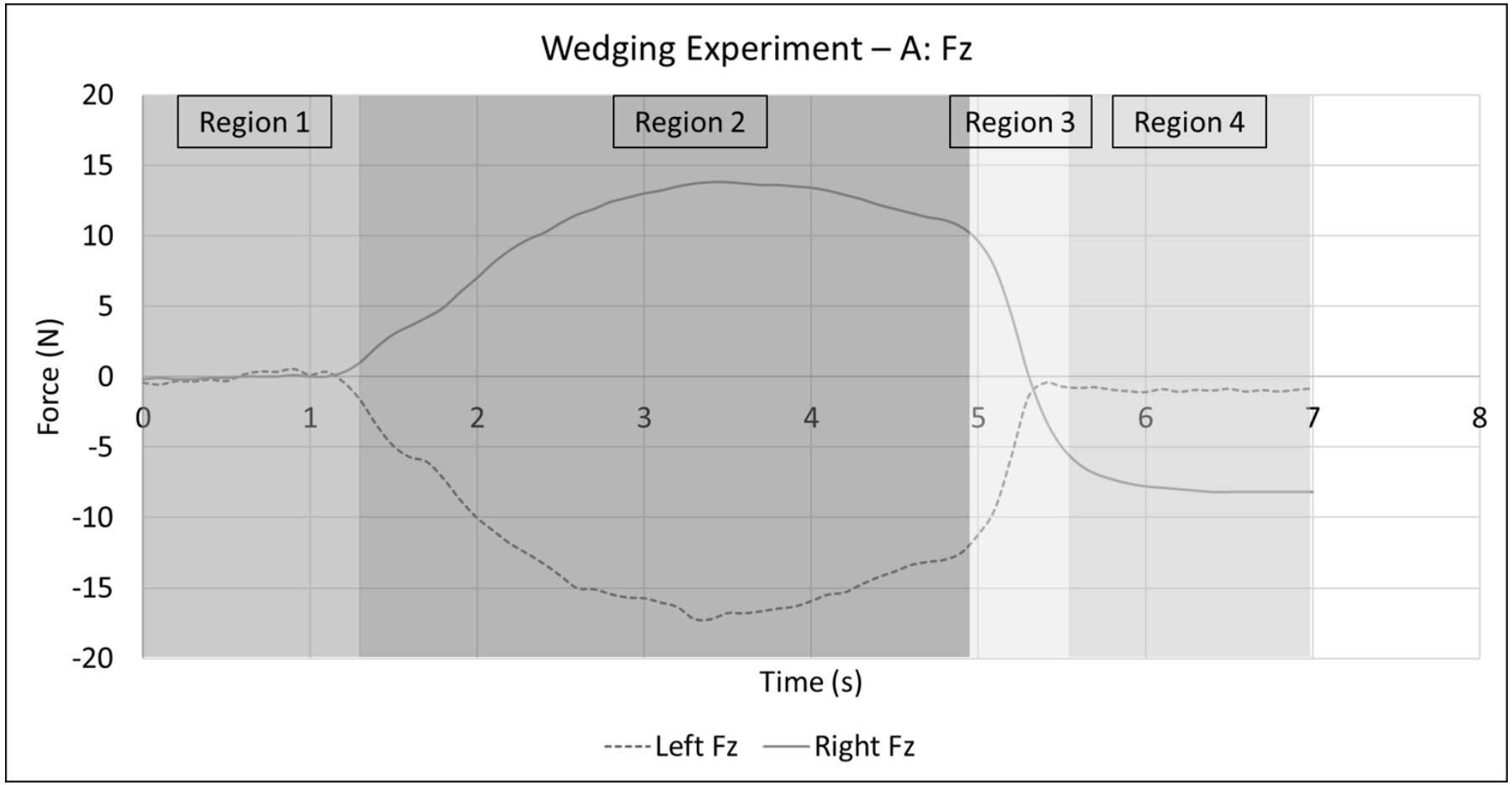

Figure 3-15. Wedging Experiment - A: Fz

A similar trend can be seen in the blue region in Figure 3-15; however, the force acting along the z-axis changes drastically in the yellow region and intersects at approximately 5.6 s, and then the forces remain constant.

According to the hypothesis, the left sensor should experience negative forces along the z-axis in the blue region, i.e., when the moment is applied, and the right sensor should detect a positive z-axis force. Then, when the moment is removed, the tilting angle of the peg reduces at a small angle, and the force acting along the z-axis will reverse, as shown in Figure 3-16: the negative force acting on the left sensor will change into a positive force; the positive force acting on the right sensor will change into a negative force. This resulted in the friction forces reversing from step 2 to step 3 in the wedging process, where the friction force at contact point A is acting downwards and the friction force is acting upwards in contact point B. This enables the resultant force at contact points A and B to be colinear.

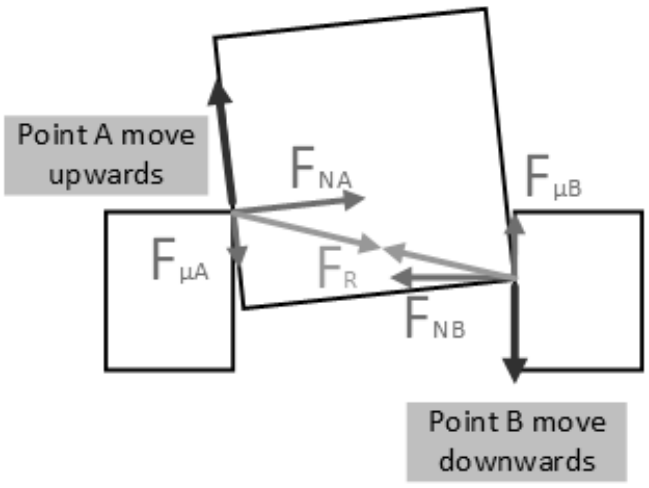

Figure 3-16. The reaction forces when the moment is removed.

Figure 3-17. Wedging Experiment - A: The reaction forces

The green region of Figure 3-17 proves that the reaction forces of the left and right sensors are equal and colinear. Similar trends were observed in the other two sets of experimental results. Table 3-4 and Figure 3-18 show the summary of the resultant forces and the errors between the two sensors. As shown in Figure 3-18, when the peg is wedged, the error between the resultant forces approaches zero, which indicates good accuracy between the readings.

Table 3-4. Wedging Experiment - A: Resultant forces and error.

Region	Time (s)	Left Resultant Force (N)	Right Resultant Force (N)	Ave Resultant Force (N)	Diff. Resultant Force (N)	Error %
1	0	3.104346	1.711724	2.408035	1.392622	57.8323
1	0.1	2.463912	1.30384	1.883876	1.160071	61.5790
1	0.2	2.524767	1.216553	1.87066	1.308214	69.9333
1	0.3	2.002668	0.824621	1.413645	1.178047	83.3340
1	0.4	1.718631	0.608276	1.163453	1.110354	95.4361
1	0.5	1.770956	0.509902	1.140429	1.261054	110.5771
1	0.6	2.138425	0.5	1.319213	1.638425	124.1972
1	0.7	2.107417	0.5	1.303709	1.607417	123.2957
1	0.8	2.300584	0.5	1.400292	1.800584	128.5863
1	0.9	2.566385	0.412311	1.489348	2.154075	144.6321
1	1	2.911364	0.3	1.605682	2.611364	162.6327
1	1.1	3.09084	0.3	1.69542	2.79084	164.6105
1	1.2	5.404506	1.532971	3.468739	3.871535	111.6122
2	1.3	9.849903	4.327817	7.08886	5.522086	77.8981
2	1.4	19.81433	9.770875	14.7926	10.04345	67.8951
2	1.5	28.0071	14.99066	21.49888	13.01644	60.5447
2	1.6	31.40983	18.66012	25.03497	12.74971	50.9276
2	1.7	31.94075	21.03093	26.48584	10.90982	41.1911
2	1.8	32.96042	23.30043	28.13042	9.659988	34.3400
2	1.9	37.81378	26.94531	32.37955	10.86846	33.5658
2	2	43.56782	30.78019	37.174	12.78763	34.3994

2	2.1	47.49985	34.44503	40.97244	13.05482	31.8625
2	2.2	50.34479	37.56062	43.9527	12.78417	29.0862
2	2.3	52.16892	39.85549	46.01221	12.31344	26.7612
2	2.4	52.82316	41.52204	47.1726	11.30112	23.9570
2	2.5	54.45508	43.43294	48.94401	11.02214	22.5199
2	2.6	56.71404	45.32439	51.01921	11.38966	22.3242
2	2.7	57.59644	46.58562	52.09103	11.01082	21.1377
2	2.8	58.25533	47.77635	53.01584	10.47898	19.7658
2	2.9	59.57364	48.91564	54.24464	10.658	19.6480
2	3	59.71329	49.76947	54.74138	9.943821	18.1651
2	3.1	60.11976	50.30398	55.21187	9.815788	17.7784
2	3.2	60.13862	50.68067	55.40964	9.457954	17.0691
2	3.3	60.82234	51.03675	55.92954	9.785585	17.4963
2	3.4	60.93359	51.46387	56.19873	9.469723	16.8504
2	3.5	61.32482	51.66749	56.49616	9.657328	17.0938
2	3.6	61.3934	51.84535	56.61937	9.548052	16.8636
2	3.7	61.24913	52.01788	56.63351	9.23125	16.3000
2	3.8	61.21557	52.1142	56.66489	9.101367	16.0617
2	3.9	61.2418	52.09463	56.66822	9.147179	16.1416
2	4	61.083	52.16522	56.62411	8.917778	15.7491
2	4.1	60.89659	52.21073	56.55366	8.685858	15.3586
2	4.2	60.88089	52.23897	56.55993	8.641918	15.2792
2	4.3	60.7206	52.35934	56.53997	8.361266	14.7882
2	4.4	60.84063	52.36153	56.60108	8.479102	14.9805
2	4.5	60.65619	52.48676	56.57147	8.169426	14.4409
2	4.6	60.6236	52.51685	56.57023	8.106747	14.3304

2	4.7	60.74542	52.55559	56.65051	8.189833	14.4568
2	4.8	60.65944	52.61046	56.63495	8.048986	14.2120
2	4.9	60.643	52.70266	56.67283	7.940342	14.0108
3	5	60.62286	52.90302	56.76294	7.71984	13.6001
3	5.1	60.72611	53.38792	57.05702	7.338192	12.8612
3	5.2	60.70294	54.3966	57.54977	6.306344	10.9581
3	5.3	61.47192	55.82284	58.64738	5.649077	9.6323
3	5.4	61.32328	57.19869	59.26098	4.12459	6.9600
3	5.5	60.72582	58.12745	59.42663	2.59837	4.3724
3	5.6	60.66371	58.73917	59.70144	1.92454	3.2236
4	5.7	60.60985	59.11455	59.8622	1.495302	2.4979
4	5.8	60.53615	59.36068	59.94841	1.175471	1.9608
4	5.9	60.53174	59.49134	60.01154	1.040393	1.7337
4	6	60.52206	59.61619	60.06913	0.905874	1.5081
4	6.1	60.59924	59.62936	60.1143	0.969889	1.6134
4	6.2	60.48753	59.74161	60.11457	0.74592	1.2408
4	6.3	60.50842	59.75508	60.13175	0.753337	1.2528
4	6.4	60.46087	59.76872	60.1148	0.692152	1.1514
4	6.5	60.46626	59.76872	60.11749	0.697539	1.1603
4	6.6	60.48196	59.76872	60.12534	0.713237	1.1863
4	6.7	60.45694	59.8676	60.16227	0.589338	0.9796
4	6.8	60.44487	59.8676	60.15624	0.577266	0.9596
4	6.9	60.41046	59.8676	60.13903	0.542855	0.9027
4	7	60.41935	59.8676	60.14348	0.551746	0.9174

Figure 3-18. Wedging Experiment - A: Errors between resultant forces

3.6 Summary

Through the simulation of wedging, the wedging process can be seen. The external force is applied on the peg and deforms the hole and increases the peg angle. Then, after the external force is removed in step 2 of the simulation, the hole is allowed to react, in which the peg angle decreases again, and this rotation causes the friction forces to react in the opposite direction and finally wedge the peg.

When the peg is wedged in the simulation, stress can still be observed in the absence of an external force. The highest stress in the simulation was still within the elastic limit of the material, ensuring that the deformation of the hole was elastic. In Simulations 1 to 3 of peg wedging, the geometrical setup fulfils the necessary conditions for the peg to wedge, and the results have shown that the peg was able to wedge. The peg in Simulation 4 did not wedge at the end of the simulation. This has shown that the 2 contact points must be within the range of the friction cones; otherwise, they will not wedge. The comparison of the reaction forces on each side of the hole in the simulation shows that it is balance/colinear, which reflects the definition of wedging shown in Figure 3-1.

In the experiment, the peg and hole were represented using three metal blocks to separate the hole into two sides. Then, two separate FT sensors were installed beneath the metal block on each side of the hole. Using the proposed method of wedging, the readings of the FT sensors throughout the wedging process were recorded and analysed. The results have confirmed the hypothesis correct, where the peg will wedge after the external force or

moment is removed. The resultant force of the left is balanced with the reaction forces on the right, and the error between the two readings is low. The definition and the necessary conditions of wedging are confirmed to be correct.

Chapter 4
Dislodging a Peg Using Impulses

4.1 Preliminaries

Using the method in Chapter 3, a peg can be systematically wedged and repeated. To avoid damaging the components when dislodging the peg, it is preferable to pull the peg using a low magnitude of force, as it will be easier to control the dislodging process; but it would require a longer time to remove the wedged peg. However, it is desirable to complete the dislodging of the peg as fast as possible to maintain the efficiency of the disassembly process. Using the principle of impulse in (Hibbeler & Yap, 2013), the relationship between the magnitude of force and dislodging duration can be observed.

In this chapter, the wedged peg is pulled vertically upwards, as shown in Figure 4-1, using a constant force and pulled using impulses with different frequencies. The process is repeated using different magnitudes of forces. Simulations are carried out to manipulate and record the results more easily.

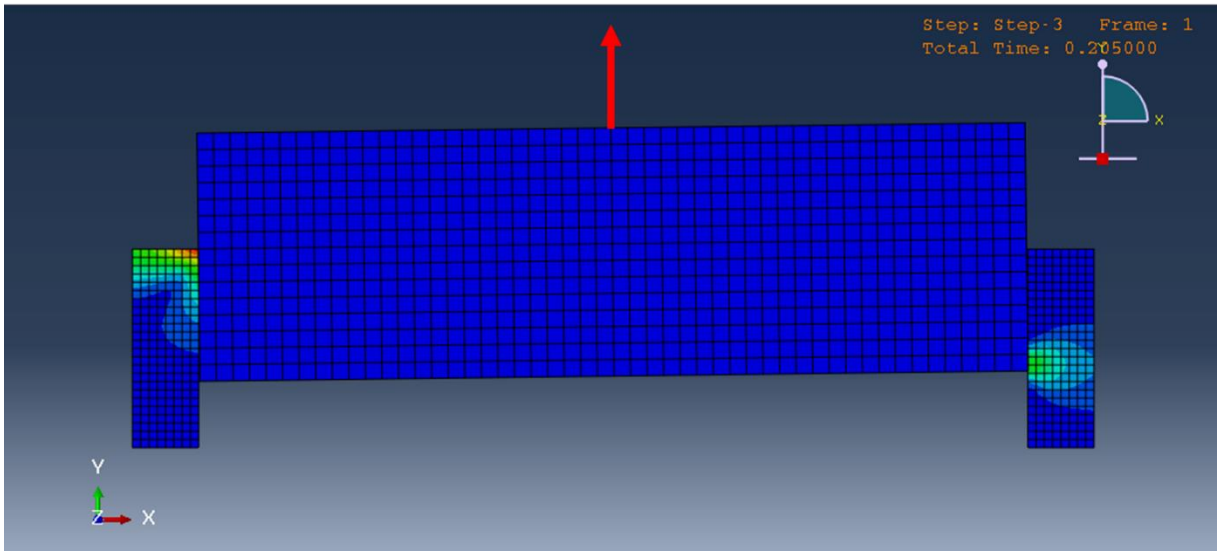

Figure 4-1. The force applied to dislodge the peg

4.2 Simulation of Peg Dislodging

4.2.1 Simulation set Up

In this investigation, the geometry of the peg and hole are:

$$Peg\ Diameter, d = 50\ mm$$

$$Hole\ Diameter, D = 50.05\ mm \quad (4.1)$$

$$Coefficient\ of\ Friction, \mu = 0.2$$

After substituting Equation (4.1) into Equations (3.2)and (3.5),

$$l_{Crit} = 2.2366\ mm$$
$$l_{Max} = 10\ mm \tag{4.2}$$

For the simulation, the two insertion depths of the peg for this investigation are:

$$Case\ 1: l_1 = 7\ mm$$
$$Case\ 2: l_2 = 8\ mm \tag{4.3}$$

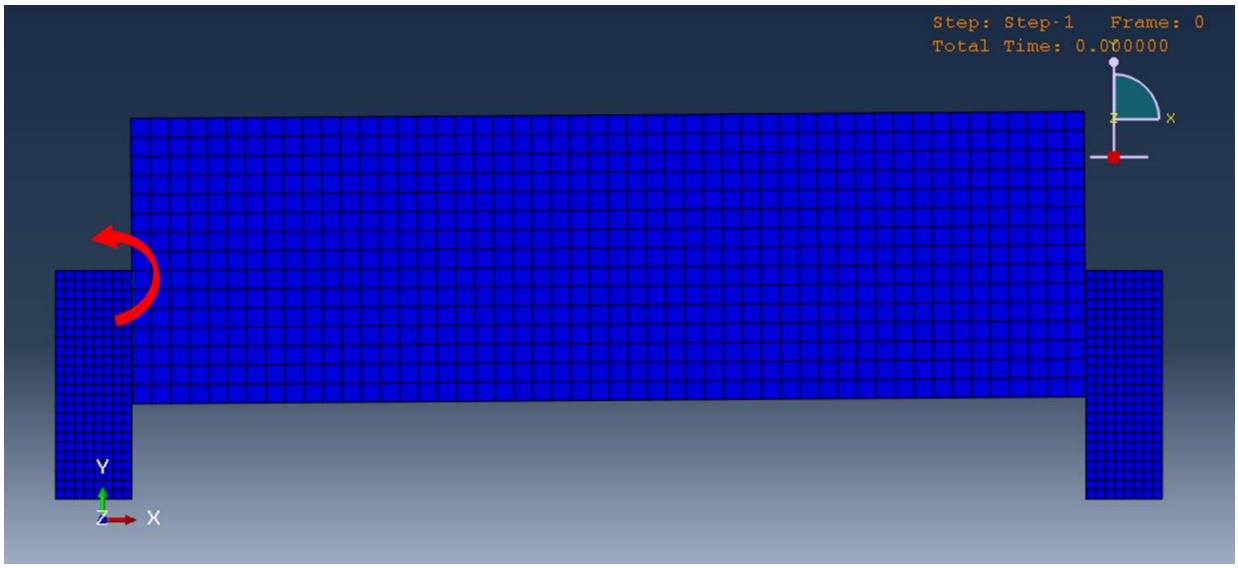

Figure 4-2. The applied moment to wedge the peg

There are four steps in the simulation. For both cases, a counterclockwise moment of 1000 Nmm for Case 1 and 1500 Nmm for Case 2 is applied at Point A of the peg in step 1, as shown in Figure 4-2. Then, the moment is removed in step 2 to allow the peg and hole to react and wedge. The dislodging force is applied in step 3. Step 4 allows the unsuccessful of peg dislodging to be observed. Due to time constraints and computing power, the time frame for each step is 0.1 seconds. There are 20 frames in each step, which is 0.005 seconds each frame.

4.2.2 Methods of dislodging the peg.

There were six methods of pulling the peg. The force inputs are shown in Figure 4-3.

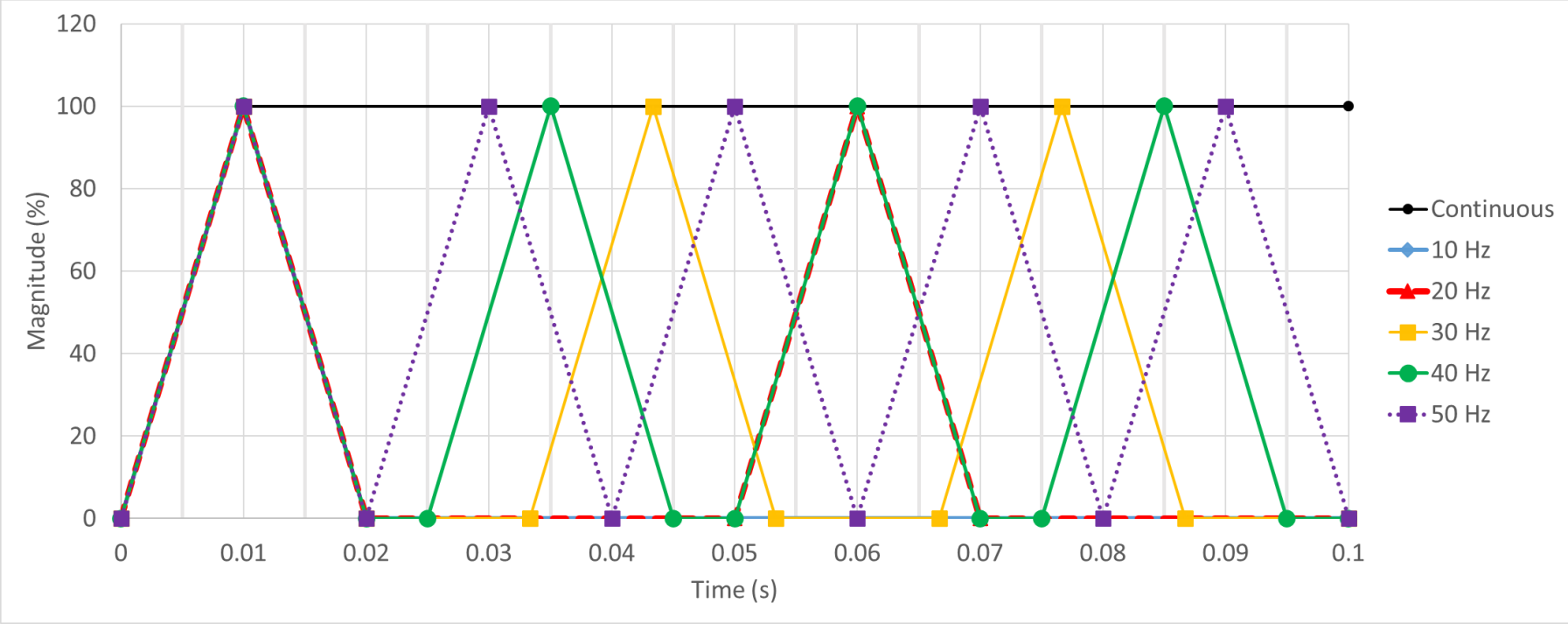

Figure 4-3. The input frequencies of dislodging the peg

A range of forces are applied in each investigation, and the time taken for the peg to dislodge is recorded. It ranges from approximately 20 N to 25 N. This range is estimated when applying the continuous force to see what is the minimum force to dislodge the peg.

4.3 Results and discussion.

4.3.1 Simulation results.

Figure 4-4 and Figure 4-5 show the frame number (time taken in simulation) for the peg to dislodge in step 3. Using equation (4.4) to (4.6), the impulse needed to dislodge the peg is calculated. Figure 4-7 and Figure 4-8 show the impulse required to dislodge the peg. The full results are shown in Appendix B.

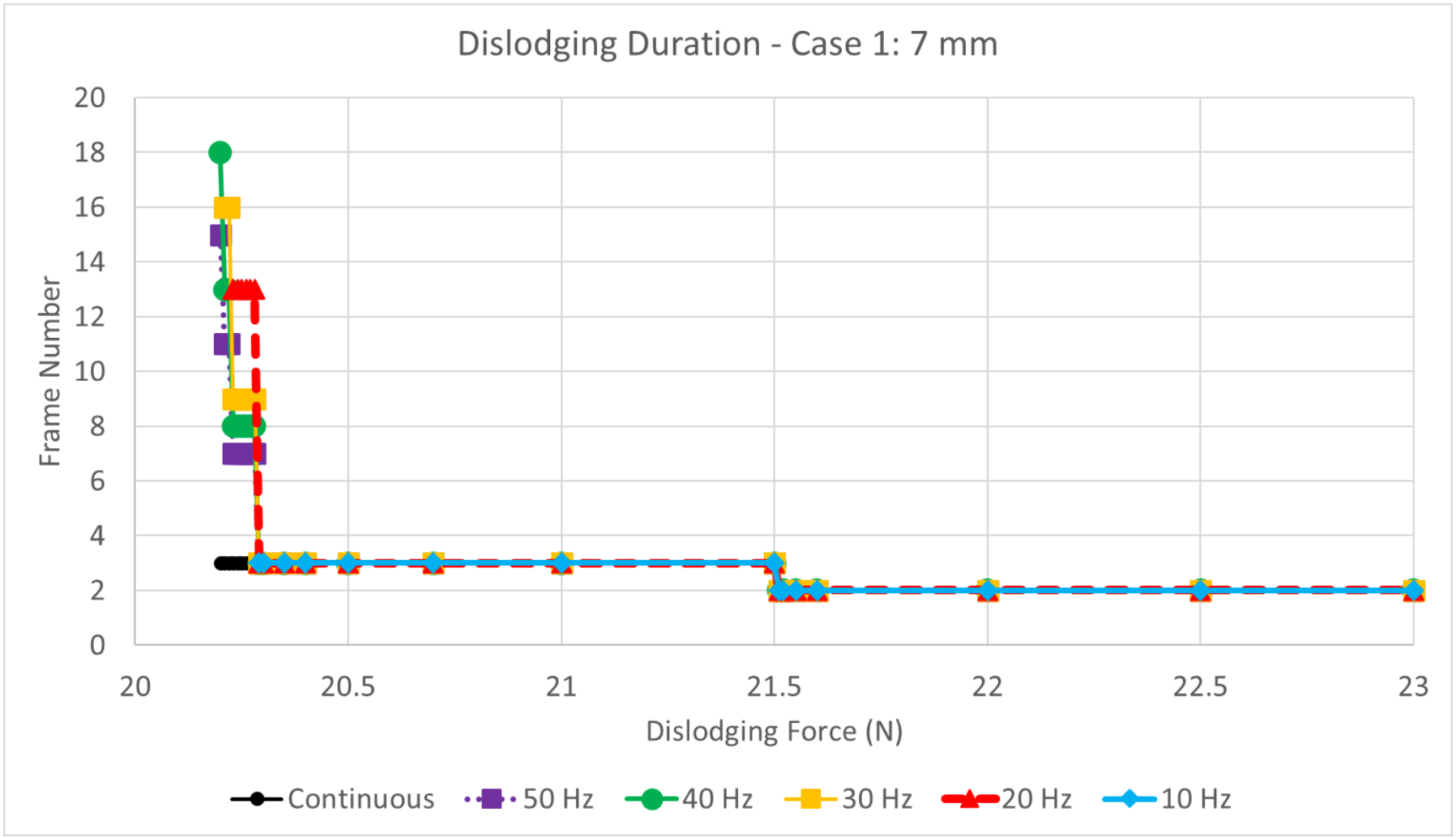

Figure 4-4. Frame number when the peg is dislodged – Case 1

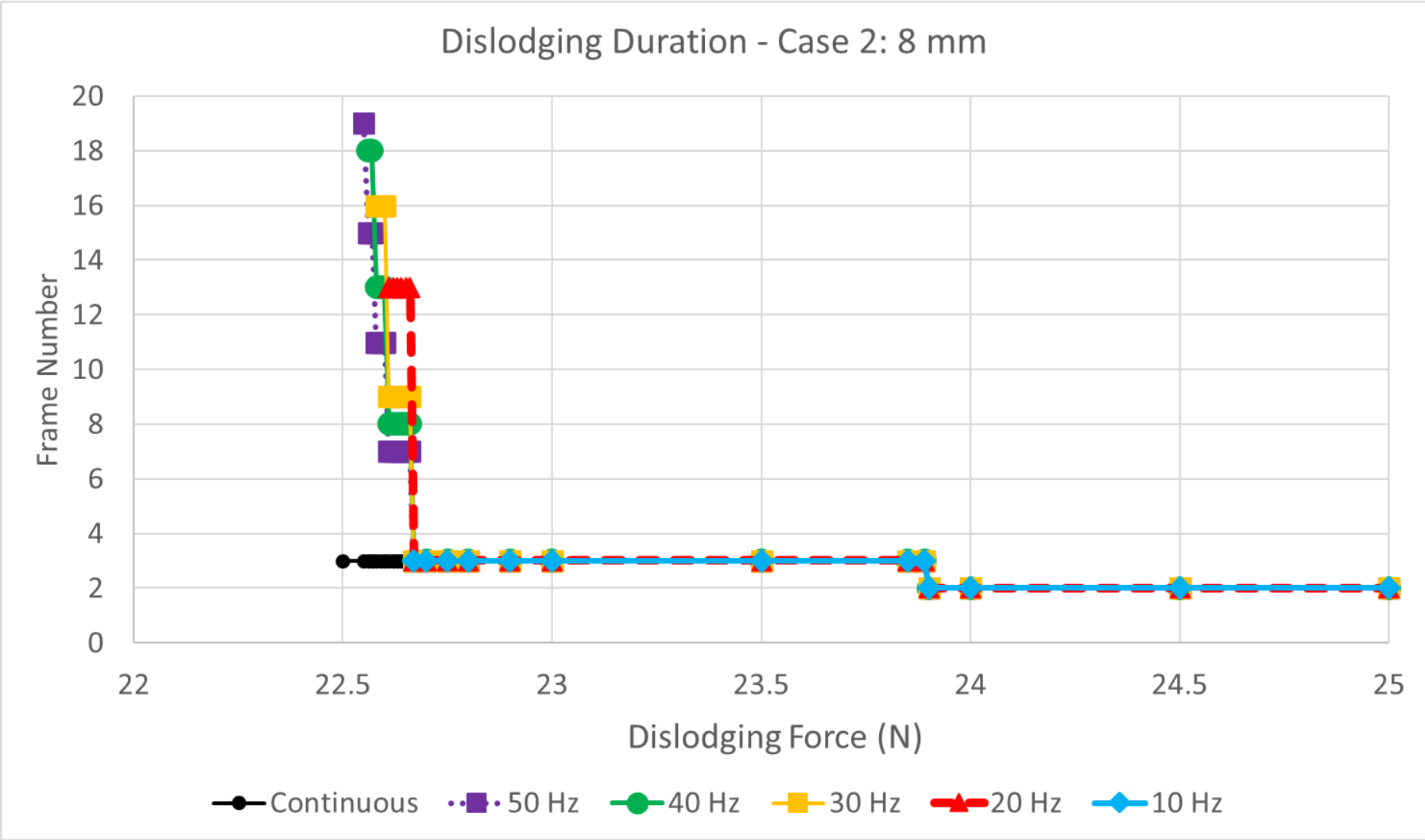

Figure 4-5. Frame number when the peg is dislodged – Case 2

To determine the impulse needed to dislodge the peg, the area under the graph is calculated.

Figure 4-6 shows an example of calculating the area under the graph for case 1:

$$l_{case\ 1} = 7mm$$

$$Frequencdy, f = 50\ Hz$$

$$F = 20.2\ N \tag{4.4}$$

$$Dislodge\ Frame\ Number = 15$$

$$Time\ taken\ to\ unwedge, t = \frac{15}{20} \times 0.1s$$

$$= 0.075s \tag{4.5}$$

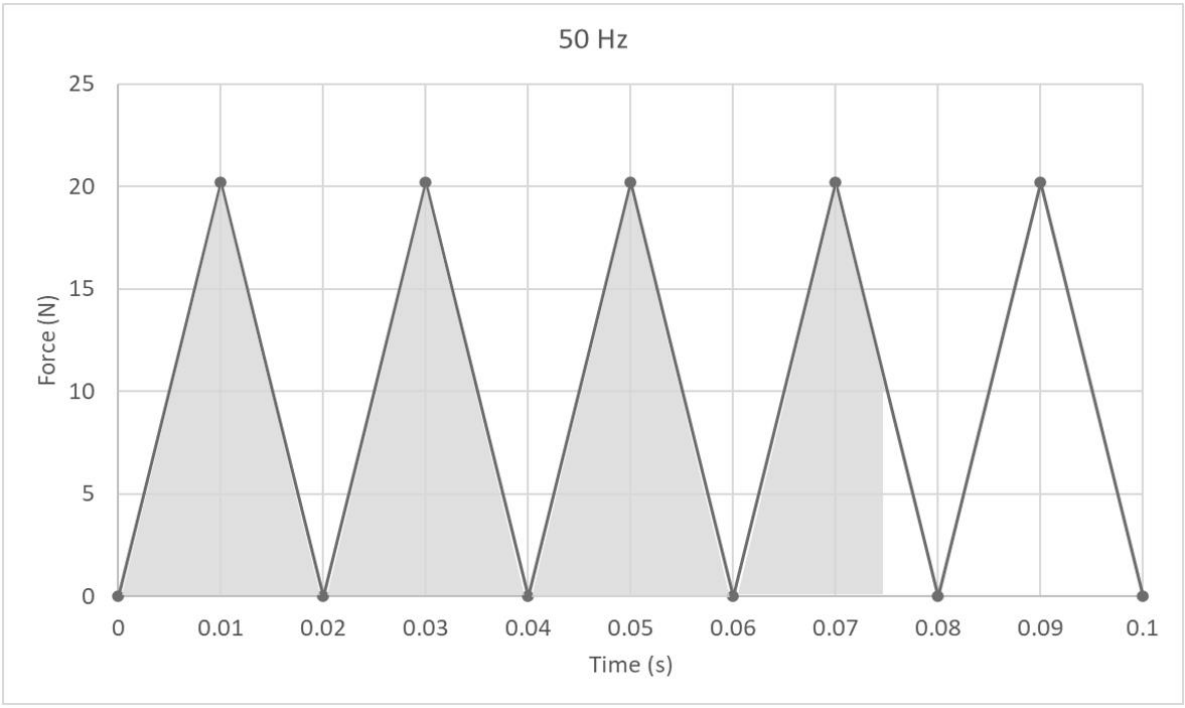

Figure 4-6. An example of the area under the graph

$$Impulse = 4\left(\frac{0.02s \times 20.2\ N}{2}\right) - \frac{(0.005s \times 10.1N)}{2} \quad (4.6)$$

$$= 0.78275Ns$$

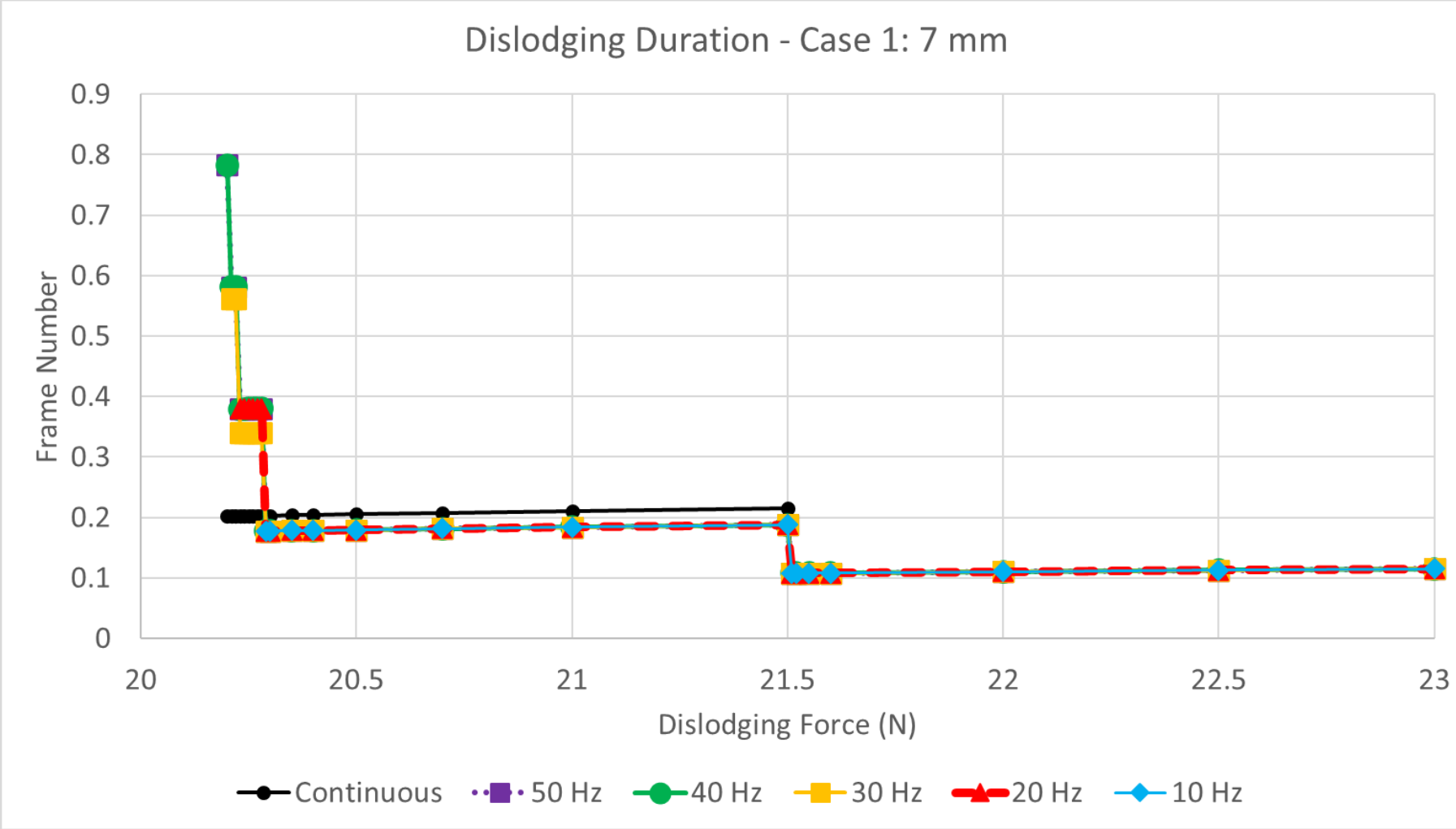

Figure 4-7. Impulse required to dislodge the peg - Case 1

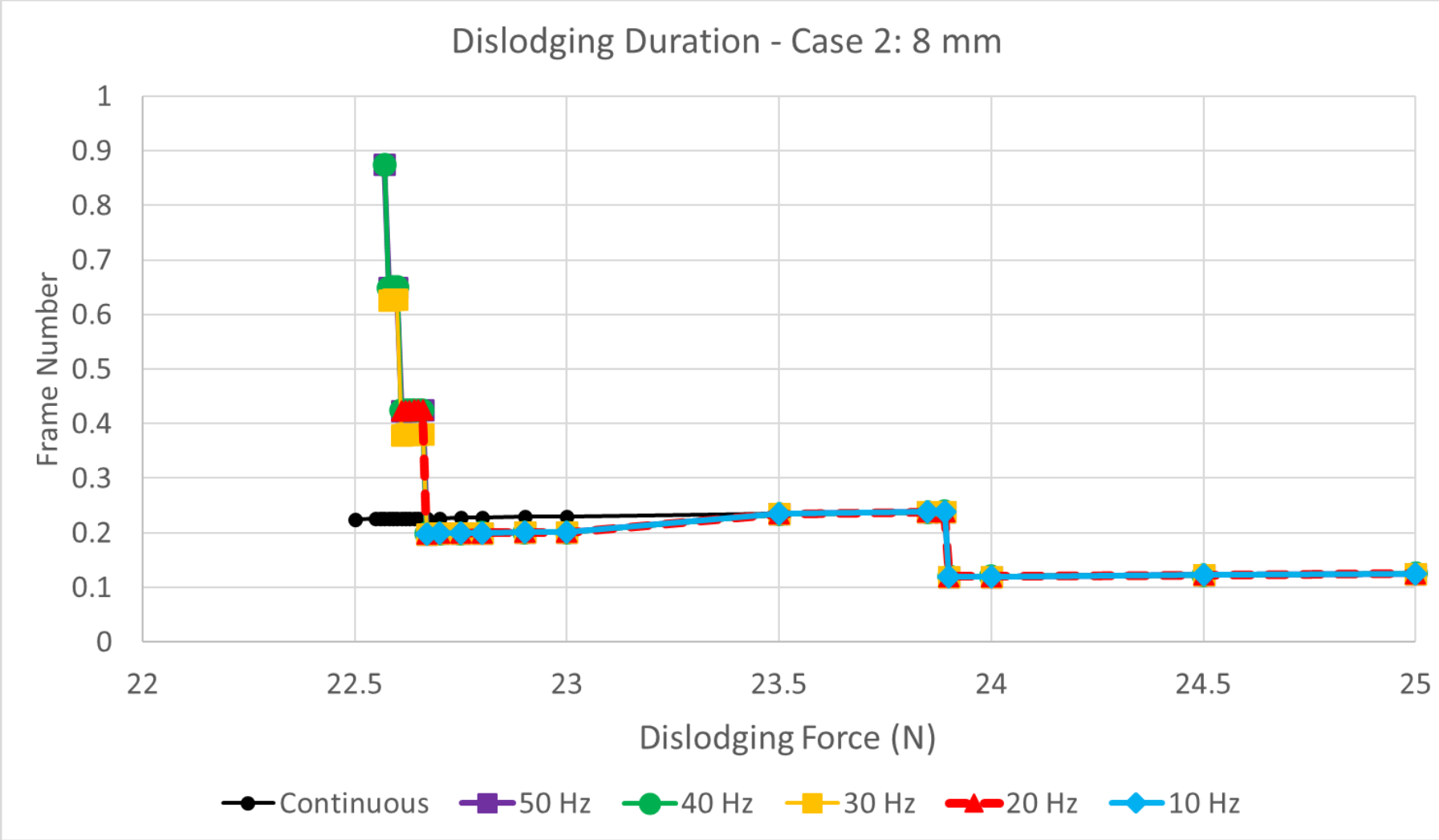

Figure 4-8. Impulse required to dislodge the peg – Case 2

4.3.2 Discussion.

The peg was dislodged at different times depending on the frequency of impulse and the magnitude of force used for pulling the peg. Similar trends were observed in both cases.

As the magnitude of the pulling force decreases, the time taken to dislodge the peg increases. The lowest impulse achieved in case 1 is 0.10755 Ns and 0.1195 Ns for case 2, in which the peg dislodges at frame 2 in the simulation for both cases.

With higher frequency, the peg is able to dislodge at a lower magnitude of force, but it requires a longer duration, which results in higher impulse. Between 20.30 N and 21.50 N in case 1 and 22.70 N and 23.50 N in case 2, pulling the wedged peg using pulses is able to reduce the impulse compared to when using a continuous force. However, when the magnitude is lower than 20.29 N in case 1 (Figure 4-9) and 22.70 N in case 2 (Figure 4-10), the peg is dislodged at a lower impulse using continuous force. Then, when the magnitude exceeds 21.50 N in case 1 and 23.90 N in case 2, the impulse increases linearly.

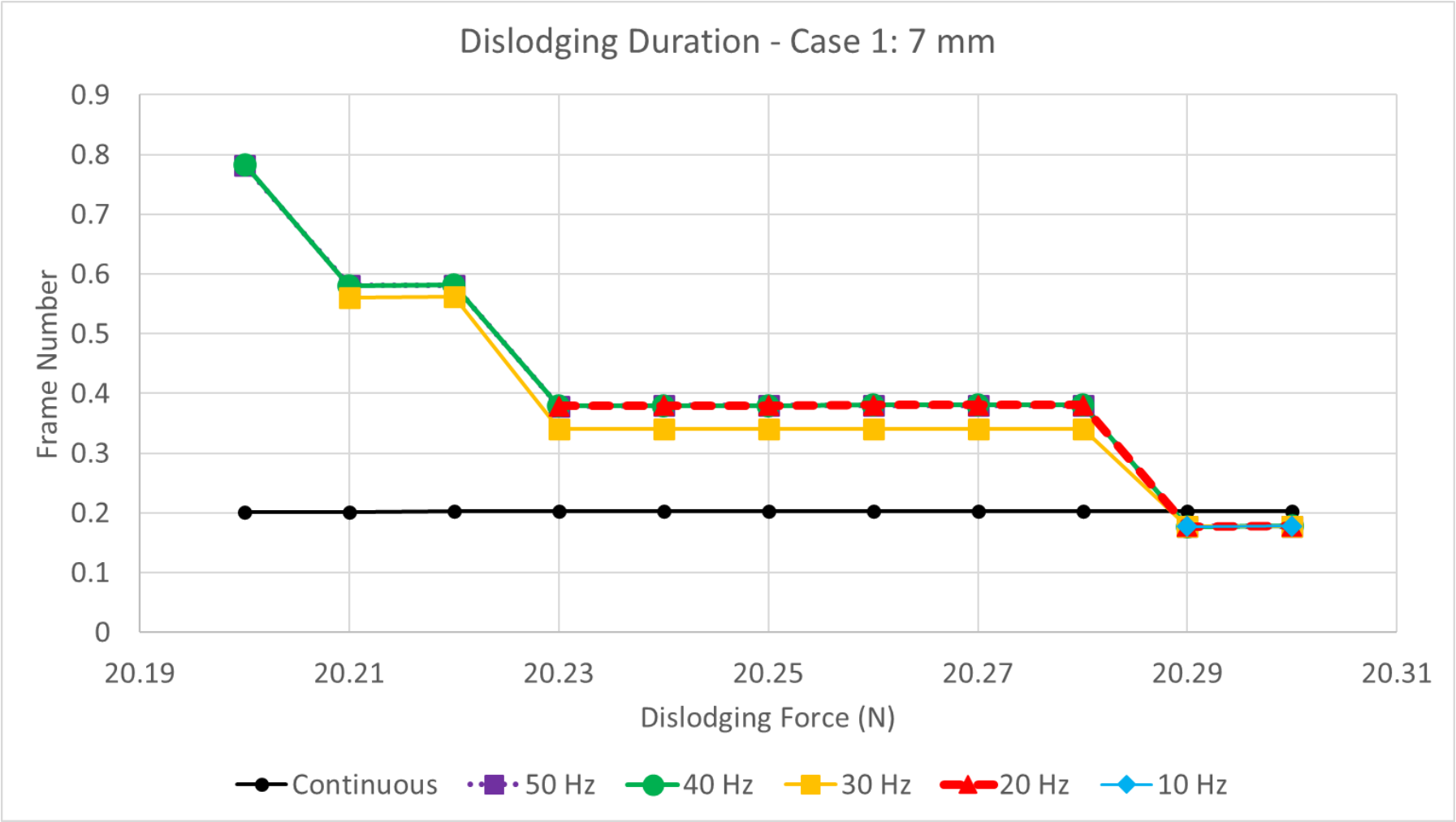

Figure 4-9. Impulse required to dislodge the peg – Case 1 (Magnified)

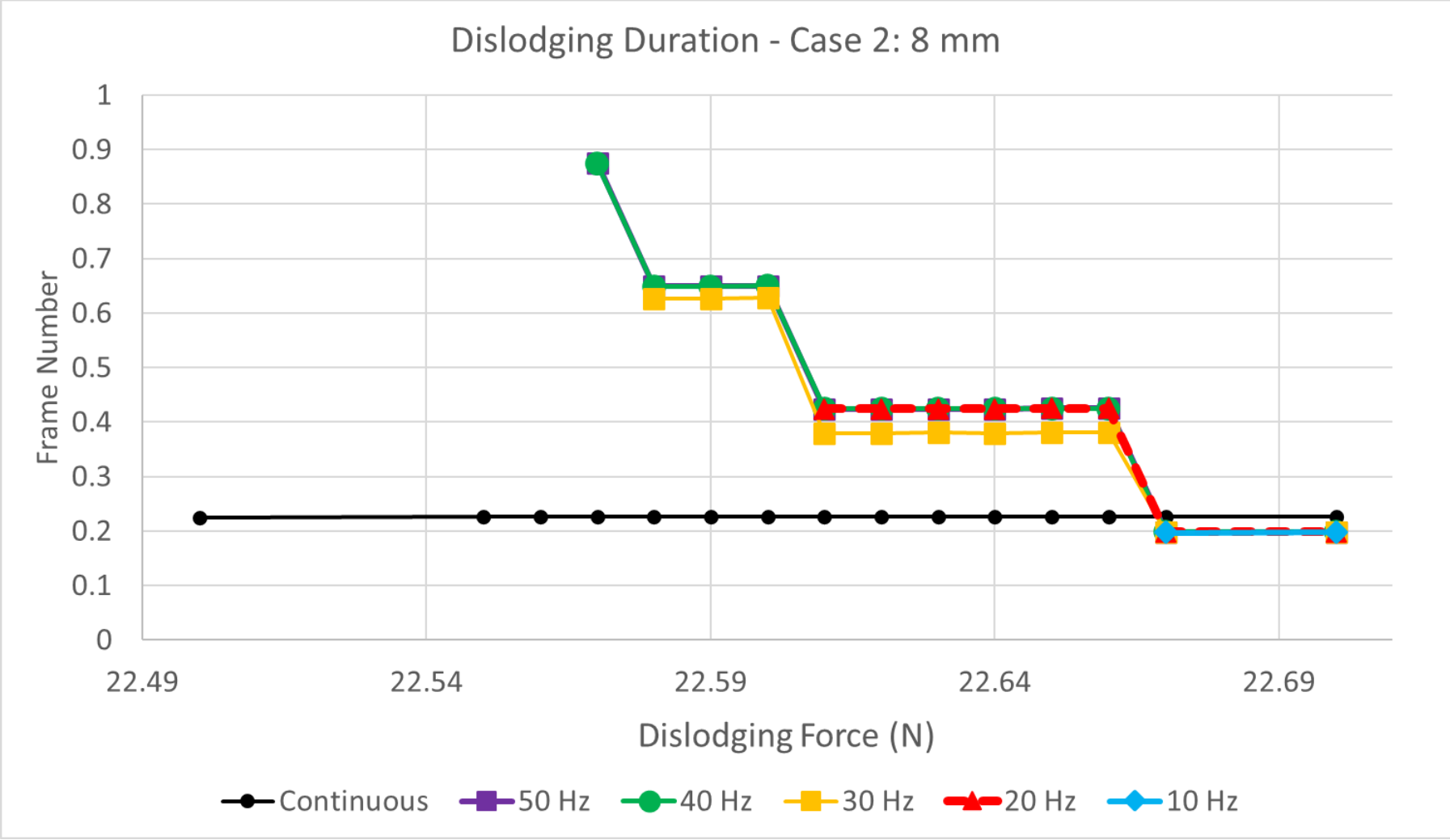

Figure 4-10. Impulse required to dislodge the peg – Case 2 (Magnified)

The sudden small drop in impulse when the pulling force magnitude is at 21.50 N in case 1 and 23.90 N in case 2 is due to the decrease in the duration of peg dislodging. The dislodgement frame number drops from 3 to 2 when the pulling magnitude increases from 21.50 N to 21.51 N for case 1 and from 23.89 N to 23.90 N for case 2. This is the limitation of using simulation.

Although applying higher magnitudes of pulling force to dislodge the peg requires a much lower impulse when compared to lower magnitudes, there is a risk of damaging the components. Based on the simulation result, it is shown that within a certain range, using pulsating force to dislodge the peg is beneficial compared to using a continuous force. To achieve low impulse, the pulling force must be at a minimum magnitude.

4.4 Summary

An investigation of peg dislodging has been carried out. Based on human intuition, when a peg is stuck, the natural way to dislodge the peg is to shake it and pull it out of the hole. However, in regard to small clearance and to avoid damaging the peg and hole, an upwards or vertical force is applied.

Depending on the nature of the disassembly process, some would prefer a lower pulling magnitude to dislodge the wedged peg to have better control over the disassembly process, and to avoid damaging the components, some would prefer a shorter disassembly time, and preserving the quality of the components may not be of interest.

Unlike press fit components, which have surface contact along the components, peg-hole wedging only has 2-point contact. Thus, the parameters used in the analysis are critical, and simulation is the preferred method of investigating this problem as it is sensitive.

There were two simulation setups in this study using the same peg-hole geometry, where the peg insertion depths were 7 mm (case 1) and 8 mm (case 2) in each case study. The peg was systematically wedged with 1000 Nmm and 1500 Nmm.

To investigate the parameters that produce the low impulse, the wedged peg is pulled using different methods: by a continuous force and with pulses of different frequencies (10 Hz to 50 Hz). The process of dislodging is repeated with different magnitudes of forces.

The results show that to dislodge the peg with low impulse, the magnitude of the pulling force should fall within a specific range. The use of pulsating force is only beneficial in the low magnitude region. However, when the magnitude is in the lowest region, the use of continuous pulling force required a short duration to dislodge the peg, which resulted in low impulse compared to using pulsating force.

Chapter 5

The Passive Compliant Gough-Whitehall-Stewart Mechanism for Peg-Hole Assembly and Disassembly.

5.1 Preliminaries

In (McCallion, et al., 1979), the compliant device is designed based on the Gough-Whitehall-Stewart Platform (Gough & Whitehall, 1962), (Stewart, 1965). The compliance centre of the device is on the top plate.

An improved version of the compliant device is investigated in this chapter by lowering the top plate, which will then possess the properties of an RCC device. This improved design was patented in 1985, and the full description can be found in (Pham, 1985). However, there has not been an analysis of the patented device; therefore, the analysis in this chapter is required to prove the location compliance centre.

This design can be applicable for peg-hole assembly and disassembly. The links used in both designs are double-acting cylinders with ball joints, as shown in Figure 5-1. Figure 5-2 depicts the compliant device used in (McCallion, et al., 1979).

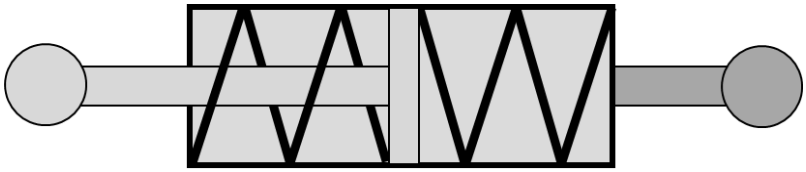

Figure 5-1. Double-acting cylinder

The use of double-acting cylinders is more economically friendly compared to ESPs in commercial RCC devices. The current available RCC design can only withstand compressive forces, and the proposed design in this chapter can resist both compressive and tensile forces, which allows the device to provide compliance for both peg insertion and extraction.

This investigation aims to understand the accuracy of the remodelled approximation matrix for the new design. The method used is similar to (McCallion, et al., 1979), which is formulating a simplified model for the new device using a small approximation. Then, the theoretical model is validated numerically.

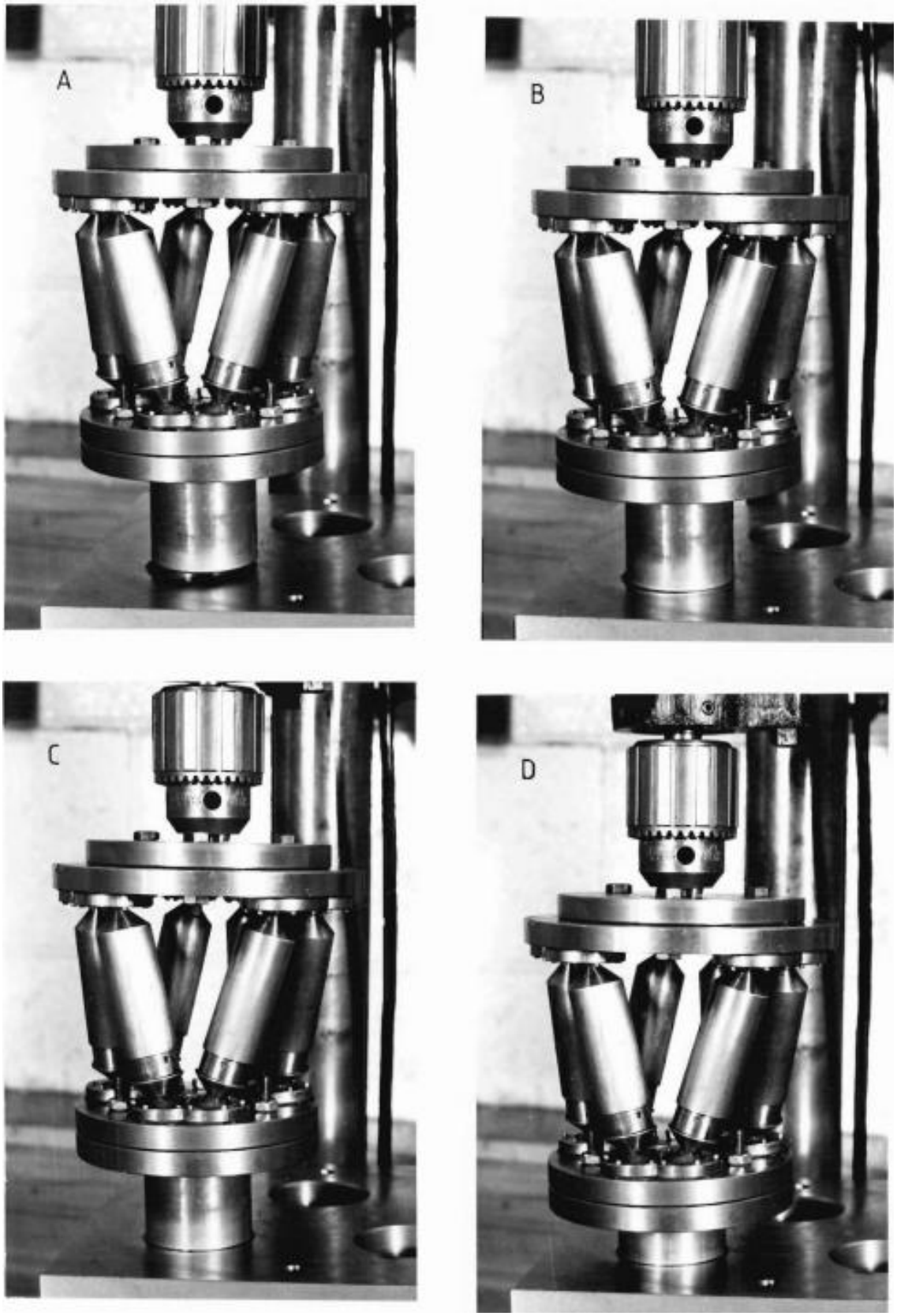

Figure 5-2. The compliance device in (McCallion, et al., 1979)

The approximation matrix will then be subjected to further tests. In the first scenario, the length of the peg is slightly longer. This is only considered in the numerical validation model and not in the approximation model. Then, the results from both calculations are compared. The second scenario is similar but with a slightly shorter peg. The last scenario is different. A simulation is carried out, and the results are compared.

The sensitivity analysis has confirmed the correctness of the small motion assumptions and the RCC properties of the new compliance device, the double-acting springs of which render it suitable for use in disassembly operations.

5.2 Theoretical Models

5.2.1 The Approximation Model

As mentioned, the new device is a modified version of the compliant device in (McCallion, et al., 1979), which was inspired by the Gough-Whitehall-Stewart mechanism (Gough & Whitehall, 1962), (Stewart, 1965).

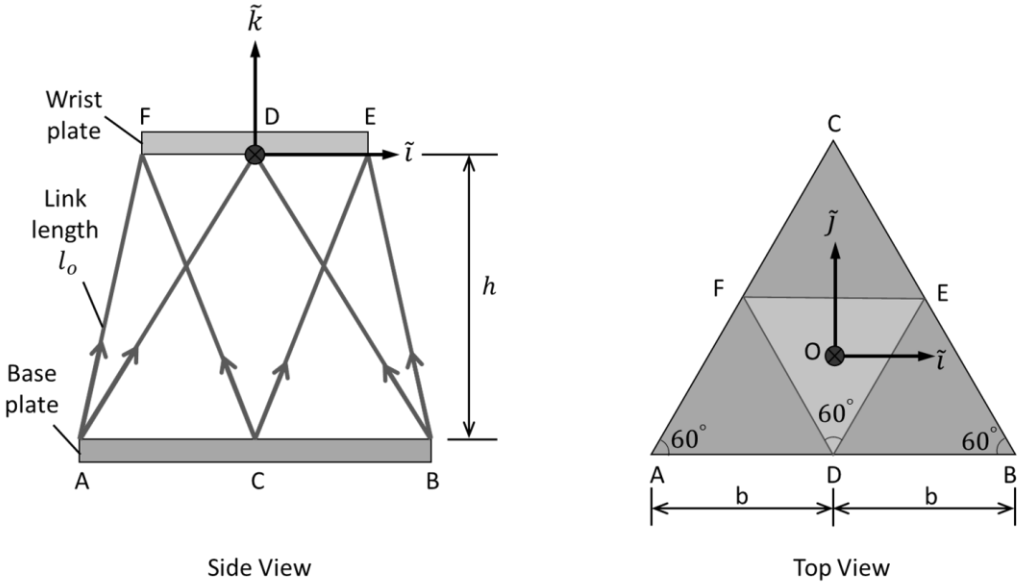

Figure 5-3. Simplified geometry of the compliant device (McCallion, et al., 1979)

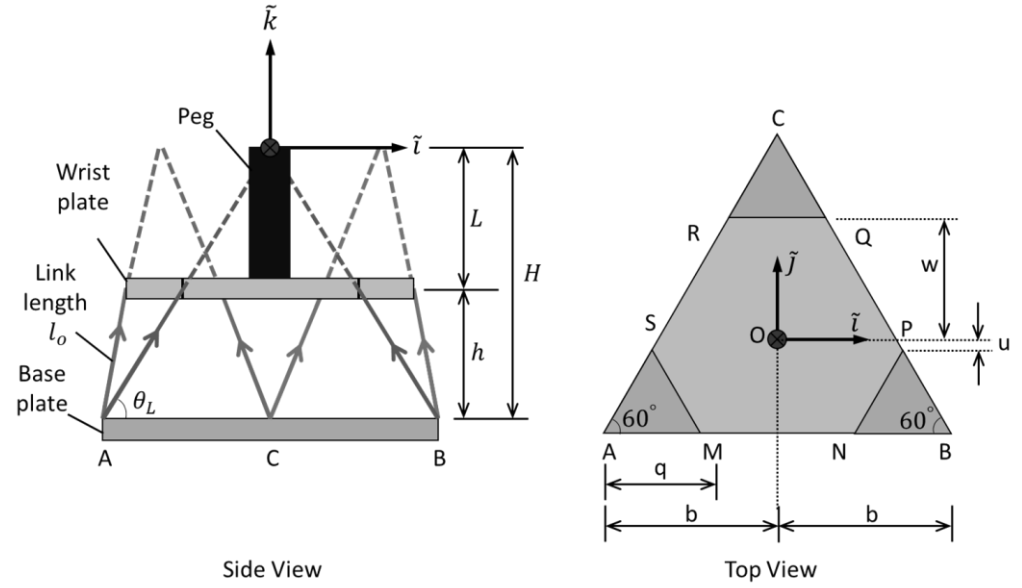

Figure 5-4. Simplified geometry of the new device

The main difference between the compliant device from (McCallion, et al., 1979) and the new device is that the wrist plate has been lowered by L, which makes the centre of rotation remote, and the tip of the peg will be the centre compliance. In the new device, there are six edges/joints instead of three on the wrist plate.

With this model, all joints between two links are at the same point, but this is not the case in practice. It is also assumed that all joints are frictionless, there is no bending moment acting on the links, and the compressive/tensile forces act along the links. Similar to (McCallion, et al., 1979), this model is only recommended for small translation and rotational errors, and this is dependent on the dimension of the end effector of the robot/machine and the size of the peg. The stiffnesses of all links are considered to be the same.

The new device has six degrees of freedom, which is derived in the appendix. The flexibility matrix [C] of the device about a set of orthogonal axes $(\tilde{\imath}, \tilde{\jmath}, \tilde{k})$ is approximated to a diagonal matrix as follows:

$$\begin{bmatrix} x \\ y \\ z \\ \theta_x \\ \theta_y \\ \theta_z \end{bmatrix} = \begin{bmatrix} C_{11} & 0 & 0 & 0 & 0 & 0 \\ 0 & C_{22} & 0 & 0 & 0 & 0 \\ 0 & 0 & C_{33} & 0 & 0 & 0 \\ 0 & 0 & 0 & C_{44} & 0 & 0 \\ 0 & 0 & 0 & 0 & C_{55} & 0 \\ 0 & 0 & 0 & 0 & 0 & C_{66} \end{bmatrix} \begin{bmatrix} F_x \\ F_y \\ F_z \\ M_x \\ M_y \\ M_z \end{bmatrix} \tag{5.1}$$

where x, y, z are the small translations and $\theta_x, \theta_y, \theta_z$ are the small rotations along and about $(\tilde{\imath}, \tilde{\jmath}, \tilde{k})$ respectively; C_{mm}'s are the flexibility constants, which depend on the dimension of the device and the stiffness of the springs; and $F_x, F_y, F_Z, M_x, M_y, M_z$ are the forces and moments projected in $(\tilde{\imath}, \tilde{\jmath}, \tilde{k})$.

This model is simplified and can be easily applied. Although the derivation is shorter than the actual calculation, it is still able to produce a good approximation that is close to the real values.

The fixed variables are divided into two tiers:

a. Primary fixed variables, which are decided:

$$Base\ length, b$$

$$Peg\ length, L$$

$$Link's\ tilting\ angle, \theta_L \tag{5.2}$$

$$Spring\ constant, k$$

b. Secondary fixed variables, which are calculated based on the primary fixed variable:

$$H = b \times \tan\theta_L \tag{5.3}$$

$$h = H - L \tag{5.4}$$

$$l_o = \frac{h}{\sin\theta_L} \tag{5.5}$$

$$q = \frac{h}{\tan\theta_L} \tag{5.6}$$

$$u = \frac{q\sqrt{3}}{2} - \frac{b\sqrt{3}}{3} \tag{5.7}$$

$$w = \frac{4b\sqrt{3} - 3q\sqrt{3}}{6} \tag{5.8}$$

However, the manipulated variables would be the translation and rotation $x, y, z, \theta_x, \theta_y, and\ \theta_z$. Then, $F_x, F_y, F_Z, M_x, M_y, M_z$ are the responding variables. This would better describe the effects of misalignments on the device. The model results will then be compared to the numerical results.

The coordinates about the global axes are listed below:

$$OA = \left(-b \;,\; \frac{-b\sqrt{3}}{3} \;,\; -H \right)$$

$$OB = \left(b \;,\; \frac{-b\sqrt{3}}{3} \;,\; -H \right)$$

$$OC = \left(0 \;,\; \frac{2b\sqrt{3}}{3} \;,\; -H \right)$$

$$OM = \left(-(b-q) \;,\; \frac{-b\sqrt{3}}{3} \;,\; -L \right)$$

$$ON = \left((b-q) \;,\; \frac{-b\sqrt{3}}{3} \;,\; -L \right)$$

$$OP = \left((b-\frac{q}{2}) \;,\; u \;,\; -L \right)$$

$$OQ = \left(\frac{q}{2} \;,\; w \;,\; -L \right)$$

$$OR = \left(-\frac{q}{2} \quad , \quad w \quad , \quad -L \right)$$

$$OS = \left(-(b - \frac{q}{2}) \quad , \quad u \quad , \quad -L \right)$$

Link 1: $\overrightarrow{l_1} = \overrightarrow{AM} = \overrightarrow{OM} - \overrightarrow{OA}$

Link 2: $\overrightarrow{l_2} = \overrightarrow{BN} = \overrightarrow{ON} - \overrightarrow{OB}$

Link 3: $\overrightarrow{l_3} = \overrightarrow{BP} = \overrightarrow{OP} - \overrightarrow{OB}$

Link 4: $\overrightarrow{l_4} = \overrightarrow{CQ} = \overrightarrow{OQ} - \overrightarrow{OC}$

Link 5: $\overrightarrow{l_5} = \overrightarrow{CR} = \overrightarrow{OR} - \overrightarrow{OC}$

Link 6: $\overrightarrow{l_6} = \overrightarrow{AS} = \overrightarrow{OS} - \overrightarrow{OA}$

The method to find the flexibility matrix [C] is similar to (McCallion, et al., 1979):

1. The local stiffness matrix [s] of the device is found by using the coordinate system listed above, and the local displacement vector, $\overrightarrow{\Delta l}$, is defined. Since the forces act along the links, the local coordinate system is used instead.

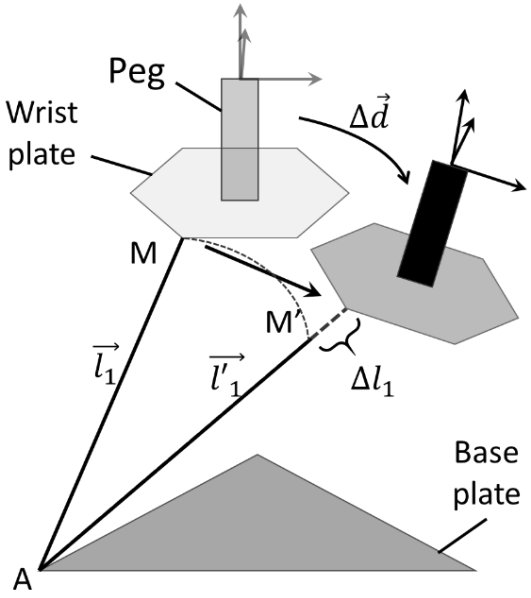

Figure 5-5. Link vectors and the displacement of the wrist plate

The local stiffness matrix of the device is shown below:

$$[\mathrm{s}] = k[I] \tag{5.9}$$

where k is the spring constant and $[I]$ is the 6×6 identity matrix.

The local displacement Δl_m is the small change in the length of link m caused by the axial link forces; l_m is the length of the link and $\overrightarrow{l_m}$ is the link vector. Then, assuming the translation and rotation, $\left(\overrightarrow{l_m'} - \overrightarrow{l_m}\right)$, the change is small, and the relationship below is established.

$$l_m{}^2 = \overrightarrow{l_m}^2 \tag{5.10}$$

$$l_m \, \Delta l_m \approx \overrightarrow{l_m} \cdot \left(\overrightarrow{l_m'} - \overrightarrow{l_m}\right) \tag{5.11}$$

where $\overrightarrow{l_m{}'}$ is the link vector of link m after its length has changed by Δl_m. Since all links have the same initial length,

$$l_m = l_o \tag{5.12}$$

$$\Delta l_m \approx \frac{\overrightarrow{l_m} \cdot \left(\overrightarrow{l_m{}'} - \overrightarrow{l_m}\right)}{l_o} \tag{5.13}$$

2. The compatibility matrix [a] is derived from the displacements of joints in the local and global coordinate systems. Let $\Delta\vec{d}$ be the displacement of the wrist plate in the global coordinate system as shown in Figure 5-5.

$$\Delta\vec{d} = \begin{bmatrix} x \\ y \\ z \\ \theta_x \\ \theta_y \\ \theta_z \end{bmatrix} \tag{5.14}$$

$$\Delta\vec{l} = \begin{bmatrix} \Delta l_1 \\ \Delta l_2 \\ \Delta l_3 \\ \Delta l_4 \\ \Delta l_5 \\ \Delta l_6 \end{bmatrix} \tag{5.15}$$

$$\Delta\vec{l} = [\mathrm{a}]\,\Delta\vec{d} \tag{5.16}$$

Using Equation (5.13) and solving $\overrightarrow{l_m{}'}$ as linear functions of $(x, y, z, \theta_x, \theta_y, \theta_z)$, the coefficient a_{mn} can be obtained. Using Link 1, an example of the calculation for obtaining the first row of $[a]$ is shown below.

$$\overrightarrow{l_1'} = \overrightarrow{OM'} - \overrightarrow{OA} \tag{5.17}$$

where $\overrightarrow{OM'}$ is the vector of joint M on the wrist plate after translation and rotation,

$$\overrightarrow{OM'} = [R]\,\overrightarrow{OM} + [\vec{t}] \tag{5.18}$$

$$[R] = \begin{bmatrix} 1 & -\theta_z & \theta_y \\ \theta_z & 1 & -\theta_x \\ -\theta_y & \theta_x & 1 \end{bmatrix} \tag{5.19}$$

$$\left[\overrightarrow{OM}\right] = \begin{bmatrix} -(b-q) \\ \dfrac{-b\sqrt{3}}{3} \\ -L \end{bmatrix} \tag{5.20}$$

$$[\vec{t}] = \begin{bmatrix} x \\ y \\ z \end{bmatrix} \tag{5.21}$$

$$\left[\overrightarrow{OA}\right] = \begin{bmatrix} -b \\ \dfrac{-b\sqrt{3}}{3} \\ -H \end{bmatrix} \tag{5.22}$$

Then, substituting Equations (5.18) to (5.22) into Equation (5.17) yields:

$$\overrightarrow{l_1'} = \begin{bmatrix} q + \dfrac{b\sqrt{3}}{3}\theta_z - L\theta_y + x \\ -(b-q)\theta_z + L\theta_x + y \\ (b-q)\theta_y - \dfrac{b\sqrt{3}}{3}\theta_z + z + h \end{bmatrix} \tag{5.23}$$

The vector $\overrightarrow{l_1}$ is the link between Joints A and M,

$$\begin{aligned}\overrightarrow{l_1} &= \overrightarrow{OM} - \overrightarrow{OA} \\ &= \begin{bmatrix} -(b-q) \\ \frac{b\sqrt{3}}{3} \\ -L \end{bmatrix} - \begin{bmatrix} -b \\ \frac{b\sqrt{3}}{3} \\ -H \end{bmatrix} \\ &= \begin{bmatrix} q \\ 0 \\ h \end{bmatrix}\end{aligned} \tag{5.24}$$

Using Equation (5.13),

$$\begin{aligned}\overrightarrow{l_1'} - \overrightarrow{l_1} &= \begin{bmatrix} q + \frac{b\sqrt{3}}{3}\theta_z - L\theta_y + x \\ -(b-q)\theta_z + L\theta_x + y \\ (b-q)\theta_y - \frac{b\sqrt{3}}{3}\theta_x + z + h \end{bmatrix} - \begin{bmatrix} q \\ 0 \\ h \end{bmatrix} \\ &= \begin{bmatrix} \frac{b\sqrt{3}}{3}\theta_z - L\theta_y + x \\ -(b-q)\theta_z + L\theta_x + y \\ (b-q)\theta_y - \frac{b\sqrt{3}}{3}\theta_x + z \end{bmatrix}\end{aligned} \tag{5.25}$$

$$\overrightarrow{l_1} \cdot \left(\overrightarrow{l_1'} - \overrightarrow{l_1}\right) = \left(\frac{bq\sqrt{3}}{3}\theta_z - Lq\theta_y + qx + h(b-q)\theta_y - \frac{bh\sqrt{3}}{3}\theta_x + hz\right) \tag{5.26}$$

Substituting Equation (5.26) into Equation (5.13),

$$\Delta l_1 \approx \frac{1}{l_o}\left(\frac{bq\sqrt{3}}{3}\theta_z - Lq\theta_y + qx + h(b-q)\theta_y - \frac{bh\sqrt{3}}{3}\theta_x + hz\right) \tag{5.27}$$

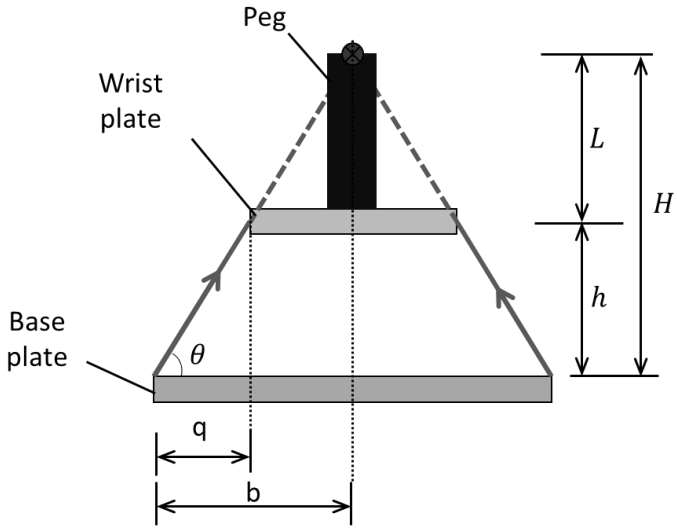

Figure 5-6. Relationship between geometry

Note that

$$\tan\theta = \frac{H}{b} = \frac{h}{q}$$

$$Hq = hb$$

Therefore, the first line of $[a]$ is

$$\left[q \quad 0 \quad h \quad -\frac{bh\sqrt{3}}{3} \quad 0 \quad \frac{bq\sqrt{3}}{3}\right] \tag{5.28}$$

Repeating this process for the five other links, the entire matrix $[a]$ is:

$$[a] = \begin{bmatrix} q & 0 & h & -\frac{bh\sqrt{3}}{3} & 0 & \frac{bq\sqrt{3}}{3} \\ -q & 0 & h & -\frac{bh\sqrt{3}}{3} & 0 & -\frac{bq\sqrt{3}}{3} \\ -\frac{q}{2} & \frac{q\sqrt{3}}{2} & h & \frac{bh\sqrt{3}}{6} & \frac{-bh}{2} & \frac{bq\sqrt{3}}{3} \\ \frac{q}{2} & -\frac{q\sqrt{3}}{2} & h & \frac{bh\sqrt{3}}{6} & \frac{-bh}{2} & -\frac{bq\sqrt{3}}{3} \\ -\frac{q}{2} & -\frac{q\sqrt{3}}{2} & h & \frac{bh\sqrt{3}}{6} & \frac{bh}{2} & \frac{bq\sqrt{3}}{3} \\ \frac{q}{2} & \frac{q\sqrt{3}}{2} & h & \frac{bh\sqrt{3}}{6} & \frac{bh}{2} & -\frac{bq\sqrt{3}}{3} \end{bmatrix} \quad (5.29)$$

3. The global stiffness matrix $[S]$ is established through the relationship below, where $[a]^T$ is the transpose matrix of $[a]$.

$$[S] = [a]^T [s] [a] \quad (5.30)$$

Substituting Equations (5.9) and (5.29) into Equation(5.30),

$$[S] = \frac{k}{l_o^2} \begin{bmatrix} 3q^2 & 0 & 0 & 0 & 0 & 0 \\ 0 & 3q^2 & 0 & 0 & 0 & 0 \\ 0 & 0 & 6h^2 & 0 & 0 & 0 \\ 0 & 0 & 0 & b^2h^2 & 0 & 0 \\ 0 & 0 & 0 & 0 & b^2h^2 & 0 \\ 0 & 0 & 0 & 0 & 0 & 2b^2q^2 \end{bmatrix} \quad (5.31)$$

4. The flexibility matrix $[C]$ is the inverse of the global stiffness matrix $[S]$.

$$[C] = \frac{l_o^2}{k}\begin{bmatrix} \frac{1}{3q^2} & 0 & 0 & 0 & 0 & 0 \\ 0 & \frac{1}{3q^2} & 0 & 0 & 0 & 0 \\ 0 & 0 & \frac{1}{6h^2} & 0 & 0 & 0 \\ 0 & 0 & 0 & \frac{1}{b^2h^2} & 0 & 0 \\ 0 & 0 & 0 & 0 & \frac{1}{b^2h^2} & 0 \\ 0 & 0 & 0 & 0 & 0 & \frac{1}{2b^2q^2} \end{bmatrix} \tag{5.32}$$

Finally, substituting Equation (5.32) into Equation (5.1),

$$\begin{bmatrix} x \\ y \\ z \\ \theta_x \\ \theta_y \\ \theta_z \end{bmatrix} = \frac{l_o^2}{k}\begin{bmatrix} \frac{1}{3q^2} & 0 & 0 & 0 & 0 & 0 \\ 0 & \frac{1}{3q^2} & 0 & 0 & 0 & 0 \\ 0 & 0 & \frac{1}{6h^2} & 0 & 0 & 0 \\ 0 & 0 & 0 & \frac{1}{b^2h^2} & 0 & 0 \\ 0 & 0 & 0 & 0 & \frac{1}{b^2h^2} & 0 \\ 0 & 0 & 0 & 0 & 0 & \frac{1}{2b^2q^2} \end{bmatrix}\begin{bmatrix} F_x \\ F_y \\ F_z \\ M_x \\ M_y \\ M_z \end{bmatrix} \tag{5.33}$$

5.2.2 Numerical Validation Model

To validate the approximation model, a set of numerical models is derived. The change in the position of joints in the global coordinate system can be calculated because the position of the joints with respect to the remote centre is known and the manipulated translations and rotations of the remote centre are also known.

The base plate is assumed to be fixed, and the wrist plate is the one that moves. Let θ be the rotation introduced. Using Link 1 as an example, the translation and rotation of Joint M are calculated as follows:

$$\overrightarrow{\mathrm{OM}'} = [R_z(\theta_z)] \cdot \left[R_y(\theta_y)\right] \cdot [R_x(\theta_x)] \cdot \overrightarrow{OM} + [\vec{t}]$$

$$= \begin{bmatrix} \cos\theta_y \cos\theta_z & \cos\theta_z \sin\theta_x \sin\theta_y - \cos\theta_x \sin\theta_z & \sin\theta_x \sin\theta_z + \cos\theta_x \cos\theta_z \sin\theta_y \\ \cos\theta_y \sin\theta_z & \cos\theta_x \cos\theta_z + \sin\theta_x \sin\theta_y \sin\theta_z & \cos\theta_x \sin\theta_y \sin\theta_z - \cos\theta_z \sin\theta_x \\ -\sin\theta_z & \cos\theta_y \sin\theta_x & \cos\theta_x \cos\theta_y \end{bmatrix} \begin{bmatrix} -(b-q) \\ \frac{-b\sqrt{3}}{3} \\ -L \end{bmatrix} + \begin{bmatrix} x \\ y \\ z \end{bmatrix} \quad (5.34)$$

$$[R_x(\theta_x)] = \begin{bmatrix} 1 & 0 & 0 \\ 0 & \cos\theta_x & -\sin\theta_x \\ 0 & \sin\theta_x & \cos\theta_x \end{bmatrix} \quad (5.35)$$

$$\left[R_y(\theta_y)\right] = \begin{bmatrix} \cos\theta_y & 0 & \sin\theta_y \\ 0 & 1 & 0 \\ -\sin\theta_y & 0 & \cos\theta_y \end{bmatrix} \quad (5.36)$$

$$[R_z(\theta_z)] = \begin{bmatrix} \cos\theta_z & -\sin\theta_z & 0 \\ \sin\theta_z & \cos\theta_z & 0 \\ 0 & 0 & 1 \end{bmatrix} \quad (5.37)$$

Using Equation (5.17), the change in distance between the two points can be calculated.

The force acting along the link is calculated using the equation below and resolved in $(\tilde{\imath}, \tilde{\jmath}, \tilde{k})$ by using the link vector.

$$F_1 = k \times \Delta l_1 \tag{5.38}$$

where

$$\Delta l_1 = l_1' - l_o \tag{5.39}$$

Let $\overrightarrow{AM'}$ be the vector of Link 1 after translation/rotation,

$$\overrightarrow{AM'} = \begin{bmatrix} AM'_x \\ AM'_y \\ AM'_z \end{bmatrix} \tag{5.40}$$

and the length of Link 1,

$$\|AM'\| = \sqrt{AM_x^2 + AM_y^2 + AM_z^2} \tag{5.41}$$

To find the angle, ω, of vector Link 1 with respect to the axes, the method below is used.

$$\begin{aligned} \omega_x &= \cos^{-1} \frac{AM_x}{\|AM'\|} \\ \omega_y &= \cos^{-1} \frac{AM_y}{\|AM'\|} \end{aligned} \tag{5.42}$$

$$\omega_z = \cos^{-1}\frac{AM_z}{\|AM'\|}$$

Projecting the force along Link 1 onto the axes,

$$F_{1x} = F_1 \cos\omega_x$$

$$F_{1y} = F_1 \cos\omega_y \tag{5.43}$$

$$F_{1z} = F_1 \cos\omega_z$$

The process is repeated for the rest of the links. The sum of all the projected forces of each axis can now be compared with the approximation model for translation.

However, to calculate the moments caused by rotation, there is an extra step. The moments are also resolved in $(\tilde{\imath}, \tilde{\jmath}, \tilde{k})$ using the equation below:

$$\begin{aligned}\overrightarrow{M_1} &= \overrightarrow{r_1} \times \overrightarrow{F_1} \\ &= \begin{bmatrix} r_{1x} \\ r_{1y} \\ r_{1z} \end{bmatrix} \times \begin{bmatrix} F_{1x} \\ F_{1y} \\ F_{1z} \end{bmatrix}\end{aligned} \tag{5.44}$$

$$M_{1x} = r_{1y}F_{1z} - r_{1z}F_{1y}$$

$$M_{1y} = r_{1z}F_{1x} - r_{1x}F_{1z} \tag{5.45}$$

$$M_{1z} = r_{1x}F_{1y} - r_{1y}F_{1x}$$

where

$\vec{M}$ is the moment,

$\vec{r}$ is the vector between the remote centre to the joint on the Wrist Plate, and

$\vec{F}$ is the force vector, which is already calculated using Equation (5.43).

The calculation is repeated for the rest of the links, summing all the projected moments of each axis and comparing it with the approximation model for rotation.

5.2.3 Results: Comparison of models.

To compare the approximation model and numerical validation model, several tests have been carried out by changing the peg length, L, or the link tilting angle, θ_L. These tests not only compare the accuracy of the model but also show trends when L or θ_L changes.

In the first comparison, the peg length, L, changes from 50 mm to 60 mm, while the link tilting angle, θ_L, and the total height, H, remain the same, as shown in Figure 5-7.

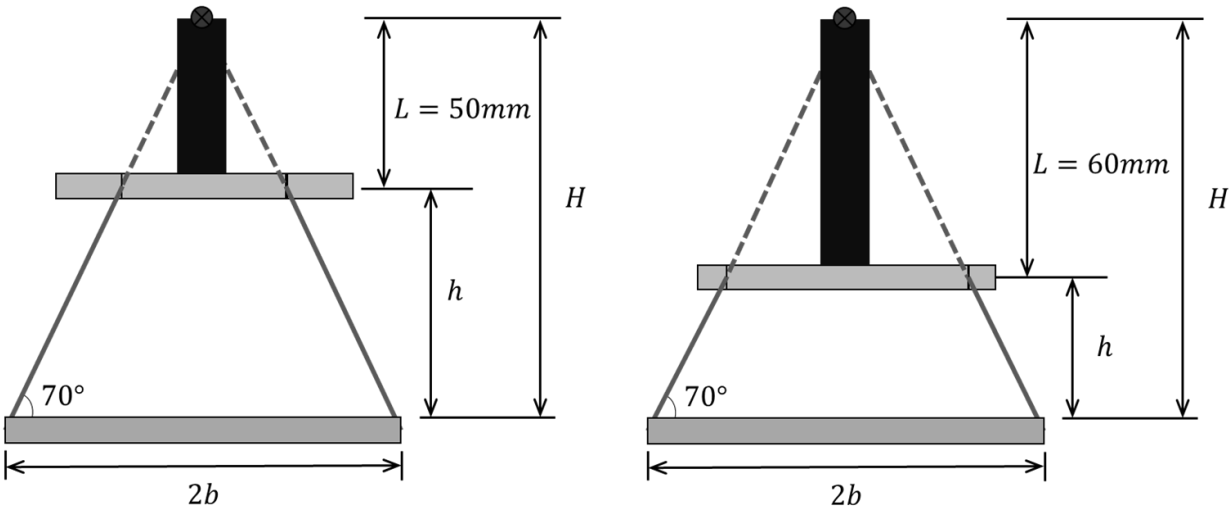

Figure 5-7. Comparison of different peg lengths

$$b = 50\ mm$$
$$L = 50mm\ Vs.\ 60mm$$
$$\theta_L = 70\ °$$
$$k = 200\ N/mm \tag{5.46}$$

After substituting Equation (5.46) into both models, the summary results are shown in Table 5-1 to Table 5-4. The full results are shown in Appendix C.

Table 5-1. Results of the first comparison for translation for $L = 50mm$.

Translation (mm)	Approximation Matrix						Numerical Validation Model						Error (%)
	ΣFx	ΣFy	ΣFz	ΣMx	ΣMy	ΣMz	ΣFx	ΣFy	ΣFz	ΣMx	ΣMy	ΣMz	
x = 0.1	7.0187	0	0	0	0	0	7.0187	0	0.05	0.1536	-0.008	0	0
x = 0.5	35.093	0	0	0	0	0	35.099	0	1.2499	3.8391	-0.983	-0.018	0.0168
x = 1.0	70.186	0	0	0	0	0	70.234	0	4.9995	15.353	-7.861	-0.142	0.0749
y = 0.1	0	7.0187	0	0	0	0	0	7.0187	0.05	-0.146	0	0	0
y = 0.5	0	35.093	0	0	0	0	0	35.099	1.2499	-2.857	0	0	0.0168
y = 1.0	0	70.187	0	0	0	0	0	70.234	4.9995	-7.493	0	0	0.0667
z = 0.1	0	0	105.96	0	0	0	0	0	105.98	0	0	0	0.0200
z = 0.5	0	0	529.81	0	0	0	0	0	530.34	0	0	0	0.0998
z = 1.0	0	0	1059.6	0	0	0	0	0	1061.7	0	0	0	0.1982

Table 5-2. Results of the first comparison for rotation for $L = 50mm$.

Rotation (Rad)	Approximation Matrix						Numerical Validation Model						Error (%)
	ΣFx	ΣFy	ΣFz	ΣMx	ΣMy	ΣMz	ΣFx	ΣFy	ΣFz	ΣMx	ΣMy	ΣMz	
Rx = 0.005	0	0	0	2207.6	0	0	0	-0.025	1.1324	2210.6	0	0	0.1345
Rx = 0.02	0	0	0	8830.2	0	0	0	-0.267	18.116	8895.1	0	0	0.7348
Rx = 0.05	0	0	0	22076	0	0	0	-0.100	113.14	2268	0	0	2.7678
Ry = 0.005	0	0	0	0	2207.6	0	-0.003	0.0272	1.1324	-2.666	2207.9	-0.014	0.0138
Ry = 0.02	0	0	0	0	8830.2	0	-0.168	0.4343	18.116	-42.63	8852.5	-0.894	0.2525
Ry = 0.05	0	0	0	0	22076	0	-2.618	2.7092	113.14	-265.4	22423	-13.93	1.5727
Rz = 0.005	0	0	0	0	0	584.89	0	0	0.2199	0	0	584.9	0.0014
Rz = 0.02	0	0	0	0	0	2339.6	0	0	3.5188	0	0	2340.0	0.0205
Rz = 0.05	0	0	0	0	0	5848.9	0	0	21.987	0	0	5857.1	0.140

Table 5-3. Results of the first comparison for translation for $L = 60mm$

Translation (mm)	Approximation Matrix						Numerical Validation Model						Error (%)
	ΣFx	ΣFy	ΣFz	ΣMx	ΣMy	ΣMz	ΣFx	ΣFy	ΣFz	ΣMx	ΣMy	ΣMz	
x = 0.1	7.0187	0	0	0	0	0	7.0187	0	0.0565	-0.010	-0.004	0	0
x = 0.5	35.093	0	0	0	0	0	35.101	0	1.4115	4.3352	-1.253	-0.023	0.0214
x = 1.0	70.187	0	0	0	0	0	70.246	0	5.6456	17.337	-10.02	-0.180	0.0851
y = 0.1	0	7.0187	0	0	0	0	0	7.0187	0.0565	-0.163	0	0	0
y = 0.5	0	35.093	0	0	0	0	0	35.101	1.4115	-3.082	0	0	0.0214
y = 1.0	0	70.187	0	0	0	0	0	70.246	5.6456	-7.313	0	0	0.0850
z = 0.1	0	0	105.96	0	0	0	0	0	105.99	0	0	0	0.0227
z = 0.5	0	0	529.81	0	0	0	0	0	530.41	0	0	0	0.1126
z = 1.0	0	0	1059.6	0	0	0	0	0	1062	0	0	0	0.2265

Table 5-4. Results of the first comparison for rotation for $L = 60mm$.

Rotation (Rad)	Approximation Matrix						Numerical Validation Model						Error (%)
	ΣFx	ΣFy	ΣFz	ΣMx	ΣMy	ΣMz	ΣFx	ΣFy	ΣFz	ΣMx	ΣMy	ΣMz	
Rx = 0.005	0	0	0	2207.6	0	0	0	-0.027	1.5295	2211.9	0	0	0.1964
Rx = 0.02	0	0	0	8830.2	0	0	0	-0.191	24.467	8933.5	0	0	1.1699
Rx = 0.05	0	0	0	22076	0	0	0	1.8539	152.74	23132	0	0	4.7841
Ry = 0.005	0	0	0	0	2207.6	0	-0.005	0.0323	1.5295	-3.685	2208.3	-0.023	0.0295
Ry = 0.02	0	0	0	0	8830.2	0	-0.326	0.5165	24.46	-58.91	8874.7	-1.459	0.5035
Ry = 0.05	0	0	0	0	22076	0	-5.089	3.2182	152.73	-366.2	22769	-22.69	3.1378
Rz = 0.005	0	0	0	0	0	584.89	0	0	0.2795	0	0	584.91	0.0033
Rz = 0.02	0	0	0	0	0	2339.6	0	0	4.4719	0	0	2340.8	0.051
Rz = 0.05	0	0	0	0	0	5848.9	0	0	27.939	0	0	5868.2	0.3300

In the second comparison, θ_L changes, while the rest of the variables remain the same, as shown in Figure 5-8.

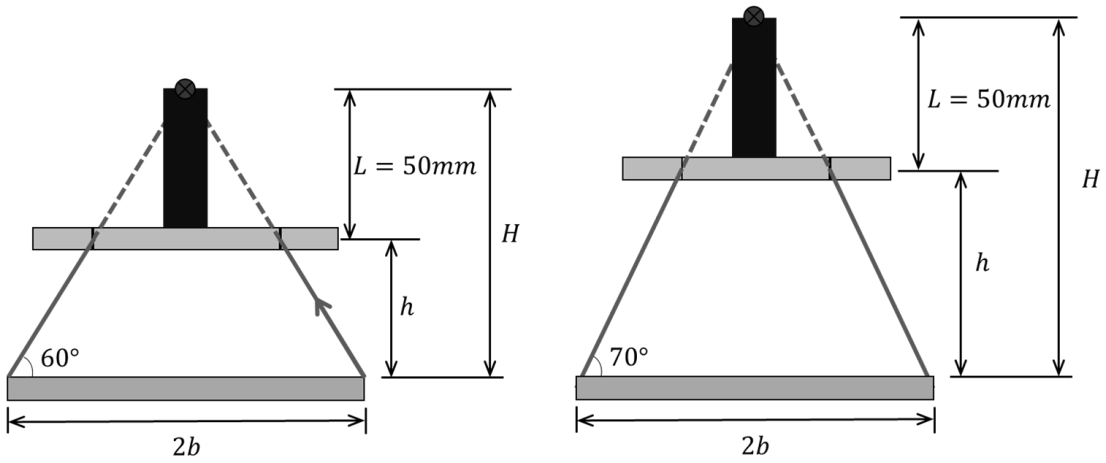

Figure 5-8. Comparison of different link tilting angles

$$b = 50\ mm$$
$$L = 50\ mm$$
$$\theta_L = \ 60\ ^\circ Vs.\ 70\ ^\circ \tag{5.47}$$
$$k = 200\ N/mm$$

After substituting Equation (5.47) into both models, the summary results are shown in Table 5-5 to Table 5-8. The full results are shown in Appendix C.

Table 5-5. Results of the second comparison for translation for $\theta_L = 60°$

Translation (mm)	Approximation Matrix						Numerical Validation Model						Error (%)
	ΣFx	ΣFy	ΣFz	ΣMx	ΣMy	ΣMz	ΣFx	ΣFy	ΣFz	ΣMx	ΣMy	ΣMz	
x = 0.1	15	0	0	0	0	0	15.000	0	0.0768	0.6654	-0.018	-0.001	0.0008
x = 0.5	75	0	0	0	0	0	75.015	0	1.921	16.632	-2.273	-0.133	0.0389
x = 1.0	150	0	0	0	0	0	150.12	0	7.6838	66.485	-18.18	-1.056	0.0822
y = 0.1	0	15	0	0	0	0	0	15.000	0.0768	-0.647	0	0	0.0008
y = 0.5	0	75	0	0	0	0	0	75.015	1.9210	-14.36	0	0	0.0206
y = 1.0	0	150	0	0	0	0	0	150.12	7.6838	-48.29	0	0	0.0822
z = 0.1	0	0	90	0	0	0	0	0	90.092	0	0	0	0.1022
z = 0.5	0	0	450	0	0	0	0	0	452.28	0	0	0	0.5059
z = 1.0	0	0	900	0	0	0	0	0	909.0	0	0	0	0.9993

Table 5-6. Results of the second comparison for rotation for $\theta_L = 60°$.

Rotation (Rad)	Approximation Matrix						Numerical Validation Model						Error (%)
	ΣFx	ΣFy	ΣFz	ΣMx	ΣMy	ΣMz	ΣFx	ΣFy	ΣFz	ΣMx	ΣMy	ΣMz	
Rx = 0.005	0	0	0	1875	0	0	0	-0.092	1.6490	1884.1	0	0	0.4844
Rx = 0.02	0	0	0	7500	0	0	0	-1.020	26.386	7686.3	0	0	2.4844
Rx = 0.05	0	0	0	18750	0	0	0	-0.828	164.62	20414	0	0	8.872
Ry = 0.005	0	0	0	0	1875	0	-0.009	0.101	1.6487	-8.217	1875.9	-0.065	0.046
Ry = 0.02	0	0	0	0	7500	0	-0.596	1.6144	26.365	-131.2	7555.4	-4.139	0.7383
Ry = 0.05	0	0	0	0	18750	0	-9.281	10.035	164.3	-811.2	19613	-64.26	4.6011
Rz = 0.005	0	0	0	0	0	1250	0	0	0.5077	0	0	1250.1	0.0069
Rz = 0.02	0	0	0	0	0	5000	0	0	8.1219	0	0	5005.5	0.1107
Rz = 0.05	0	0	0	0	0	12500	0	0	50.737	0	0	12586	0.6921

Table 5-7. Results of the second comparison for translation for $\theta_L = 70°$.

Translation (mm)	Approximation Matrix						Numerical Validation Model						Error (%)
	ΣFx	ΣFy	ΣFz	ΣMx	ΣMy	ΣMz	ΣFx	ΣFy	ΣFz	ΣMx	ΣMy	ΣMz	
x = 0.1	7.0187	0	0	0	0	0	7.0187	0	0.05	0.1536	-0.008	0	0
x = 0.5	35.093	0	0	0	0	0	35.099	0	1.2499	3.8391	-0.983	-0.018	0.0168
x = 1.0	70.187	0	0	0	0	0	70.239	0	4.9995	15.354	-7.861	-0.142	0.0749
y = 0.1	0	7.0187	0	0	0	0	0	7.0187	0.05	-0.146	0	0	0
y = 0.5	0	35.093	0	0	0	0	0	35.099	1.2499	-2.857	0	0	0.0168
y = 1.0	0	70.187	0	0	0	0	0	70.234	4.9995	-7.493	0	0	0.0667
z = 0.1	0	0	105.96	0	0	0	0	0	105.98	0	0	0	0.0200
z = 0.5	0	0	529.81	0	0	0	0	0	530.34	0	0	0	0.0998
z = 1.0	0	0	1059.6	0	0	0	0	0	1061.7	0	0	0	0.1982

Table 5-8. Results of the second comparison for rotation for $\theta_L = 70°$.

Rotation (Rad)	Approximation Matrix						Numerical Validation Model						Error (%)
	ΣFx	ΣFy	ΣFz	ΣMx	ΣMy	ΣMz	ΣFx	ΣFy	ΣFz	ΣMx	ΣMy	ΣMz	
Rx = 0.005	0	0	0	2207.6	0	0	0	-0.025	1.1324	2210.6	0	0	0.1345
Rx = 0.02	0	0	0	8830.2	0	0	0	-0.267	18.116	8895.1	0	0	0.7348
Rx = 0.05	0	0	0	22076	0	0	0	-0.100	113.14	2268	0	0	2.7678
Ry = 0.005	0	0	0	0	2207.6	0	-0.003	0.0272	1.1324	-2.666	2207.9	-0.014	0.0138
Ry = 0.02	0	0	0	0	8830.2	0	-0.168	0.4343	18.116	-42.63	8852.5	-0.894	0.2525
Ry = 0.05	0	0	0	0	22076	0	-2.618	2.7092	113.14	-265.4	22423	-13.93	1.5727
Rz = 0.005	0	0	0	0	0	584.89	0	0	0.2199	0	0	584.9	0.0014
Rz = 0.02	0	0	0	0	0	2339.6	0	0	3.5188	0	0	2340.0	0.0205
Rz = 0.05	0	0	0	0	0	5848.9	0	0	21.987	0	0	5857.1	0.140

Several observations can be seen from the results. The errors between the approximation model and the numerical validation model are relatively small.

In the first comparison, the error increases when L increases from $50mm$ to $60mm$; in the second comparison, the error increases when θ_L decreases from $70°$ to 60 °. The length of the links decreases in both comparisons when the variables change. Therefore, the longer the links are, the better the approximation model works.

Based on experience and intuition, it is known that when the links are more vertical, it is easier for the wrist plate to translate horizontally on the x-y plane and to rotate about the z-axis; when the links are more tilted, i.e., θ_L decreases, it is more difficult to horizontally translate the wrist plate on the x-y plane and to rotate about the z-axis. This is shown from the amplitude of forces and moments in the second comparison from Table 5-5 to Table 5-8.

In both comparisons, when the translation and rotation decrease, the error between the two models approaches zero.

5.3 Sensitivity Analysis

McCallion et al. advised that the approximation model is not suitable for off-centered pegs, which are too long and have large diameters. This is due to the reaction forces on the tip of the peg that will counteract the effects of the secondary moments.

In this section, the approximation model will be put to test once again with different scenarios. In this scenario, the length of the peg, assuming the centre of rotation is at the tip of the peg, will be slightly shorter or longer. The difference in peg length will only be taken into account in the numerical validation model; however, in the approximation model, the length of the peg is assumed to be correct.

The variables in the first test are shown below:

$$b = 50\ mm$$
$$\theta_L = 70\ °$$
$$k = 200\ N/mm \tag{5.48}$$
$$L_{Approx.} = 50\ mm$$
$$L_{Num.Val.} = 47\ mm, 49\ mm, 51\ mm\ \&\ 53\ mm$$

After substituting the variables, the results are tabulated in Table A - 27 to Table A - 50 in Appendix C. For translations, the errors remain the same for all cases. When the compliance

centre translates along the X-axis, only the moment about the Y-axis changes, while the remaining forces and moments remain constant. A similar observation can be seen when the compliance centre was translating along the Y-axis. When the compliance centre translates along the Y-axis, the moment about the X-axis changes, while the other forces and moments remain constant. There are no differences in the results in regard to translating the compliance in the Z-direction, which was expected.

All forces and moments varied in regard to rotation; however, the changes were small. When the compliance centre is rotated about the X-axis, the forces acting along the Y- and Z-axes change in a uniform manner, as shown in Figure A - 11 in the Appendix. It becomes slightly more complex when the Y-axis rotation is introduced to the compliance centre. While the error of the moments about the Y-axis remains very small, there are small changes occurring on the rest of the forces and moments. This can be seen in Figure A - 12 to Figure A - 17 in Appendix C. Similar to before, the different heights of the compliance centre do not influence the results when it is rotating about the Z-axis.

5.4 Model Simulation

Using MATLAB Simscape, simulations were carried out, and the results were compared to the approximation model. To fit the ball joints on the base plate, the coordinate of the bottom of the links must be modified, which is shown in Figure 5-9. Without raising the position of the base plate, the two ball joints at each point (Points A, B and C) intersect.

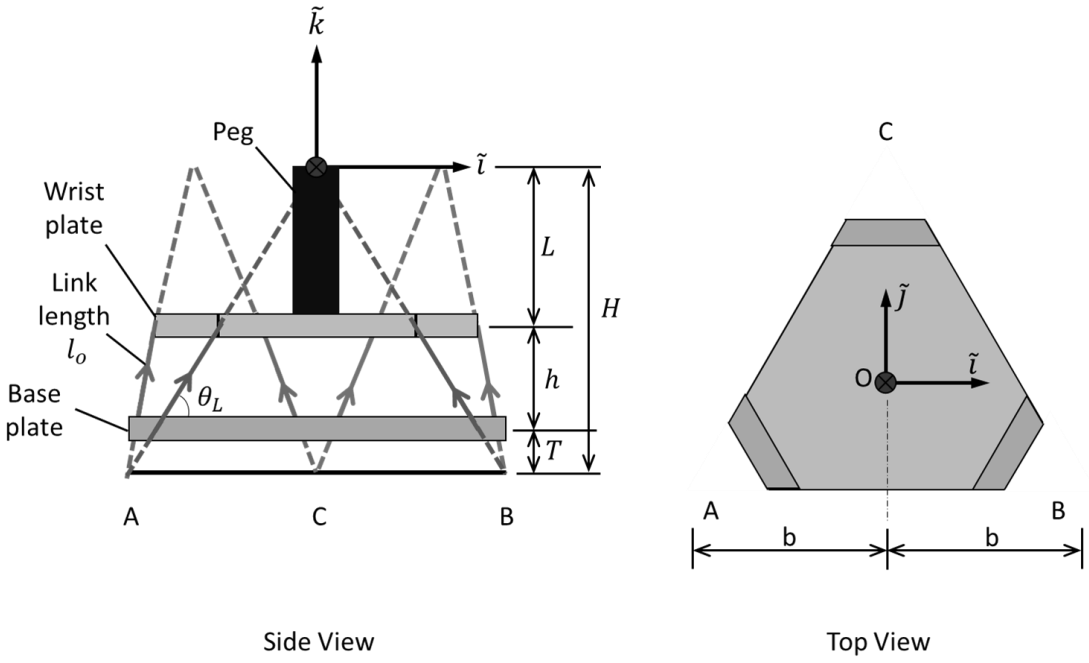

Figure 5-9. Simplified geometry of the new device in Simscape

$$b = 43.3\ mm$$

$$L = \ 25\ mm$$

$$h = \ 30\ mm$$

$$T = \ 20\ mm \tag{5.49}$$

$$\theta_L = 60\ °$$

$$K = \ 30\ N/mm$$

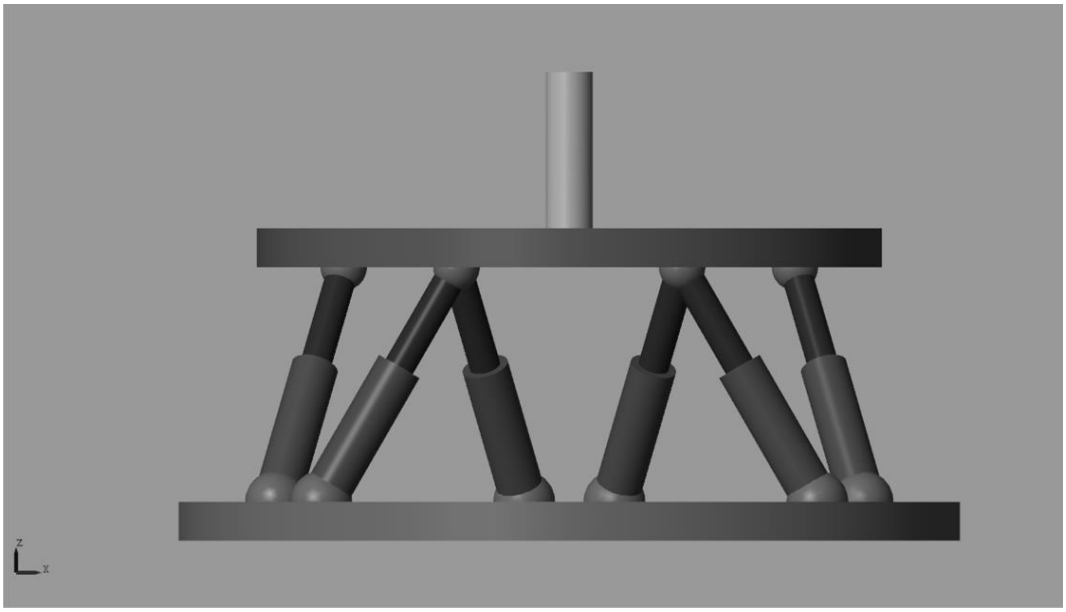

Figure 5-10. The new device was modelled in Simscape

Figure 5-10 shows the side view of the new device structure in Simscape. A different set of geometries was selected, as shown in Equation (5.49). However, the parameters used for the approximation model are shown in Equation (5.50).

$$b = 43.3\ mm$$

$$L = \ 25\ mm$$

$$h = \ 50\ mm$$

$$\theta_L = 60\ ° \qquad (5.50)$$

$$K = \ 30\ N/mm$$

$$l_o = 57.7530\ m$$

$$q = \ 28.8675\ mm$$

Substituting Equation (5.50) into Equation (5.33), the approximation model for comparison is shown in Equation (5.51).

$$\begin{bmatrix} x \\ y \\ z \\ \theta_x \\ \theta_y \\ \theta_z \end{bmatrix} = 111.111 \begin{bmatrix} 0.0004 & 0 & 0 & 0 & 0 & 0 \\ 0 & 0.0004 & 0 & 0 & 0 & 0 \\ 0 & 0 & 6.67 \times 10^{-5} & 0 & 0 & 0 \\ 0 & 0 & 0 & 2.13 \times 10^{-7} & 0 & 0 \\ 0 & 0 & 0 & 0 & 2.13 \times 10^{-7} & 0 \\ 0 & 0 & 0 & 0 & 0 & 3.2 \times 10^{-7} \end{bmatrix} \begin{bmatrix} F_x \\ F_y \\ F_z \\ M_x \\ M_y \\ M_z \end{bmatrix} \quad (5.51)$$

In the previous sections, displacements and rotations were applied to the peg to calculate the forces and moments acting on the peg. In this section, forces and moments were applied instead, and the displacements and rotations were measured. A summary of the results is shown in Table 5-9 and Table 5-10. The full results are shown in Appendix C.

Table 5-9. Summary of results of comparison when force is applied.

Force (N)	Approximation Matrix						Simscape Model						Error (%)
	dx (mm)	dy (mm)	dz (mm)	Rx (Rad)	Ry (Rad)	Rz (Rad)	dx (mm)	dy (mm)	dz (mm)	Rx (Rad)	Ry (Rad)	Rz (Rad)	
Fx = 10	0.4444	0	0	0	0	0	0.4445	0	0	0	0	0	0.0126
Fx = 50	2.2222	0	0	0	0	0	2.226	0	-0.05	-0.001	0	0	0.1698
Fx = 100	4.4444	0	0	0	0	0	4.472	-0.001	-0.21	-0.005	0	-0.001	0.6162
Fy = 10	0	0.4444	0	0	0	0	0	0.4445	0	0	0	0	0.0126
Fy = 50	0	2.2222	0	0	0	0	0	2.225	-0.05	0.0012	0	0	0.1249
Fy = 100	0	4.4444	0	0	0	0	0	4.467	-0.22	0.0048	0	0	0.5050
Fz = 10	0	0	0.0741	0	0	0	0	0	0.07	0	0	0	5.8729
Fz = 50	0	0	0.3706	0	0	0	0	0	0.37	0	0	0	0.1500
Fz = 100	0	0	0.7411	0	0	0	0	0	0.73	0	0	0	1.5220

Table 5-10. Summary of results of comparison when moment is applied.

Moment (Nmm)	Approximation Matrix						Simscape Model						Error (%)
	dx (mm)	dy (mm)	dz (mm)	Rx (Rad)	Ry (Rad)	Rz (Rad)	dx (mm)	dy (mm)	dz (mm)	Rx (Rad)	Ry (Rad)	Rz (Rad)	
Mx = 100	0	0	0	0.0024	0	0	0	0	0	0.0024	0	0	1.3890
Mx = 500	0	0	0	0.0118	0	0	0	0.0024	0	0.0118	0	0	0.2824
Mx=1000	0	0	0	0.027	0	0	0	0.0101	-0.02	0.0236	0	0	0.2824
My = 100	0	0	0	0	0.0024	0	0	0	0	0	0.0024	0	1.3890
My = 500	0	0	0	0	0.0118	0	0	-0.002	0	0	0.0119	0	0.5603
My=1000	0	0	0	0	0.0237	0	-0.001	-0.009	-0.02	0.0002	0.0238	0	0.5603
Mz = 100	0	0	0	0	0	0.0036	0	0	0	0	0	0.0036	1.2347
Mz = 500	0	0	0	0	0	0.0178	0	0	0	0	0	0.0178	0.1250
Mz=1000	0	0	0	0	0	0.0356	0	0	-0.01	0	0	0.0356	0.1250

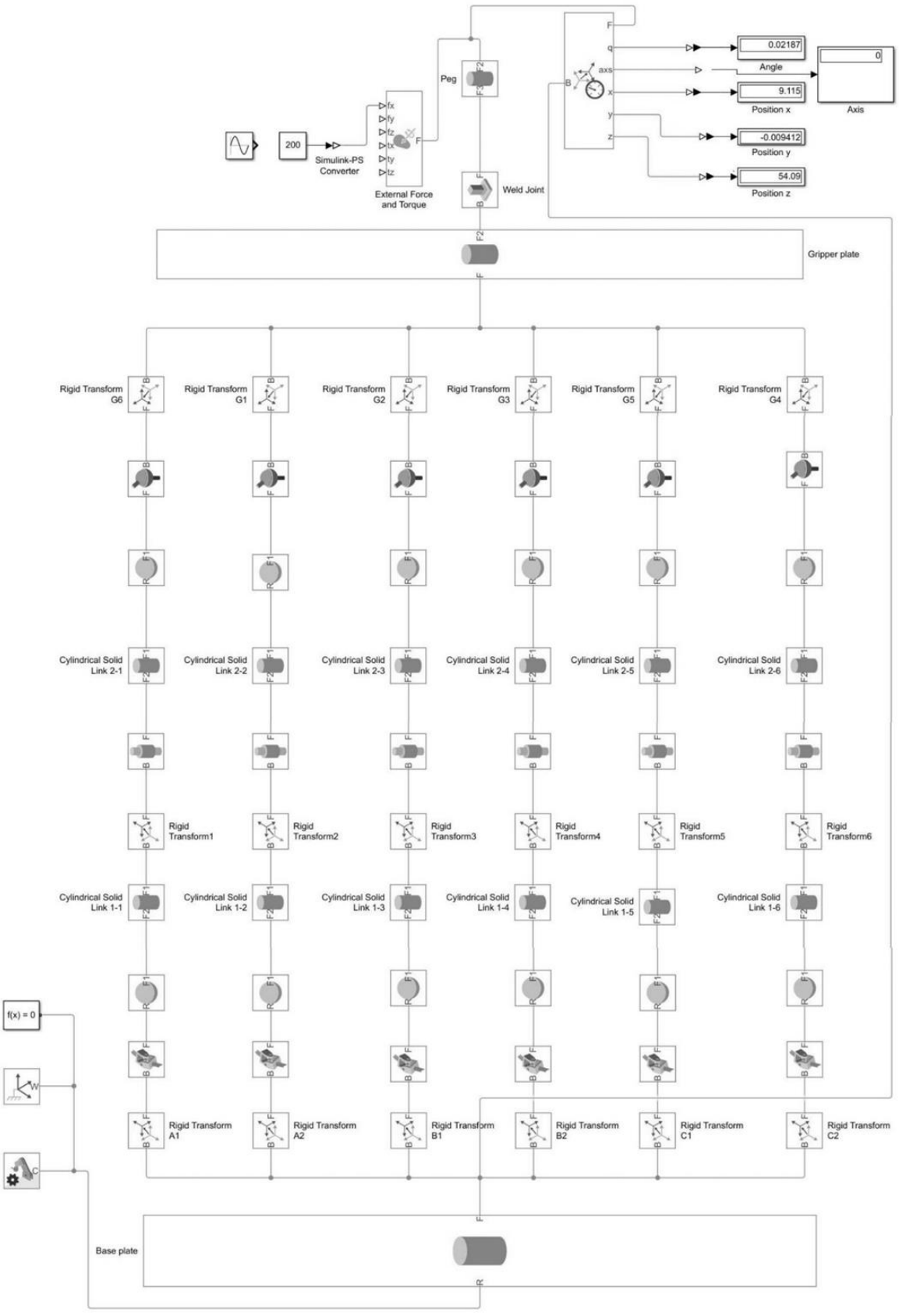

Figure 5-11. Simscape block layout

5.5 Orientation envelope of the peg

The models above only considered the length of the peg but did not consider the diameter of the peg. As mentioned in (McCallion, et al., 1979), a peg with a large diameter is not recommended; however, the permissible peg diameter allowed is unknown. In this section, the orientation of the peg and the effect of the peg radius are analysed to gain a better understanding of the orientation envelope for the movement of the peg.

As shown in Figure 5-12, assuming the vector of the contact point G is known, then the change in contact point G can be calculated.

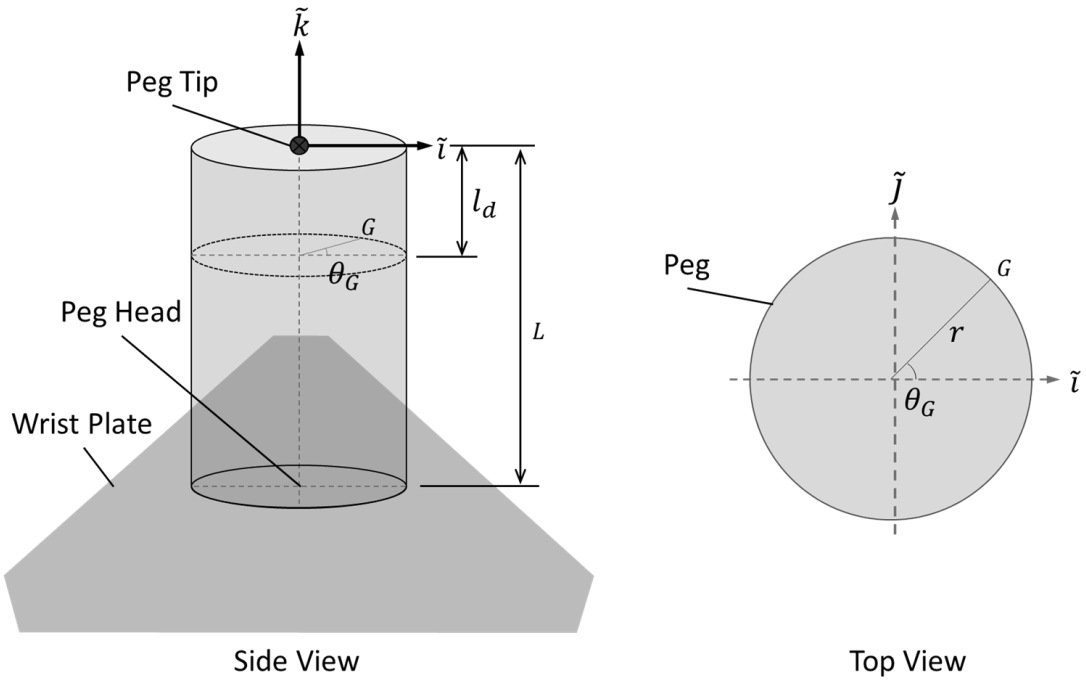

Figure 5-12. Contact point G on the peg

The vector of the Peg Tip, Peg Head and contact point G is shown below:

$$\overrightarrow{PegTip} = \begin{bmatrix} 0 \\ 0 \\ 0 \end{bmatrix} \tag{5.52}$$

$$\overrightarrow{PegHead} = \begin{bmatrix} 0 \\ 0 \\ L \end{bmatrix} \tag{5.53}$$

$$\overrightarrow{OG} = \begin{bmatrix} r\cos\theta_G \\ r\ \sin\theta_G \\ l_d \end{bmatrix} \tag{5.54}$$

where r is the peg radius.

Using the same method in the previous section, substituting Equations (5.52) and (5.53) into Equation (5.34), the new orientation of the peg tip $\overrightarrow{PegTip'}$ and peg head $\overrightarrow{PegHead'}$ is shown below:

$$Peg\ Axis = \overrightarrow{PegHead'} - \overrightarrow{PegTip'} \tag{5.55}$$

The orientation envelope can be calculated easily as well. Substitute Equation (5.54) into Equation (5.34),

$$\begin{aligned}\overrightarrow{\mathrm{OG}'} &= [R_z(\theta_z)] \cdot \left[R_y\left(\theta_y\right)\right] \cdot [R_x(\theta_x)] \cdot \overrightarrow{OG} + [\vec{t}] \\ &= \begin{bmatrix} \cos\theta_y \cos\theta_z & \cos\theta_z \sin\theta_x \sin\theta_y - \cos\theta_x \sin\theta_z & \sin\theta_x \sin\theta_z + \cos\theta_x \cos\theta_z \sin\theta_y \\ \cos\theta_y \sin\theta_z & \cos\theta_x \cos\theta_z + \sin\theta_x \sin\theta_y \sin\theta_z & \cos\theta_x \sin\theta_y \sin\theta_z - \cos\theta_z \sin\theta_x \\ -\sin\theta_z & \cos\theta_y \sin\theta_x & \cos\theta_x \cos\theta_y \end{bmatrix} \begin{bmatrix} r\cos\theta_G \\ r\ \sin\theta_G \\ l_d \end{bmatrix} + \begin{bmatrix} x \\ y \\ z \end{bmatrix}\end{aligned} \quad (5.56)$$

Assuming the translation and rotation are the same in different scenarios, the change in orientation envelope is based on the radius of the peg. Equations (5.59) and (5.61) show the example of comparison.

$$x = 1\ mm$$

$$y, z = 0\ mm$$

$$\theta_x = 0.05\ rad$$

$$\theta_y, \theta_y = 0 \tag{5.57}$$

$$\theta_G = 0$$

$$r = 10\ mm\ Vs\ 15\ mm$$

$$l_d = -10\ mm$$

Using $r = 10\ mm$ substituting Equation (5.57) into (5.56):

$$\overrightarrow{\mathrm{OG'}_{r=10}} = \begin{bmatrix} 11 \\ 0.4998 \\ -9.9875 \end{bmatrix} \tag{5.58}$$

Length of $\overrightarrow{\mathrm{OG'}_{r=10}}$:

$$\left\| \overrightarrow{\mathrm{OG'}_{r=10}} \right\| = \sqrt[2]{11^2 + 0.4998^2 + (-9.9875)^2} = 14.8661\ \mathrm{mm} \tag{5.59}$$

Repeat the calculation for $r = 15\ mm$,

$$\overrightarrow{\mathrm{OG'}_{r=15}} = \begin{bmatrix} 16 \\ 0.4998 \\ -9.9875 \end{bmatrix} \tag{5.60}$$

Length of $\overrightarrow{\mathrm{OG}'_{r=15}}$

$$\left\|\overrightarrow{\mathrm{OG}'_{r=15}}\right\| = \sqrt[2]{15^2 + 0.4998^2 + (-9.9875)^2} = 18.8680 \text{ mm} \quad (5.61)$$

The comparison shows the increase in length between the compliance centre and contact point G. If $\left\|\overrightarrow{\mathrm{OG}'_{r=10}}\right\|$ were to move 18.8680 mm like when the peg is 15 mm, the translation and rotation of the compliance centre have to increase significantly.

This supports the recommendation of avoiding pegs with large diameters. The large peg radius amplifies the rotation at the compliance centre, which will affect the sensitivity and accuracy of the approximation model.

5.6 Summary

This chapter is an extension of (McCallion, et al., 1979). The structure of the device presented by (McCallion, et al., 1979) is altered to make the centre of compliance remote. The wrist plate is lowered, which allows the centre of compliance to be at the tip of the peg. The theoretical model and approximation matrix illustrate the relationship between the translations and rotations of the wrist plate and the reaction forces and moments. The beauty of using the approximation method is that the relationship can be inverted directly without using inverse kinematics. By using only four parameters, the model gives good approximations of stiffnesses for each translation and rotation.

The results of the calculation using the approximation matrix are compared against the numerical validation model, which is representative of the device in real situations. The range of translation and rotation of the compliance centre is 0.1 mm to 1.0 mm and 0.005 radians to 0.05 radians, respectively. Overall, the differences between the results are low. As the translation and rotation decrease, the error decreases significantly. This agrees with the assumption that the approximation matrix is only recommended for small translations and rotations.

Chapter 5.4 shows the comparison between the results of the approximation model and Simscape Simulation. Instead of translating and rotating the peg and calculating the forces and moments acting on the peg, the analysis was done the other way round. The results obtained were still fairly good, and the errors were very low.

The approximation model is tested with pegs with different lengths. Overall, there were some changes in certain forces and moments; however, the errors remained low, and there were no effects on translation and rotation about the Z-axis.

Another advice for using this approximation model is that the diameter of the peg should not be too large. This is illustrated in Chapter 5.5; with a large diameter, the translation and rotation will be amplified at the compliance centre when the peg is in contact with the hole.

Chapter 6

Conclusion

This research has shown the phenomenon of peg-hole wedging in detail, the tactics to dislodge the wedged peg and the design of a compliant device to avoid wedging. To understand previous research in manufacturing and remanufacturing, the first part of this thesis presents an overview of peg-hole assembly and disassembly mechanics and strategies. The review showed that many researchers have proposed ways to overcome peg-hole jamming; however, they often only mentioned the definition and conditions for peg-hole wedging to happen and ways to avoid it. There are differences between jamming and wedging. Jamming occurs when the force is applied in an incorrect direction, and it can be rectified easily by redirecting the force. The wedging of a peg occurs when the peg is stuck in the hole and reaction forces on the contact points are collinear.

In this thesis, the wedging of a peg in a hole has been investigated in detail. Using the definition and necessary conditions for wedging to occur, the process of wedging is established. The wedging process consists of four steps. First, the peg and hole must be in 2-point contact, and the two contact points must be within each other's friction cone. Then, a force or moment is applied to increase the peg tilting angle and deform the peg and hole. The third step is to release the force or moment applied, and the peg tilting angle will be reduced by a small amount. Once the peg tilting angle reduces, the reaction forces at the contact points

will be collinear, and the peg is wedged. The wedging process is shown in the simulations and proven in experiments, and the results agree with the hypothesis. The results showed that the difference between the resultant forces on both sides of the hole is almost zero. Thus, objective 1 has been achieved.

The dislodging of a wedged peg is analysed in this thesis as well. When an object such as an old wooden drawer is stuck, the intuitive way to dislodge it is by shaking or using impact. Due to the small clearance between the peg and the hole, an upwards or vertical force is applied to dislodge the peg. Subjected to the requirements of the disassembly process, some would prioritise the maintenance of the quality of the components, and some would require a short disassembly process time. Due to the contact state of the wedged peg, i.e., 2-point contact, the variables used in the analysis are critical; therefore, the investigation is carried out using simulation. The peg is systematically wedged using the method discussed in Chapter 3 before dislodging it using different tactics of pulling. To investigate the parameters that produce the low impulses, the wedged peg is pulled using different methods: by a continuous force and with pulses of different frequencies (10 Hz to 50 Hz). The process of dislodging is repeated with different magnitudes of forces. Due to the nature of the simulation, the data have a step change across the magnitude as it depends on the time step setting. The simulation results show that within a specific range of pulling force magnitudes, the peg is dislodged at low impulses. In the low magnitude region, pulsating force helps reduce the impulse required to dislodge the peg compared to using continuous force. On the other hand, using continuous force in the lowest magnitude region resulted in lower impulse as the duration of dislodging the peg was shorter compared to using pulsating force. The

relationships between different parameters are illustrated; hence, objectives 2 and 3 have been accomplished.

The compliance device from (McCallion, et al., 1979) has been redesigned to make the centre of compliance remote by lowering the wrist plate. The principle of the design is based on the Gough-Whitehall-Stewart Platform mechanism. The RCC devices currently available can only withstand high compressive forces; thus, they are not appropriate for disassembly. The proposed design in this thesis can resist both compressive and tensile forces, which suits the purpose of both assembly and disassembly operations. Using a small approximation, a theoretical model has been derived, and its correctness has been shown through numerical analysis and simulations. The model is able to simplify the stiffness of the device into a diagonal matrix, which enables the translational and rotational stiffnesses to be calculated easily. Several assumptions were made when deriving the model: all joints are frictionless, the links between the platform do not bend, the stiffness of the springs in the links are constant, and the device is only suitable for small translations and rotations. The errors between the model and the sensitivity analysis were low; however, they increased as the translation and rotation increased. The simulation also demonstrated that the model is reversible, whereby forces and moments are the inputs to calculate the translations and rotations and vice versa. Therefore, objectives 4, 5 and 6 have been attained.

6.1 Contributions

The key contributions of this work include the following:

- Defining and standardising a systematic approach for wedging a peg in a hole. The process of peg-hole wedging was proposed based on the definition of wedging by (Simunovic, 1979). Several different assumptions and scenarios were analysed before reaching the correct method mentioned in this study.
- Demonstrating and illustrating the process of peg-hole wedging. This is carried out by finite element simulation and experiment.
- Offering opportunities for other researchers to repeat the process to further investigate the dislodging of a wedged peg.
- Analysing the duration of dislodging a wedged peg using different methods and magnitudes of pulling force.
- Demonstrating the effectiveness of using pulsating forces to dislodge a wedged peg.
- Designing an RCC device for peg hole assembly and disassembly. The design is based on the Gough-Whitehall-Stewart mechanism. (McCallion, et al., 1979) built a compliant device based on this mechanism; however, the centre of compliance was not remote.
- Deriving a simplified model of the new RCC device. Using small movement approximations, the stiffnesses of the device can be obtained easily by only using four parameters. Using simulation, it is shown that the approximation model is able to calculate the forces and moments using translations and moments and vice versa.

6.2 Future Work

The process of wedging a peg in a hole has been defined and proven; however, this applies to all scenarios. To be more specific, the wedging of a peg can be modelled and quantified using the peg-hole geometry and material properties, and then the degree of wedging can be estimated. The degree of wedging should indicate the seriousness of the wedging of the peg, and this would be used as a guide in regard to dislodging the peg. In the future, this analysis could be conducted in 3 dimensions and only using one hole instead of separating it as in this work to confirm the definition and necessary conditions of peg-hole wedging.

The dislodging of a wedged peg is studied in 2 dimensions in this research, and the peg was dislodged by applying an upwards force with different frequencies of pulses. Based on human intuition, when a peg is stuck in a hole, one would shake and twist the peg and often it could be dislodged easily. As an extension of this investigation, this problem could be analysed as a 3-dimensional problem and to study other methods of dislodging the peg, such as shaking, twisting and vibration. Then, a comparison would be made to justify the best way of dislodging a peg that is stuck in a hole. Furthermore, optimisation algorithms, such as the Bees Algorithm, could be integrated to obtain the optimal combination of parameters to dislodge a wedged peg.

The RCC device in this research, based on the Gough-Whitehall-Stewart mechanism, has only been tested and analysed numerically and through simulations. This RCC device can be constructed to experimentally validate the approximation model. In addition, the design of the device could be made flexible, where users are able to alter the device to be used for pegs of different lengths. This could be achieved by either making the angle of the links or the size

of the base plate variable. Instead of using springs to make the RCC device active, the links could be pneumatically controlled to change the stiffnesses of the links, and this design can be used for assembly and disassembly.

References

Amezquita, T., Hammond, R., Salazarand, M. & Bras, B., 1995. *Characterizing the Remanufacturability of Engineering.* Massachusetts, ASME.

Baksys, B., Baskutiene, J. & Baskutis, S., 2017. The vibratory alignment of the parts in robotic assembly. *Industrial Robot: An International Journal,* 44(6), pp. 720-729.

Bakšys, B., Baskutienė, J. & Vėžys, J., 2014. Experimental research of vibratory alignment using passive compliance devices. *Mechanika,* 20(2), pp. 165-170.

Bakšys, B., Baskutien, J., Kilikevičius, S. & Chadarovičius, A., 2010. Experimental analysis of the robotized assembly applying vibrations. *Journalof Vibroengineering,* 12(4), pp. 572-581.

Bakšys, B., Kilikevičius, S. & Chadarovičius, A., 2011. Experimental investigation of vibratory assembly with passive compliance. *Mechanika,* 17(6), pp. 608-614.

Bakšys, B. & Mikolainis, J., 2011. Experimental research of vibratory slipping of the shaft fastened with tightness in the bushing. *Mechanika,* 17(5), pp. 492-497.

Begey, J., Vedrines, M. & Renaud, P., 2020. Design of Tensegrity-Based Manipulators: Comparison of Two Approaches to Respect a Remote Center of Motion Constraint. *IEEE Robotics and Automation Letters,* 5(2), pp. 1788-1795.

Bottero, S., Muscolo, G. G. & Ferraresi, C., 2020. A New Soft RCC Device with Pneumatic Regulation. *MDPI Robotics,* 9(98).

British Standard Institute , 2010. *BS 8887-220:2010 Design for Manufacture, Assembly, Disassembly and End-of-Life Processing (MADE),* London: BSI.

Chen, H. et al., 2009. High-precision assembly automation based on robot compliance. *International Journal of Advance Manufacturing Technology,* pp. 999-1006.

Choi, S., Lee, S. & Won, S., 2001. *Development of a New Variable Remote Center Compliance using Stiffness Adjusters.* Hawaii, Proceedings of the 2001 IEEE/RSJ.

Ciblak, N. & Lipkin, H., 2003. Design and Analysis of Remote Center of Compliance Structures. *Journal of Robotic Systems,* 20(8), pp. 415-427.

Colledani, M., Copani, G. & Tolio, T., 2014. *De-Manufacturing Systems.* Windsor, Canada, Elsevier Procedia.

Dieudonné, E. et al., 2020. A study on the experimental investigation of low frequency vibration wave assisted disassembly of press-fit joints. *Journal of Manufacturing Processes,* Volume 49, pp. 70-81.

Drake, S. H., 1977. *Using Compliance In Lieu Of Sensory Feedback For Automatic Assembly,* Massachusetts, USA: Massachusetts Institute of Technology.

Fichter, E. F., Kerr, D. R. & Rees-Jones, J., 2008. The Gough–Stewart platform parallel manipulator:. *Journal of Mechanical Engineering Science,* Volume 223, pp. 243-281.

Fritz, L. J. & Koster, W. P., 1977. *Tensile and Creep Rupture Properties of (16) Uncoated and (2) Coated Engineering Alloys at Elevated Temperatures.* s.l.:s.n.

Gallardo-Alvarado, J. & Garcı´a-Murillo, M., 2012. A parallel manipulator inspired by the original Stewart platform. *Institution of Mechanical Engineering,* 227(4), pp. 831-844.

Gough, V. E. & Whitehall, S. G., 1962. *Universal Tyre Test Machine.* London, UK, Institution of Mechanical Engineering.

Haskiya, W., Maycock, K. & Knight, J., 1999. Robotic assembly: Chamferless peg-hole assembly. *Robotica,* Volume 17, pp. 621-634.

Hibbeler, R. C. & Yap, K. B., 2013. Kinetics of a Particle: Impulse and Momentum. In: M. Cohen, A. Deb, D. Villamero & K. Yap, eds. *Mechanics for Engineerings: Dynamics.* Jurong, Singapore: Pearson Education South Asia Pte Ltd, pp. 221-310.

Hollins, O., 2020. *European Remanufacturing Council.* [Online] Available at: https://www.remanufacturing.eu/about-remanufacturing.php [Accessed 2022].

Horvath, B., 2018. The recognition of resource use through industrial development from a social perspective.. *Studia Mundi - Economica,* 5(1), pp. 68-78.

iED Team, 2019. *Institute of Entrepreneurship Development.* [Online] Available at: https://ied.eu/project-updates/the-4-industrial-revolutions/ [Accessed 19 02 2020].

Ijomah, W. L., Childe, S. & McMahon, C., 2004. Remanufacturing: A Key Strategy for Sustainable.

Jeong, K. W. & Cho, H. S., 1989. Development of a pneumatic vibratory wrist for robotic assembly. *Robotica,* Volume 7, pp. 9-16.

Jin, S., Zhu, X., Wang, C. & Tomizuka, M., 2021. Contact Pose Identification for Peg-in-Hole Assembly under Uncertainties. *Cornell University .*

Joo, S., Waki, H. & Miyazaki, F., 1996. *On the Mechanics of Elastomer Shear Pads for Remote Center Compliance (RCC).* Minnesota, Proceedings of the 1996 IEEE International Conference on Robotics and Automation.

Kang, E. & Cho, H., 1995. Vibratory assembly of prismatic parts using neural network-based positioning error estimation. *Robotica,* Volume 13, pp. 185-193.

Katz, Z. & Wyk, R. S. J. v., 1997. Analysis of Peg-Hole Automated Pre-assembly Engagement Search. *The International Journal of Advanced Manufacturing Technology,* Volume 13, pp. 426-433.

Kerin, M. & Pham, D. T., 2019. A review of emerging industry 4.0 technologies in remanufacturing. *Journal of Cleaner Production.*

Kerin, M. & Pham, D. T., 2020. Smart remanufacturing: a review. *Emerald,* 31(6), pp. 1205-1235.

Kilikevicius, S. & Baksys, B., 2011. Dynamic analysis of vibratory insertion process. *Emerald,* 31(3), pp. 275-283.

Kim, U. et al., 2021. Displacement Sensor Integrated Into a Remote Center Compliance Device for a Robotic Assembly. *IEEE Access,* Volume 9, pp. 43192-43201.

Lai, L.-J., Gu, G.-Y., Zhou, H. & Zhu, L.-M., 2013. Design and Analysis of a Spatial Remote Center of Compliance Mechanism. *Springer-Verlag Berlin Heidelberg,* pp. 385-396.

Laili, Y. et al., 2019. Robotic disassembly re-planning using a two-pointer detection strategy and a super-fast bees algorithm.. *Robotics and Computer Integrated Manufacturing,* pp. 130-142.

Lai, L.-J. & Zhu, Z.-N., 2016. Modeling and Analysis of a Compliance Model and Rotational Precision for a Class of Remote Center Compliance Mechanisms. *Applied Science,* 6(388).

Lee, S., 2005. Development of a New Variable Remote Center Compliance (VRCC) With Modified Elastomer Shear Pad (ESP) for Robot Assembly. *IEEE Transactions on Automation Science and Engineering,* 2(2), pp. 193-197.

Lee, S., 2009. Shear Control of Elastomer Shear Pads for Variable Remote Center Compliance. *Advanced Robotics ,* 23(1-2), pp. 227-237.

Lee, S., Won, S. & Choi, S., 2000. Development of a new variable remote center compliance for assembly robots. *Advanced Robotics,* 14(3), pp. 241-255.

Liao, H.-T. & Leu, M. C., 1998. Analysis of Impact in Robotic Peg-in-Hole Assembly. *Robotica,* Volume 16, p. 347–356.

Li, R. et al., 2020. Unfastening of Hexagonal Headed Screws by a Collaborative Robot. *IEEE Transaction on Automation Science and Engineering,* 17(3), pp. 1455-1468.

Liu, Y. & Wang, M. Y., 2014. Optimal Design of Remote Center Compliance Devices of Rotational Symmetry. *IFIP International Federation for Information Processing ,* pp. 161-169.

Liu, Z. et al., 2019. Screw Insertion Method in Peg-in-Hole Assembly for Axial Friction Reduction. *IEEE,* Volume 7, pp. 148313-148325.

McCallion, H., Johnson, G. R. & Pham, D. T., 1979. A Compliant Device For Inserting A Peg In A Hole. *Industrial Robot: An International Journal,* 6(2), pp. 81-87.

Mullo, S. D., Pruna, E., Wolff, J. & Raatz, A., 2018. *A vibration control for disassembly of turbine blades.* Gulf of Naples, Italy, Elsevier B. V..

Oh, S.-R., Hollis, R. L. & Salcudean, S. E., 1993. Precision Assembly with a Magnetically Levitated Wrist. *IEEE,* pp. 127-134.

Park, D. I. et al., 2018. Passive compliant module with the displacement measurement sensor and its application for automatic assembly. *International Federation of Automatic Control,* pp. 85-90.

Park, D. I. et al., 2017. *Variable Passive Compliance Device For Robotic Assembly.* Korea, 14th International Conference on Ubiquitous Robots and Ambient Intelligence (URAI).

Pham, D. T., 1985. *Improvements in compliant devices.* London, England, Patent No. GB2152473.

Pitchandi, N., Subramanian, S. P. & Irulappan, M., 2017. Insertion force analysis of compliantly supported peg-in-hole assembly. *Assembly Automation,* 37(3), pp. 285-295.

Sadauskas, E. & Baksys, B., 2014. Peg-bush alignment under elastic vibrations. *Emerald,* 34(4), pp. 349-356.

Sadauskas, E., Bakšys, B. & Jurėnas, V., 2013. Elastic vibrations of the peg during part alignment. *Mechanika,* 19(6), pp. 676-680.

Simunovic, S., 1979. *An Information Approach To Parts Mating,* Massachusetts, USA: Massachusetts Institute of Technology.

Stewart, D., 1965. *A Platform with Six Degree of Freedom.* London, The Industrial Robot, pp. 371-386.

Su, H. et al., 2020. Improved recurrent neural network-based manipulator control with remote center of motion constraints: Experimental results. *Neural Networks,* pp. 291-299.

Su, J., Hong, Q., Ou, Z. & Zhang, Y., 2012. Sensor-less insertion strategy for an eccentric peg in a hole of the crankshaft and bearing assembly. *Emerald Group Publishing Limited,* pp. 86-99.

Tang, T. et al., 2016. *Autonomous Alignment of Peg and Hole by Force/Torque Measurement for Robotic Assembly.* Fort Worth, Texas, IEEE International Conference on Automation Science and Engineering (CASE).

Vartanov, M. & Martynovich, N., 2016. *Reliability for the Robotic Assembly of Cylindrical Parts.* s.l., Elsevier Ltd..

Vartanov, M. V., Petukhov, S. L. & Trung Ta, T., 2020. Experimental Research of the Robotic Assembly Process Using the Effect of Rotation and Low-Frequency Vibration. *IEEE.*

Wang, P. et al., 2015. *Robotic Assembly System Guided by Multiple Vision and Laser Sensors for Large Scale Components.* Zhuhai, China, IEEE Conference on Robotics and Biomimetics.

Wang, S., Chen, G., Xu, H. & Wang, Z., 2019. A Robotic Peg-in-Hole Assembly Strategy Based on Variable Compliance Center. *IEEE Access,* pp. 167534-167546.

Wang, Y. et al., 2020. Interlocking problems in disassembly sequence planning. *International Journal of Production Research.*

Wang, Y. et al., 2018. *Contact Force/Torque Prediction and Analysis Model Large Length-diameter Ratio Peg-in-hole Assembly.* Kuala Lumpur, Malaysia, IEEE International Conference on Robotics and Biomimetics.

Weigl, A. & Seitz, M., 1994. *Vission Assisted Disassembly Using A Dexterous Hand-Arm-System: An Example And Experimental Results.* Capri, Italy, Fourth IFAC Symposium on Robot Control.

Whitney, D. E., 1982. Quasi-Static Assembly Of Compliantly Supported Rigid Parts. *Journal Of Dynamic Systems, Measurement, And Control,* Volume 104, pp. 65-77.

Wohlert-Jensen, C. H. H., 1978. *Techniques for Automatic Assembly.* Christchurch, New Zealand: University of Canterbury.

Wohlert-Jensen, K., 1978. *Techniques for Auntomatic Assembly,* Christchurch, New Zealand: University of Canterbury.

Wolff, J., Kolditz, T., Fei, Y. & Raatz, A., 2018. *Simulation-Based Determination of Disassembly Forces.* s.l., Elsevier B. V., pp. 13-18.

Wolff, J., Yan, M., Schultz, M. & Raatz, A., 2016. *Reduction of Disassembly Forces for Detaching Components with Solidified Assembly Connections.* Garbsen, Germany, Published by.

Yoshida, T. et al., 2001. Disassembly System using an Impact Hammer for the Material Recycling. *Memoirs of the Faculty of Engineering, Okayama University,* 35(1&2), pp. 191-196.

Zhang, K. et al., 2019. Jamming Analysis and Force Control for Flexible Dual Peg-in-Hole Assembly. *IEEE Transactions on Industrial Electronics,* 66(3), pp. 1930-1939.

Zhang, Y. et al., 2019. Peg–hole disassembly using active compliance. *Royal Society Open Science,* Volume 6.

Zhang, Z. et al., 2020. A Stiffness Variable Passive Compliance Device with Reconfigurable Elastic Inner Skeleton and Origami Shell. *Chinese Journal of Mechanical Engineering.*

Zhao, F. & Wu, P. S. Y., 1998. VRCC: A Variable Remote Centre Complaince Device. *Mechatronics ,* Volume 8, pp. 657-672.

Zhao, Y., Chen, K., Yu, J. & Huang, S., 2021. Design of a parallel compliance device with variable stiffness. *Journal of Mechanical Engineering Science ,* 235(1), pp. 94-107.

Zhao, Y., Gao, F., Zhao, Y. & Chen, Z., 2020. Peg-in-Hole Assembly Based on Six-Legged Robots. *MDPI,* 20(10), p. 2861.

Appendix

Appendix A: Wedging of a Peg.

Due to the small meshes of Hole-A and Hole-B, it is difficult to show the high stresses of the hole in the simulation. Thus, Figure A - 1 and Figure A - 2 are examples of the peg wedging simulations, whereby Figure A - 1 shows a successful wedge and Figure A - 2 shows an unsuccessful wedge.

Table A - 1. Material property of the peg and hole.

	Peg			Hole		
Mass Density	8.05 e-9			8.05 e-9		
Young's Modulus	5000000			193000		
Poisson's Ratio	0.27			0.27		
Plasticity		**Yield Stress**	**Plastic Strain**		**Yield Stress**	**Plastic Strain**
	1	5000	0	**1**	210	0
	2	5000	1	**2**	290	1

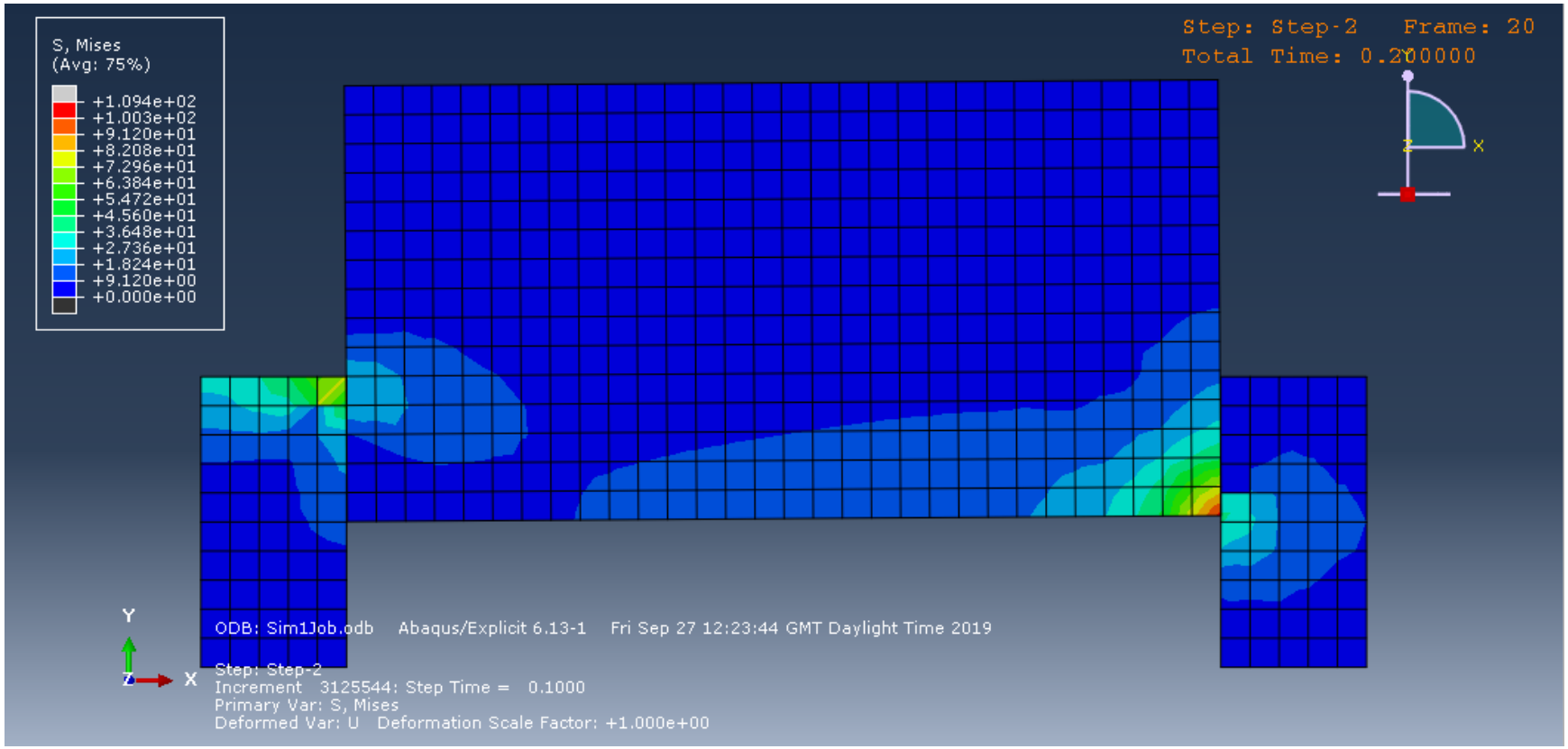

Figure A - 1. Wedging simulation example: A successful wedge when the insertion depth is within the limit

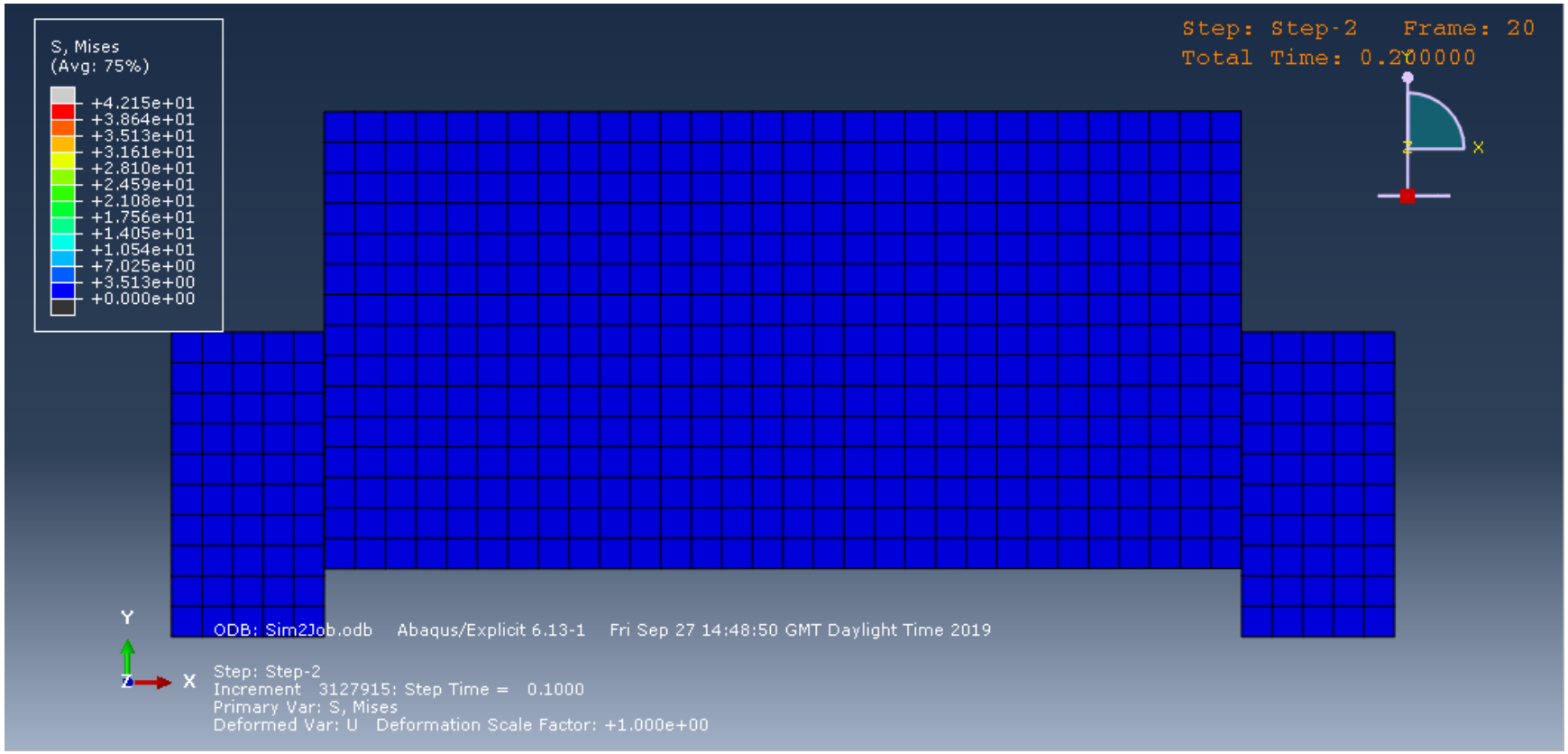

Figure A - 2. Wedging simulation example: An unsuccessful wedge when the insertion depth exits the limit

Table A - 2. Wedging Experiment - A: Results.

Region	Time	Left Fx	Right Fx	Left Fy	Right Fy	Left Fz	Right Fz	Left Resultant Force	Right Resultant Force	Ave Reaction Force	Diff. Reaction Force	Error %
1	0	-3.0629	1.7	-0.3087	0	-0.4008	-0.2	3.1043	1.7117	2.4080	1.3926	57.83
1	0.1	-2.3820	1.3	-0.3359	0	-0.5331	-0.1	2.4639	1.3038	1.8839	1.1601	61.58
1	0.2	-2.4371	1.2	-0.5941	0	-0.2863	-0.2	2.5248	1.2166	1.8707	1.3082	69.93
1	0.3	-1.9293	0.8	-0.4366	0	-0.3131	-0.2	2.0027	0.8246	1.4136	1.1780	83.33
1	0.4	-1.6659	0.6	-0.3869	0	-0.1693	-0.1	1.7186	0.6083	1.1635	1.1104	95.44
1	0.5	-1.6609	0.5	-0.5449	0	-0.2842	-0.1	1.7710	0.5099	1.1404	1.2611	110.58
1	0.6	-2.0787	0.5	-0.4726	0	0.1684	0	2.1384	0.5000	1.3192	1.6384	124.20
1	0.7	-2.0326	0.5	-0.3835	0	0.4032	0	2.1074	0.5000	1.3037	1.6074	123.30
1	0.8	-2.2405	0.5	-0.3647	0	0.3738	0	2.3006	0.5000	1.4003	1.8006	128.59
1	0.9	-2.4692	0.4	-0.3903	0	0.5804	0.1	2.5664	0.4123	1.4893	2.1541	144.63
1	1	-2.8575	0.3	-0.5342	0	0.1590	0	2.9114	0.3000	1.6057	2.6114	162.63
1	1.1	-3.0388	0.3	-0.4287	0	0.3675	0	3.0908	0.3000	1.6954	2.7908	164.61
1	1.2	-5.3532	1.5	-0.6568	0.1	-0.3475	0.3	5.4045	1.5330	3.4687	3.8715	111.61
2	1.3	-9.6397	4.2	-1.2246	0.3	-1.6115	1	9.8499	4.3278	7.0889	5.5221	77.90
2	1.4	-19.2992	9.5	-2.8880	0.9	-3.4364	2.1	19.8143	9.7709	14.7926	10.0435	67.90
2	1.5	-27.1513	14.6	-4.8088	1.6	-4.9072	3	28.0071	14.9907	21.4989	13.0164	60.54
2	1.6	-30.4666	18.2	-5.0892	2	-5.6976	3.6	31.4098	18.6601	25.0350	12.7497	50.93

2	1.7	-31.0160	20.5	-4.6789	2.1	-6.0274	4.2	31.9407	21.0309	26.4858	10.9098	41.19
2	1.8	-31.9480	22.7	-3.6630	1.9	-7.2319	4.9	32.9604	23.3004	28.1304	9.6600	34.34
2	1.9	-36.5541	26.2	-4.1455	1.9	-8.7463	6	37.8138	26.9453	32.3795	10.8685	33.57
2	2	-42.1146	29.9	-4.9134	2.1	-10.0186	7	43.5678	30.7802	37.1740	12.7876	34.40
2	2.1	-45.8223	33.4	-6.0547	2.3	-10.9496	8.1	47.4999	34.4450	40.9724	13.0548	31.86
2	2.2	-48.5913	36.4	-5.7327	2.2	-11.8581	9	50.3448	37.5606	43.9527	12.7842	29.09
2	2.3	-50.3203	38.6	-5.6743	2.1	-12.5407	9.7	52.1689	39.8555	46.0122	12.3134	26.76
2	2.4	-50.8365	40.2	-5.4322	2	-13.2827	10.2	52.8232	41.5220	47.1726	11.3011	23.96
2	2.5	-52.2942	42	-5.5537	1.9	-14.1361	10.9	54.4551	43.4329	48.9440	11.0221	22.52
2	2.6	-54.4040	43.8	-5.5957	1.9	-15.0126	11.5	56.7140	45.3244	51.0192	11.3897	22.32
2	2.7	-55.2680	45	-5.9430	1.9	-15.0825	11.9	57.5964	46.5856	52.0910	11.0108	21.14
2	2.8	-55.8566	46.1	-5.9563	1.9	-15.4351	12.4	58.2553	47.7764	53.0158	10.4790	19.77
2	2.9	-57.1419	47.2	-6.1632	1.9	-15.6792	12.7	59.5736	48.9156	54.2446	10.6580	19.65
2	3	-57.2771	48	-6.1403	2	-15.7259	13	59.7133	49.7695	54.7414	9.9438	18.17
2	3.1	-57.6025	48.5	-6.2614	2	-16.0354	13.2	60.1198	50.3040	55.2119	9.8158	17.78
2	3.2	-57.5164	48.8	-6.3964	2.2	-16.3587	13.5	60.1386	50.6807	55.4096	9.4580	17.07
2	3.3	-57.9487	49.1	-6.7192	2.5	-17.2091	13.7	60.8223	51.0368	55.9295	9.7856	17.50
2	3.4	-58.0198	49.5	-7.0740	2.8	-17.2211	13.8	60.9336	51.4639	56.1987	9.4697	16.85
2	3.5	-58.4851	49.7	-7.6540	3	-16.7823	13.8	61.3248	51.6675	56.4962	9.6573	17.09
2	3.6	-58.5382	49.9	-7.7440	3.2	-16.8064	13.7	61.3934	51.8453	56.6194	9.5481	16.86
2	3.7	-58.4542	50.1	-7.5610	3.3	-16.6552	13.6	61.2491	52.0179	56.6335	9.2312	16.30

2	3.8	-58.4582	50.2	-7.6783	3.3	-16.4628	13.6	61.2156	52.1142	56.6649	9.1014	16.06
2	3.9	-58.5064	50.2	-7.8305	3.4	-16.3171	13.5	61.2418	52.0946	56.6682	9.1472	16.14
2	4	-58.4486	50.3	-7.8149	3.4	-15.9319	13.4	61.0830	52.1652	56.6241	8.9178	15.75
2	4.1	-58.3978	50.4	-7.6715	3.4	-15.4672	13.2	60.8966	52.2107	56.5537	8.6859	15.36
2	4.2	-58.4390	50.5	-7.5319	3.5	-15.3180	12.9	60.8809	52.2390	56.5599	8.6419	15.28
2	4.3	-58.4140	50.7	-7.5716	3.5	-14.7469	12.6	60.7206	52.3593	56.5400	8.3613	14.79
2	4.4	-58.6643	50.8	-7.5820	3.5	-14.2335	12.2	60.8406	52.3615	56.6011	8.4791	14.98
2	4.5	-58.5616	51	-7.6496	3.5	-13.8274	11.9	60.6562	52.4868	56.5715	8.1694	14.44
2	4.6	-58.6317	51.1	-7.6898	3.5	-13.3571	11.6	60.6236	52.5169	56.5702	8.1067	14.33
2	4.7	-58.7979	51.2	-7.7541	3.6	-13.1410	11.3	60.7454	52.5556	56.6505	8.1898	14.46
2	4.8	-58.7626	51.3	-7.6176	3.6	-12.9808	11.1	60.6594	52.6105	56.6349	8.0490	14.21
2	4.9	-58.8376	51.5	-7.7470	3.6	-12.4779	10.6	60.6430	52.7027	56.6728	7.9403	14.01
3	5	-59.0624	51.9	-7.8472	3.6	-11.1888	9.6	60.6229	52.9030	56.7629	7.7198	13.60
3	5.1	-59.4556	52.7	-8.0582	3.7	-9.3679	7.7	60.7261	53.3879	57.0570	7.3382	12.86
3	5.2	-59.9064	54.1	-8.0782	3.7	-5.5508	4.3	60.7029	54.3966	57.5498	6.3063	10.96
3	5.3	-60.8974	55.7	-8.2689	3.7	-1.3880	0.1	61.4719	55.8228	58.6474	5.6491	9.63
3	5.4	-60.8785	57	-7.3607	3.7	-0.4113	-3	61.3233	57.1987	59.2610	4.1246	6.96
3	5.5	-60.3321	57.8	-6.8716	3.6	-0.6696	-5	60.7258	58.1274	59.4266	2.5984	4.37
3	5.6	-60.2870	58.3	-6.7053	3.6	-0.7737	-6.2	60.6637	58.7392	59.7014	1.9245	3.22
4	5.7	-60.2363	58.6	-6.6796	3.6	-0.7215	-6.9	60.6099	59.1145	59.8622	1.4953	2.50
4	5.8	-60.1500	58.8	-6.7665	3.6	-0.9027	-7.3	60.5361	59.3607	59.9484	1.1755	1.96

4	5.9	-60.1469	58.9	-6.7408	3.5	-1.0044	-7.6	60.5317	59.4913	60.0115	1.0404	1.73
4	6	-60.1410	59	-6.6955	3.5	-1.0702	-7.8	60.5221	59.6162	60.0691	0.9059	1.51
4	6.1	-60.2233	59	-6.6850	3.5	-0.8535	-7.9	60.5992	59.6294	60.1143	0.9699	1.61
4	6.2	-60.1080	59.1	-6.6828	3.5	-1.0522	-8	60.4875	59.7416	60.1146	0.7459	1.24
4	6.3	-60.1350	59.1	-6.6507	3.5	-0.9030	-8.1	60.5084	59.7551	60.1318	0.7533	1.25
4	6.4	-60.0803	59.1	-6.7051	3.5	-0.9590	-8.2	60.4609	59.7687	60.1148	0.6922	1.15
4	6.5	-60.0896	59.1	-6.6873	3.5	-0.8335	-8.2	60.4663	59.7687	60.1175	0.6975	1.16
4	6.6	-60.1041	59.1	-6.6715	3.5	-1.0295	-8.2	60.4820	59.7687	60.1253	0.7132	1.19
4	6.7	-60.0822	59.2	-6.6565	3.5	-0.9274	-8.2	60.4569	59.8676	60.1623	0.5893	0.98
4	6.8	-60.0683	59.2	-6.6588	3.5	-1.0238	-8.2	60.4449	59.8676	60.1562	0.5773	0.96
4	6.9	-60.0356	59.2	-6.6589	3.5	-0.9022	-8.2	60.4105	59.8676	60.1390	0.5429	0.90
4	7	-60.0438	59.2	-6.6773	3.5	-0.8046	-8.2	60.4193	59.8676	60.1435	0.5517	0.92

Table A - 3. Wedging Experiment - B: Results.

Region	Time	Left Fx	Right Fx	Left Fy	Right Fy	Left Fz	Right Fz	Left Resultant Force	Right Resultant Force	Ave Reaction Force	Diff. Reaction Force	Error %
1	0	-2.1800	0.1	-0.6183	0	-0.1754	0.1	2.2727	0.1414	1.2071	2.1313	176.57
1	0.1	-2.3760	0.1	-0.6930	0	-0.2715	0.1	2.4899	0.1414	1.3156	2.3484	178.50
1	0.2	-2.7105	0.2	-0.7029	0	-0.4175	0.1	2.8311	0.2236	1.5274	2.6075	170.72
1	0.3	-2.6637	0.2	-0.5729	0	-0.4503	0.1	2.7615	0.2236	1.4926	2.5379	170.04
1	0.4	-2.5187	0.2	-0.6381	0	-0.4588	0.2	2.6384	0.2828	1.4606	2.3556	161.27
1	0.5	-2.7221	0.1	-0.6177	0	-0.6376	0.1	2.8632	0.1414	1.5023	2.7218	181.17
1	0.6	-2.6132	0.1	-0.5727	0	-0.1948	0.1	2.6823	0.1414	1.4119	2.5409	179.97
1	0.7	-2.5996	0	-0.5836	0	-0.2820	0.1	2.6792	0.1000	1.3896	2.5792	185.61
1	0.8	-2.7479	0	-0.6130	0	-0.0658	0.1	2.8162	0.1000	1.4581	2.7162	186.28
1	0.9	-2.9651	0	-0.7717	0	-0.3114	0.1	3.0797	0.1000	1.5899	2.9797	187.42
1	1	-3.4672	0	-0.6333	0	-0.0462	0.1	3.5249	0.1000	1.8124	3.4249	188.97
1	1.1	-4.0257	0.2	-0.7486	0	0.0593	0.1	4.0951	0.2236	2.1594	3.8715	179.29
1	1.2	-4.0057	0.2	-0.9649	0	0.1027	0.1	4.1216	0.2236	2.1726	3.8980	179.42
1	1.3	-4.1254	0.2	-1.1176	-0.2	-0.2410	0.2	4.2809	0.3464	2.3137	3.9345	170.06
1	1.4	-4.1287	0.2	-1.0241	-0.3	-0.2987	0.5	4.2643	0.6164	2.4404	3.6479	149.48
1	1.5	-4.1238	0.2	-0.9161	0.1	-0.5726	0.4	4.2629	0.4583	2.3606	3.8047	161.17
1	1.6	-4.1573	0.2	-1.8674	0.4	-0.6781	0.5	4.6076	0.6708	2.6392	3.9368	149.17

1	1.7	-4.1387	0.3	-3.5050	0.6	-0.8014	0.7	5.4824	0.9695	3.2259	4.5128	139.89
1	1.8	-4.1230	0.3	-4.2296	0.7	-0.8531	0.9	5.9679	1.1790	3.5735	4.7890	134.01
1	1.9	-4.3512	0.3	-4.4200	0.8	-0.8426	0.8	6.2593	1.1705	3.7149	5.0889	136.99
1	2	-4.3217	0.3	-4.4406	0.8	-0.6971	0.7	6.2355	1.1045	3.6700	5.1310	139.81
1	2.1	-4.4381	0.7	-4.5038	0.9	-0.5741	0.6	6.3490	1.2884	3.8187	5.0606	132.52
1	2.2	-4.6871	0.7	-4.3987	0.9	-0.6017	0.6	6.4560	1.2884	3.8722	5.1676	133.45
1	2.3	-4.6921	0.7	-4.2641	0.9	-0.6982	0.7	6.3785	1.3379	3.8582	5.0406	130.65
1	2.4	-5.0079	0.7	-4.2880	0.9	-0.9014	0.8	6.6542	1.3928	4.0235	5.2614	130.77
1	2.5	-5.0327	0.4	-4.3310	0.9	-1.1078	0.9	6.7315	1.3342	4.0328	5.3973	133.83
1	2.6	-5.0861	0.5	-4.1166	0.9	-0.7689	0.8	6.5883	1.3038	3.9461	5.2845	133.92
1	2.7	-5.1893	0	-4.1856	0.9	-0.8464	0.7	6.7204	1.1402	3.9303	5.5802	141.98
1	2.8	-5.2387	1.9	-3.7107	0.9	-0.8891	0.5	6.4811	2.1610	4.3210	4.3200	99.98
1	2.9	-6.1873	2.4	-3.5394	0.9	-0.9975	0.5	7.1976	2.6115	4.9046	4.5861	93.51
2	3	-7.0184	3	-3.7575	0.9	-1.2862	0.6	8.0642	3.1890	5.6266	4.8751	86.64
2	3.1	-16.8459	6.1	-3.6168	0.9	-1.7801	0.9	17.3215	6.2314	11.7764	11.0901	94.17
2	3.2	-21.8451	8.9	-3.5865	1	-2.5572	1.4	22.2848	9.0648	15.6748	13.2200	84.34
2	3.3	-25.3764	15.6	-3.7860	1.1	-3.9848	2.4	25.9649	15.8218	20.8934	10.1431	48.55
2	3.4	-29.9885	18.7	-4.5002	1.3	-5.1378	3.6	30.7565	19.0877	24.9221	11.6688	46.82
2	3.5	-37.5686	21.9	-5.1218	1.4	-6.2661	4.5	38.4304	22.4013	30.4159	16.0291	52.70
2	3.6	-39.6565	24.6	-5.3262	1.4	-6.9769	5.3	40.6162	25.2034	32.9098	15.4129	46.83
2	3.7	-42.6949	27.2	-5.6577	1.5	-7.7916	6.1	43.7673	27.9159	35.8416	15.8513	44.23

2	3.8	-45.4828	29.7	-5.7896	1.6	-8.2650	6.9	46.5888	30.5329	38.5609	16.0559	41.64
2	3.9	-48.5671	32.1	-6.0998	1.7	-9.3377	7.8	49.8314	33.0778	41.4546	16.7536	40.41
2	4	-51.2568	34.6	-6.5427	1.8	-10.1445	8.6	52.6591	35.6982	44.1786	16.9609	38.39
2	4.1	-54.4078	37.3	-7.0172	1.9	-10.8697	9.1	55.9250	38.4410	47.1830	17.4840	37.06
2	4.2	-56.6423	39.2	-7.1904	2	-11.0983	9.5	58.1654	40.3843	49.2749	17.7812	36.09
2	4.3	-57.4369	40.8	-7.0210	1.9	-11.4481	9.7	58.9860	41.9802	50.4831	17.0058	33.69
2	4.4	-57.8871	41.8	-6.9199	1.9	-11.5178	9.9	59.4261	42.9984	51.2122	16.4277	32.08
2	4.5	-57.9453	42.6	-7.0652	1.9	-11.9296	10.1	59.5809	43.8221	51.7015	15.7588	30.48
2	4.6	-58.7478	43.6	-6.8671	1.8	-12.4953	10.3	60.4532	44.8363	52.6447	15.6170	29.66
2	4.7	-60.0692	44.8	-6.5443	1.9	-12.5463	10.4	61.7134	46.0305	53.8720	15.6829	29.11
2	4.8	-61.3728	45.8	-6.6100	2	-12.8297	10.7	63.0469	47.0758	55.0614	15.9712	29.01
2	4.9	-62.5493	46.9	-6.9286	2	-13.2753	10.8	64.3168	48.1690	56.2429	16.1479	28.71
2	5	-62.9512	47.6	-6.7025	2.1	-13.0648	10.8	64.6410	48.8550	56.7480	15.7861	27.82
2	5.1	-62.8876	48	-6.6950	2.1	-13.1193	11	64.5894	49.2890	56.9392	15.3004	26.87
2	5.2	-63.1065	48.3	-6.8568	2.1	-13.5737	11.2	64.9129	49.6260	57.2695	15.2869	26.69
2	5.3	-63.5297	48.6	-6.7406	2.1	-13.6209	11.3	65.3222	49.9406	57.6314	15.3816	26.69
2	5.4	-63.6242	48.7	-6.6469	2.1	-13.7927	11.3	65.4405	50.0379	57.7392	15.4026	26.68
2	5.5	-63.7721	49	-6.7753	2.1	-14.1778	11.6	65.6795	50.3981	58.0388	15.2813	26.33
2	5.6	-64.1917	49.1	-6.6090	2.1	-14.4406	11.7	66.1271	50.5184	58.3227	15.6086	26.76
2	5.7	-64.3312	49.3	-6.8234	2.1	-14.5636	12.1	66.3111	50.8066	58.5589	15.5045	26.48
2	5.8	-64.9511	49.7	-6.9511	2.1	-15.3206	12.2	67.0946	51.2186	59.1566	15.8760	26.84

2	5.9	-65.1854	50.2	-6.4495	2.1	-14.9002	11.7	67.1770	51.5882	59.3826	15.5888	26.25
2	6	-65.1311	50.5	-5.7986	2.1	-13.6292	11.3	66.7940	51.7914	59.2927	15.0026	25.30
2	6.1	-65.2925	50.6	-6.2899	2.1	-13.7550	11.2	67.0215	51.8672	59.4444	15.1542	25.49
2	6.2	-65.3353	50.8	-6.4202	2.1	-13.5506	10.8	67.0339	51.9778	59.5058	15.0561	25.30
2	6.3	-65.1890	51	-6.0361	2.1	-12.9910	10.4	66.7443	52.0919	59.4181	14.6524	24.66
2	6.4	-65.1304	51.2	-6.0589	2.1	-12.5798	9.8	66.6103	52.1717	59.3910	14.4386	24.31
2	6.5	-64.6249	51.6	-6.0377	2.1	-11.8425	8.9	65.9779	52.4040	59.1909	13.5739	22.93
3	6.6	-63.6743	52.2	-5.5890	2.1	-10.6389	7.5	64.7985	52.7778	58.7882	12.0207	20.45
3	6.7	-62.4708	53	-5.7041	2.2	-8.8293	5.8	63.3489	53.3618	58.3554	9.9872	17.11
3	6.8	-60.9933	53.9	-5.7663	2.2	-7.2773	3.7	61.6960	54.0716	57.8838	7.6243	13.17
3	6.9	-60.0084	55.1	-5.3781	2.3	-5.2716	0.9	60.4791	55.1553	57.8172	5.3237	9.21
3	7	-59.6423	56.2	-6.2179	2.3	-3.2031	-1.8	60.0510	56.2758	58.1634	3.7752	6.49
4	7.1	-60.2040	57.2	-5.8295	2.3	-2.1441	-4.1	60.5235	57.3929	58.9582	3.1307	5.31
4	7.2	-60.3211	57.8	-6.1184	2.3	-1.5095	-5.5	60.6493	58.1066	59.3780	2.5427	4.28
4	7.3	-60.2208	58.1	-6.0894	2.3	-1.6872	-6.4	60.5514	58.4967	59.5240	2.0547	3.45
4	7.4	-60.1972	58.3	-6.1470	2.3	-1.6405	-6.8	60.5324	58.7403	59.6364	1.7922	3.01
4	7.5	-60.1654	58.5	-6.1534	2.3	-1.5195	-7.1	60.4984	58.9741	59.7363	1.5242	2.55
4	7.6	-60.2123	58.6	-6.1694	2.3	-1.5589	-7.3	60.5476	59.0977	59.8227	1.4499	2.42
4	7.7	-60.2220	58.6	-6.1522	2.3	-1.8449	-7.4	60.5635	59.1102	59.8368	1.4534	2.43
4	7.8	-60.1987	58.6	-6.1354	2.3	-1.6472	-7.6	60.5330	59.1355	59.8343	1.3975	2.34
4	7.9	-60.1941	58.7	-6.1253	2.3	-1.6486	-7.6	60.5274	59.2346	59.8810	1.2928	2.16

4	8	-60.1081	58.7	-6.1285	2.3	-1.5503	-7.7	60.4396	59.2475	59.8436	1.1921	1.99
4	8.1	-60.1235	58.7	-6.1305	2.3	-1.8851	-7.7	60.4647	59.2475	59.8561	1.2171	2.03
4	8.2	-60.1084	58.7	-6.1425	2.3	-1.6393	-7.8	60.4437	59.2606	59.8522	1.1831	1.98
4	8.3	-60.0608	58.7	-6.0966	2.3	-1.6693	-7.8	60.3925	59.2606	59.8266	1.1319	1.89
4	8.4	-60.0810	58.7	-6.0535	2.3	-1.7175	-7.9	60.4096	59.2739	59.8417	1.1358	1.90
4	8.5	-60.0228	58.8	-6.0515	2.3	-1.6878	-7.9	60.3507	59.3729	59.8618	0.9778	1.63
4	8.6	-60.0969	58.8	-6.0234	2.3	-1.6380	-7.9	60.4202	59.3729	59.8965	1.0473	1.75
4	8.7	-59.9963	58.8	-6.0258	2.3	-1.6363	-7.9	60.3203	59.3729	59.8466	0.9474	1.58
4	8.8	-60.0227	58.8	-5.9847	2.3	-1.5114	-7.9	60.3392	59.3729	59.8561	0.9664	1.61
4	8.9	-60.0807	58.8	-6.0354	2.3	-1.7376	-7.9	60.4081	59.3729	59.8905	1.0352	1.73

Table A - 4. Wedging Experiment - C: Results.

Region	Time	Left Fx	Right Fx	Left Fy	Right Fy	Left Fz	Right Fz	Left Resultant Force	Right Resultant Force	Ave Reaction Force	Diff. Reaction Force	Error %
1	0	-0.7029	0.1	-0.0926	0	-0.1464	-0.1	0.7239	0.1414	0.4327	0.5825	134.63
1	0.1	-1.0164	0.1	-0.0935	0	-0.1814	-0.1	1.0367	0.1414	0.5891	0.8953	151.99
1	0.2	-0.8594	0.2	-0.1284	0	-0.1012	-0.2	0.8748	0.2828	0.5788	0.5920	102.27
1	0.3	-1.4683	0.3	-0.2314	-0.1	-0.1970	-0.2	1.4995	0.3742	0.9368	1.1253	120.12
1	0.4	-1.2556	0.3	-0.3162	0	-0.2212	-0.1	1.3136	0.3162	0.8149	0.9974	122.39
1	0.5	-0.9644	0.3	-0.0549	0	-0.3554	-0.1	1.0293	0.3162	0.6728	0.7131	105.99
1	0.6	-1.4419	0.5	-0.1652	0	-0.4481	-0.2	1.5189	0.5385	1.0287	0.9804	95.30
1	0.7	-2.3520	0.8	-0.2589	0	-0.5739	-0.3	2.4348	0.8544	1.6446	1.5804	96.10
1	0.8	-3.1035	1.2	-0.5654	0.1	-0.4451	-0.3	3.1859	1.2410	2.2134	1.9449	87.87
1	0.9	-3.8749	1.6	-0.3785	0.1	-0.5335	-0.3	3.9297	1.6310	2.7803	2.2987	82.68
1	1	-4.2813	1.9	-0.4474	0.1	-0.3737	-0.3	4.3208	1.9261	3.1234	2.3946	76.67
1	1.1	-4.6156	2	-0.5802	0.1	-0.6059	-0.3	4.6912	2.0248	3.3580	2.6664	79.40
1	1.2	-5.1694	2.2	-0.6771	0	-0.9322	-0.2	5.2963	2.2091	3.7527	3.0872	82.27
2	1.3	-6.1851	2.5	-0.8913	0	-1.0013	0	6.3287	2.5000	4.4143	3.8287	86.73
2	1.4	-7.8632	3.4	-1.1645	-0.1	-1.4943	0.5	8.0882	3.4380	5.7631	4.6502	80.69
2	1.5	-11.9395	5.7	-1.9537	0	-2.2137	1.2	12.2992	5.8249	9.0621	6.4742	71.44
2	1.6	-18.9552	9.3	-3.4961	0.2	-3.3718	2	19.5676	9.5147	14.5412	10.0529	69.13

2	1.7	-26.1611	13.7	-3.9152	0.2	-4.8938	3	26.9014	14.0260	20.4637	12.8753	62.92
2	1.8	-34.1790	18.4	-3.7765	-0.1	-6.9127	4	35.0750	18.8300	26.9525	16.2449	60.27
2	1.9	-39.3413	23.1	-4.1157	-0.2	-8.2662	5.2	40.4105	23.6789	32.0447	16.7316	52.21
2	2	-46.3708	27.7	-5.0425	0.2	-10.9487	6.5	47.9119	28.4531	38.1825	19.4588	50.96
2	2.1	-50.5128	31.7	-5.8154	0.6	-12.7818	7.8	52.4284	32.6510	42.5397	19.7773	46.49
2	2.2	-55.1077	35.8	-6.7419	1.1	-14.9336	9.1	57.4920	36.9548	47.2234	20.5371	43.49
2	2.3	-58.7425	39.1	-6.7897	1.3	-16.1602	9.9	61.3020	40.3548	50.8284	20.9472	41.21
2	2.4	-60.1136	41.6	-6.8091	1.5	-16.0767	9.9	62.5977	42.7881	52.6929	19.8096	37.59
2	2.5	-59.9210	43	-7.0368	1.5	-16.4702	10.4	62.5404	44.2652	53.4028	18.2752	34.22
2	2.6	-61.1065	44.3	-7.0166	1.5	-17.0695	10.7	63.8327	45.5986	54.7156	18.2341	33.33
2	2.7	-61.4645	45.1	-7.2633	1.6	-17.1961	11.1	64.2366	46.4734	55.3550	17.7632	32.09
2	2.8	-61.8669	45.7	-7.3485	1.6	-17.4081	11.4	64.6882	47.1276	55.9079	17.5606	31.41
2	2.9	-62.1827	46.2	-7.2532	1.7	-17.3237	11.6	64.9570	47.6643	56.3107	17.2926	30.71
2	3	-62.6547	46.8	-7.5567	1.7	-17.7031	11.8	65.5448	48.2946	56.9197	17.2502	30.31
2	3.1	-63.0506	47.3	-7.3011	1.7	-17.7156	11.9	65.8979	48.8036	57.3507	17.0943	29.81
2	3.2	-62.9576	47.6	-7.3862	1.8	-17.7921	12.3	65.8390	49.1964	57.5177	16.6426	28.93
2	3.3	-63.1830	47.9	-7.5002	1.8	-17.9414	12.4	66.1078	49.5117	57.8097	16.5960	28.71
2	3.4	-63.2670	48.2	-7.5569	1.8	-17.3389	12.4	66.0337	49.8020	57.9179	16.2317	28.03
2	3.5	-63.4428	48.5	-7.6540	1.8	-17.4672	12.5	66.2470	50.1173	58.1822	16.1298	27.72
2	3.6	-63.6847	48.7	-7.7782	1.9	-17.4423	12.6	66.4866	50.3394	58.4130	16.1472	27.64
2	3.7	-63.5173	48.8	-7.8419	1.9	-17.5699	12.7	66.3675	50.4613	58.4144	15.9063	27.23

2	3.8	-63.4000	49.1	-7.9196	1.9	-17.3094	12.3	66.1959	50.6528	58.4243	15.5430	26.60
2	3.9	-62.5007	49.5	-7.6598	1.9	-17.0493	12.1	65.2357	50.9928	58.1143	14.2428	24.51
2	4	-61.9878	50	-7.7214	2	-16.4982	11.9	64.6088	51.4355	58.0222	13.1733	22.70
2	4.1	-61.5868	50.7	-8.0615	2	-15.4583	11.6	64.0069	52.0485	58.0277	11.9583	20.61
2	4.2	-61.1434	50.9	-8.3049	2	-14.9543	11.3	63.4911	52.1776	57.8344	11.3135	19.56
2	4.3	-60.5714	50.9	-7.8936	2	-13.5674	11	62.5721	52.1134	57.3428	10.4587	18.24
2	4.4	-60.2016	50.8	-7.4768	2	-12.3571	10.8	61.9099	51.9738	56.9419	9.9360	17.45
2	4.5	-59.9522	50.6	-7.6358	2	-11.5744	10.1	61.5349	51.6369	56.5859	9.8980	17.49
2	4.6	-59.9669	50.3	-7.6827	2	-10.8473	9.8	61.4225	51.2848	56.3536	10.1377	17.99
2	4.7	-59.8038	50.1	-7.7196	2	-10.1578	9.5	61.1496	51.0320	56.0908	10.1176	18.04
2	4.8	-59.8213	49.8	-7.6144	2	-10.0125	9.3	61.1295	50.7004	55.9149	10.4291	18.65
2	4.9	-60.0155	49.6	-7.5606	2	-10.0058	9.2	61.3118	50.4856	55.8987	10.8262	19.37
2	5	-59.9904	49.6	-7.2597	2	-9.6140	8.7	61.1880	50.3969	55.7925	10.7911	19.34
3	5.1	-59.9789	49.8	-7.3023	2	-8.9452	7.6	61.0803	50.4163	55.7483	10.6641	19.13
3	5.2	-59.8256	50.7	-7.3331	2	-7.9413	6.5	60.7942	51.1541	55.9742	9.6401	17.22
3	5.3	-58.9936	52.1	-7.0730	2.1	-6.4824	5.5	59.7686	52.4316	56.1001	7.3370	13.08
3	5.4	-58.6176	53.6	-6.1094	2	-4.1950	2	59.0843	53.6746	56.3794	5.4097	9.60
3	5.5	-58.6307	54.9	-5.4365	2	-3.1953	-1	58.9689	54.9455	56.9572	4.0233	7.06
3	5.6	-58.5883	55.9	-5.4734	2	-2.3726	-3.3	58.8912	56.0330	57.4621	2.8582	4.97
4	5.7	-58.5232	56.5	-5.6080	1.9	-2.3091	-4.7	58.8366	56.7270	57.7818	2.1096	3.65
4	5.8	-58.7518	56.9	-5.6283	1.9	-2.2559	-5.5	59.0639	57.1968	58.1303	1.8671	3.21

4	5.9	-58.8445	57.1	-5.6194	1.9	-2.4144	-6.1	59.1615	57.4563	58.3089	1.7052	2.92
4	6	-58.8250	57.2	-5.5447	1.9	-2.2662	-6.3	59.1292	57.5773	58.3532	1.5519	2.66
4	6.1	-58.8470	57.3	-5.5480	1.9	-2.3937	-6.5	59.1564	57.6988	58.4276	1.4576	2.49
4	6.2	-58.8708	57.4	-5.5914	1.9	-2.4030	-6.7	59.1845	57.8209	58.5027	1.3636	2.33
4	6.3	-58.7578	57.4	-5.5546	1.9	-2.2732	-6.8	59.0636	57.8326	58.4481	1.2310	2.11
4	6.4	-58.7727	57.4	-5.5478	1.9	-2.2563	-6.8	59.0771	57.8326	58.4548	1.2445	2.13
4	6.5	-58.8235	57.5	-5.5687	1.9	-2.3435	-6.9	59.1330	57.9437	58.5383	1.1893	2.03
4	6.6	-58.8443	57.5	-5.5594	1.9	-2.3119	-7	59.1515	57.9557	58.5536	1.1959	2.04
4	6.7	-58.7413	57.5	-5.5661	1.9	-2.3527	-6.9	59.0513	57.9437	58.4975	1.1077	1.89
4	6.8	-58.7203	57.5	-5.5286	1.9	-2.4545	-7	59.0310	57.9557	58.4933	1.0753	1.84
4	6.9	-58.7230	57.5	-5.5179	1.9	-2.2641	-7	59.0251	57.9557	58.4904	1.0695	1.83
4	7	-58.7176	57.5	-5.4742	1.9	-2.3151	-7.1	59.0176	57.9678	58.4927	1.0498	1.79

The Region 1 in the figures is where the peg is in contact with the hole, Region 2 is where the peg is rotated, Region 3 is where the peg is released, and Region 4 is where the peg is successfully wedged.

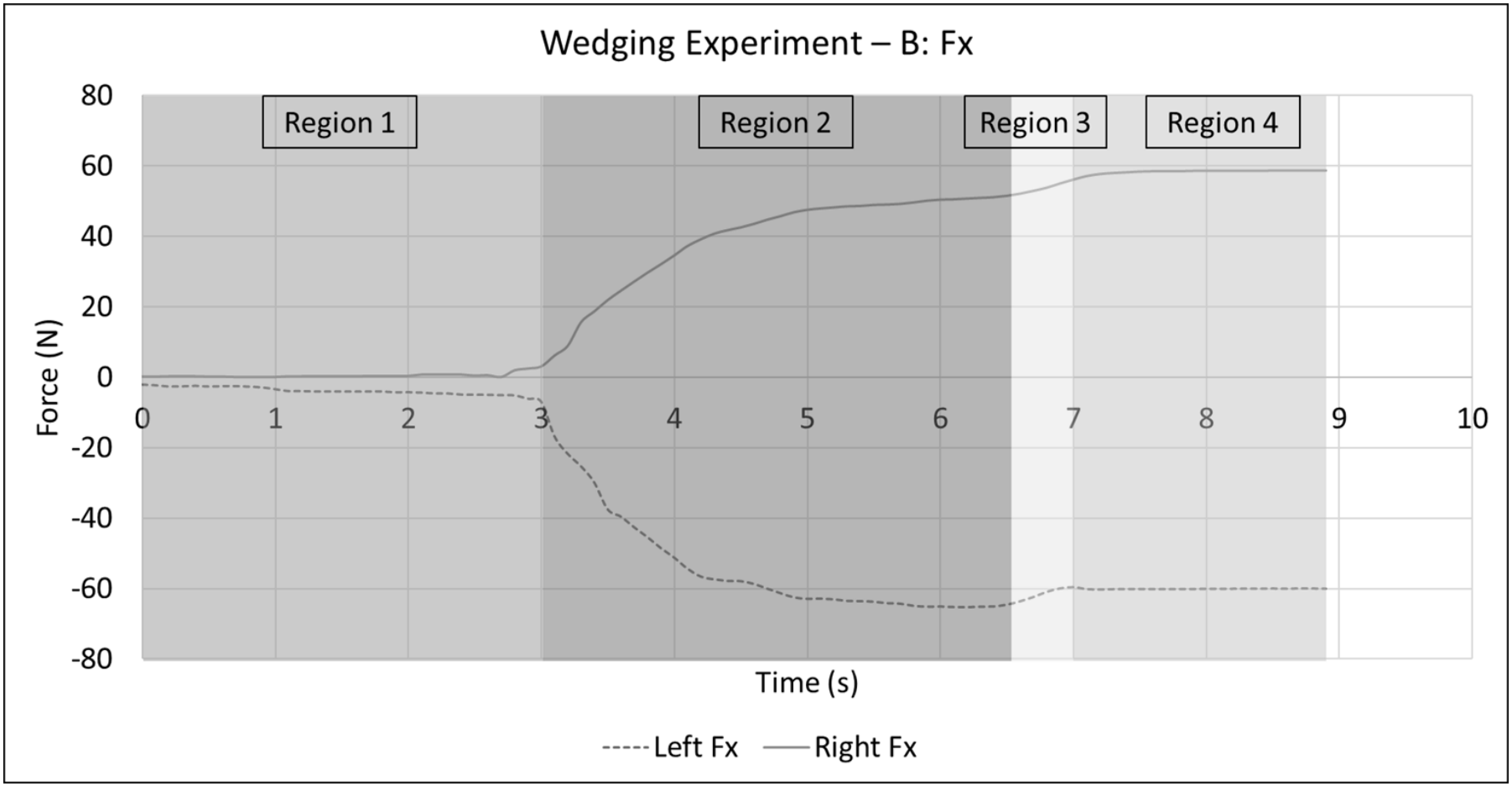

Figure A - 3. Wedging Experiment - B: Fx

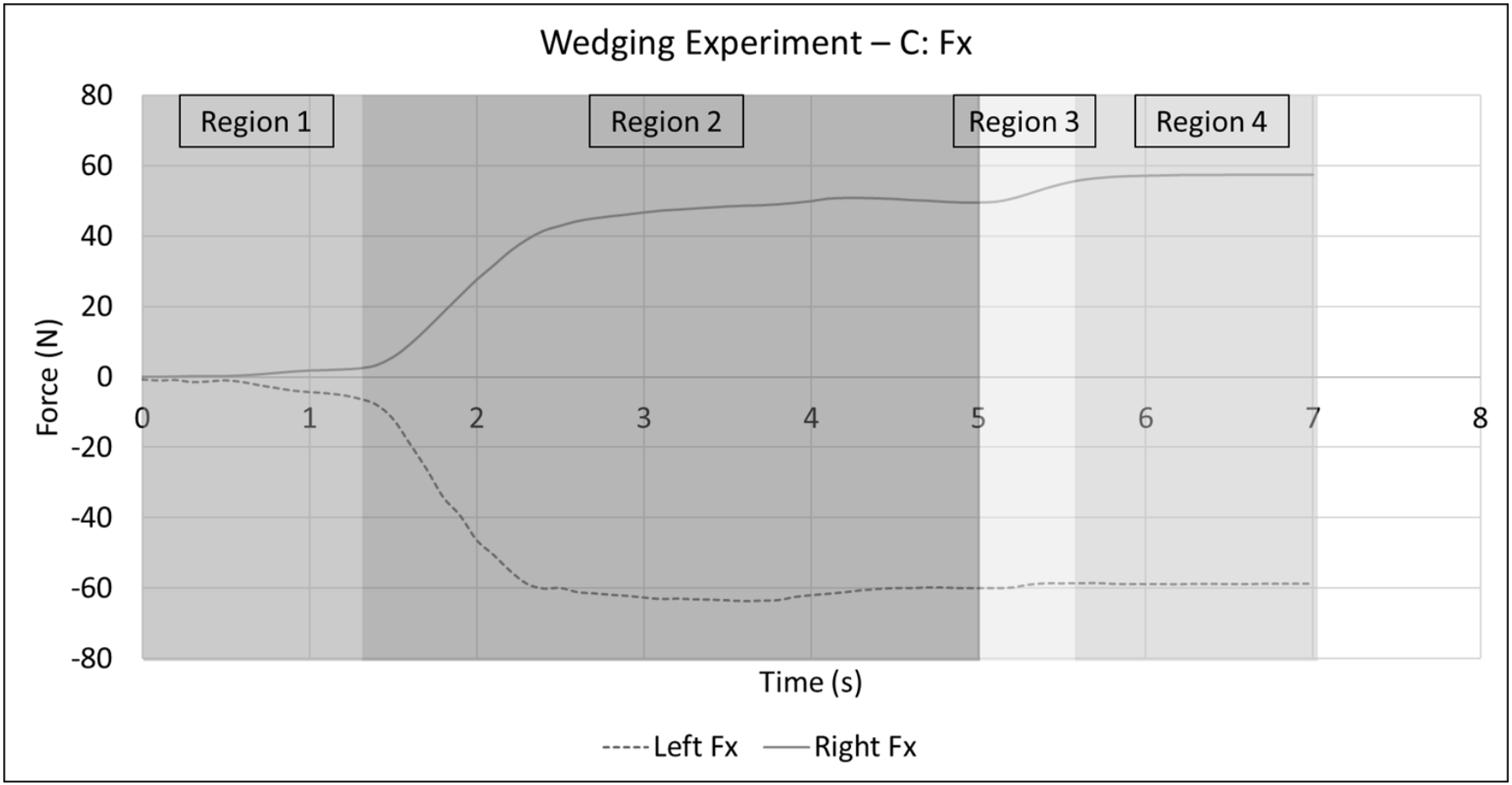

Figure A - 4. Wedging Experiment - C: Fx

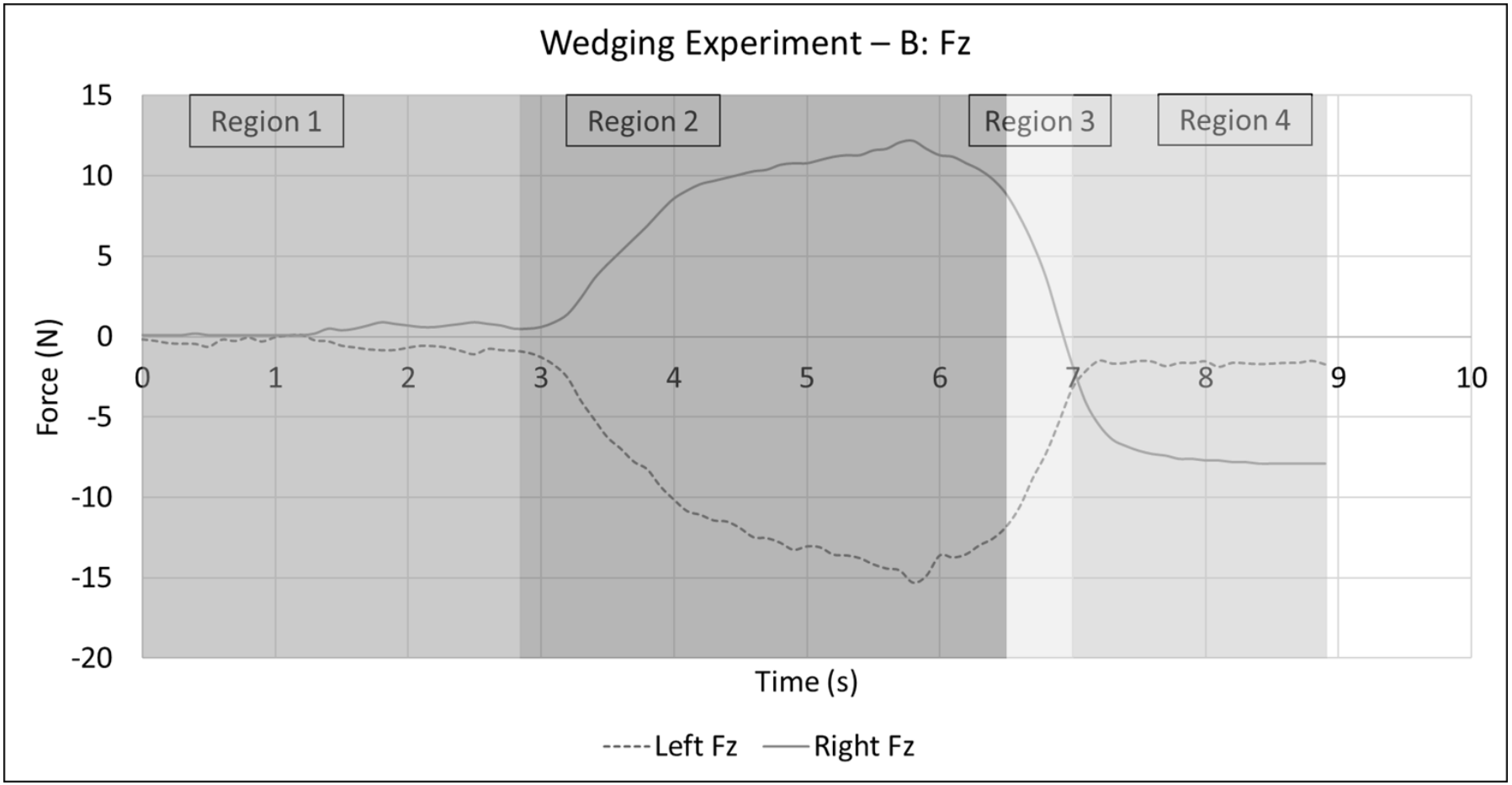

Figure A - 5. Wedging Experiment - B: Fz

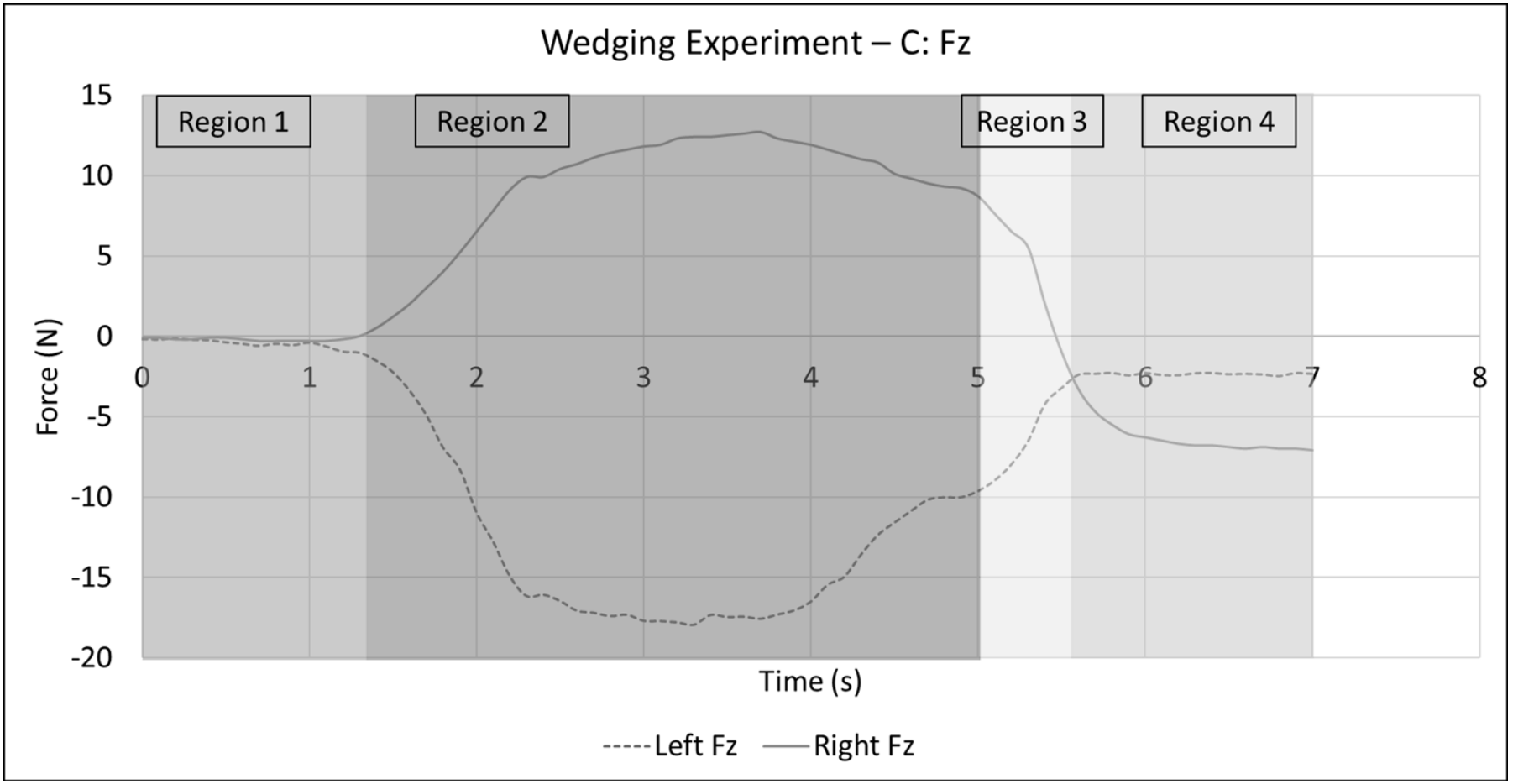

Figure A - 6. Wedging Experiment - C: Fz

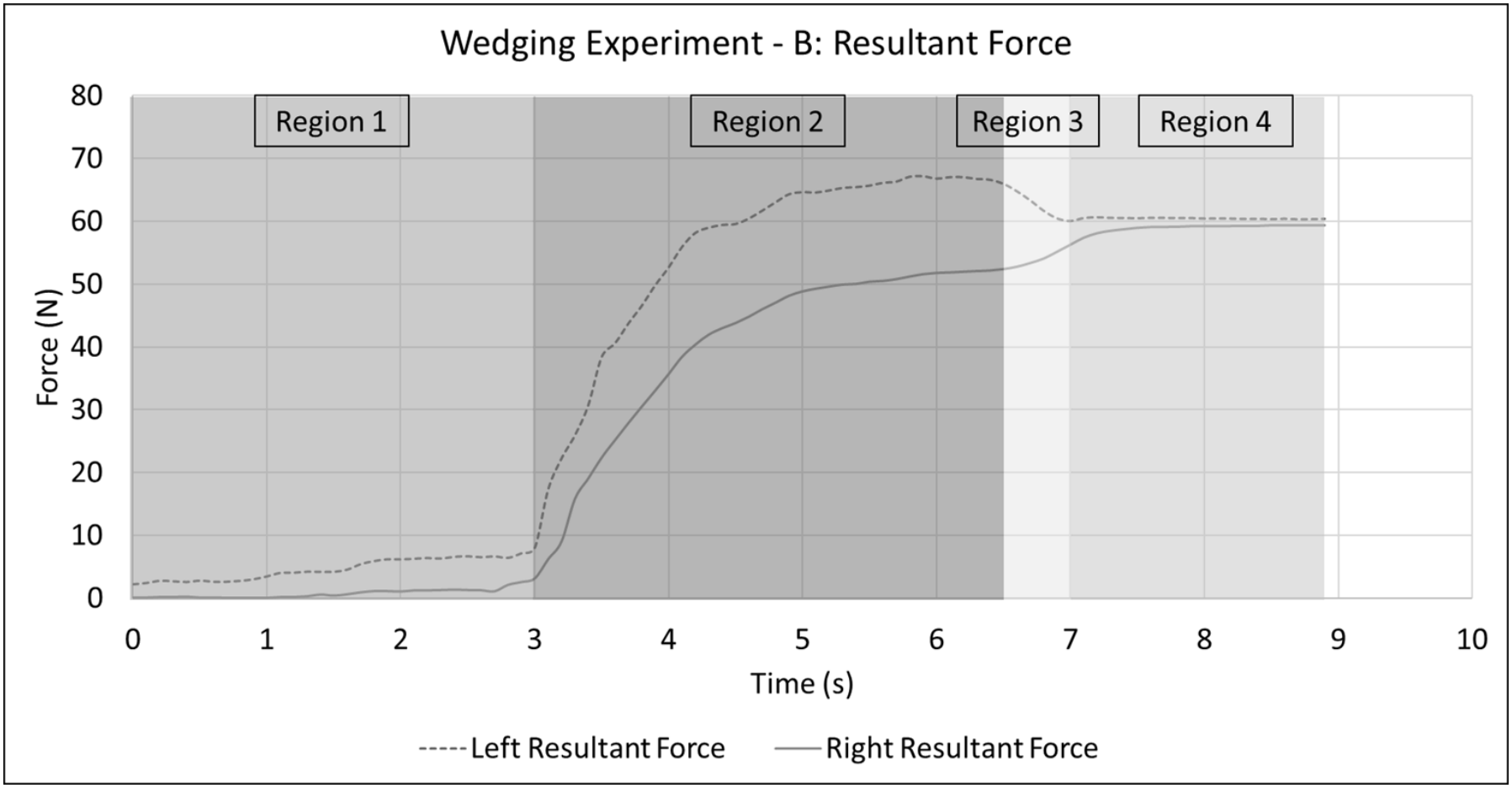

Figure A - 7. Wedging Experiment - B: The resultant forces

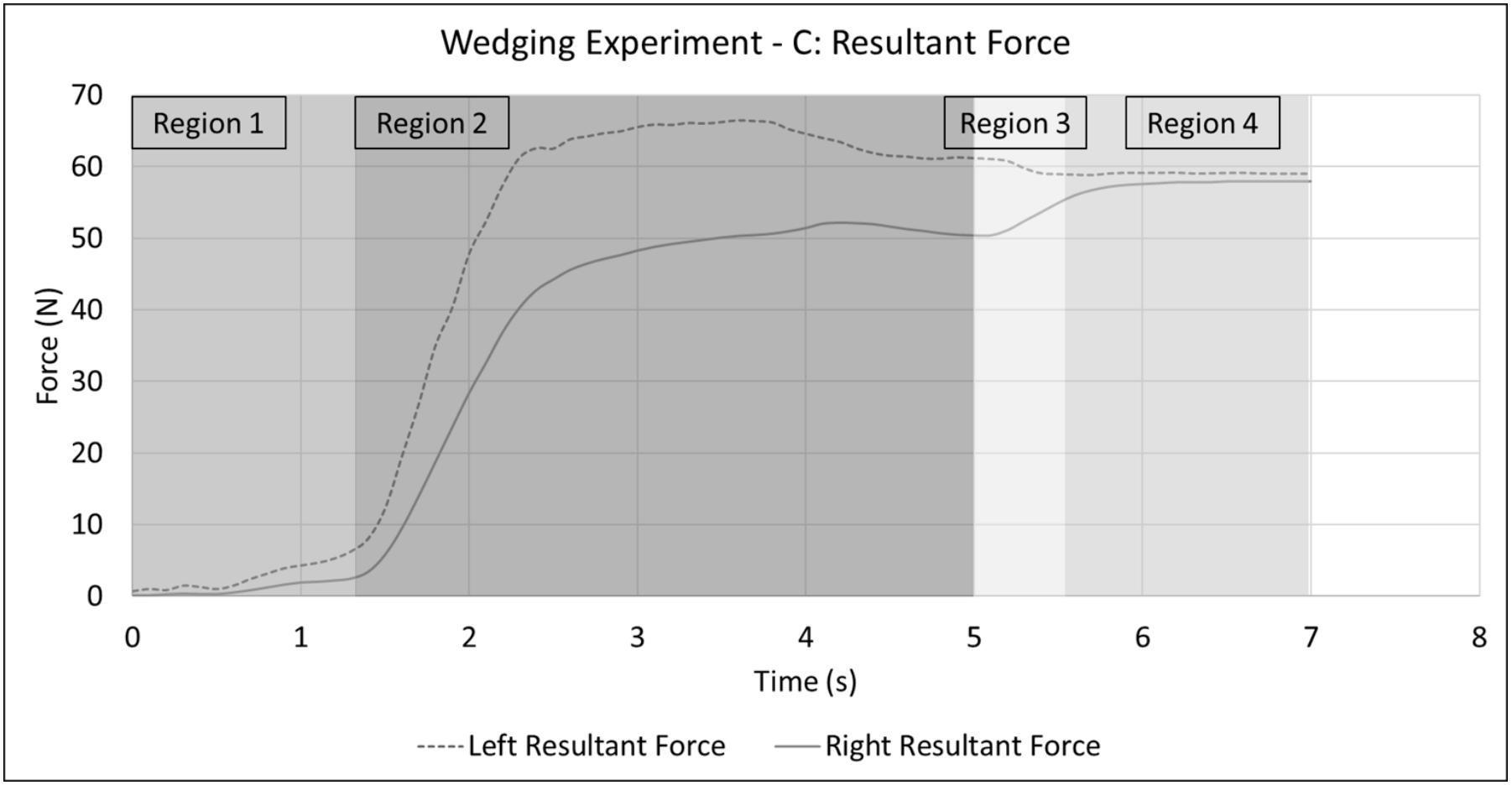

Figure A - 8. Wedging Experiment - C: The resultant forces

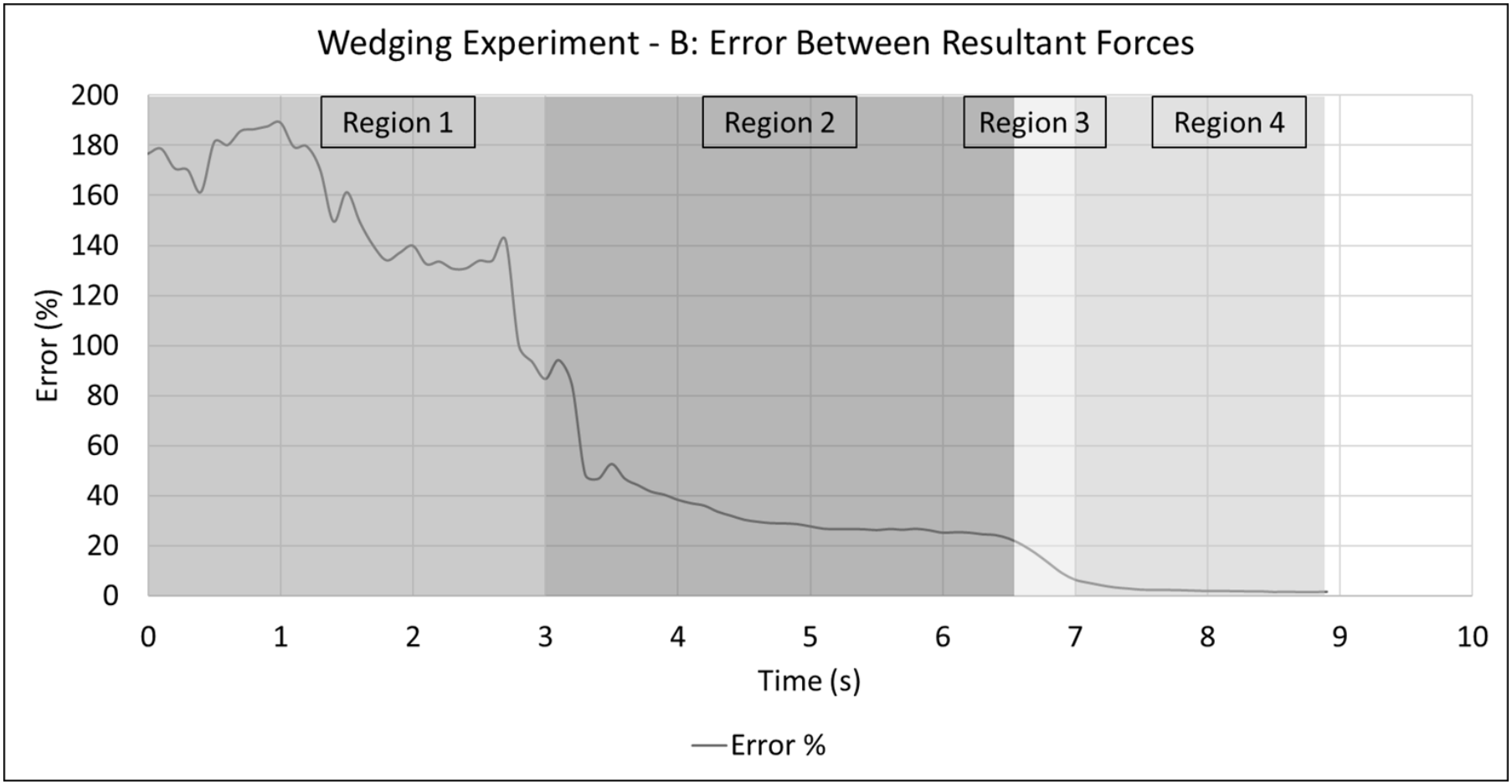

Figure A - 9. Wedging Experiment - B: Error between resultant forces

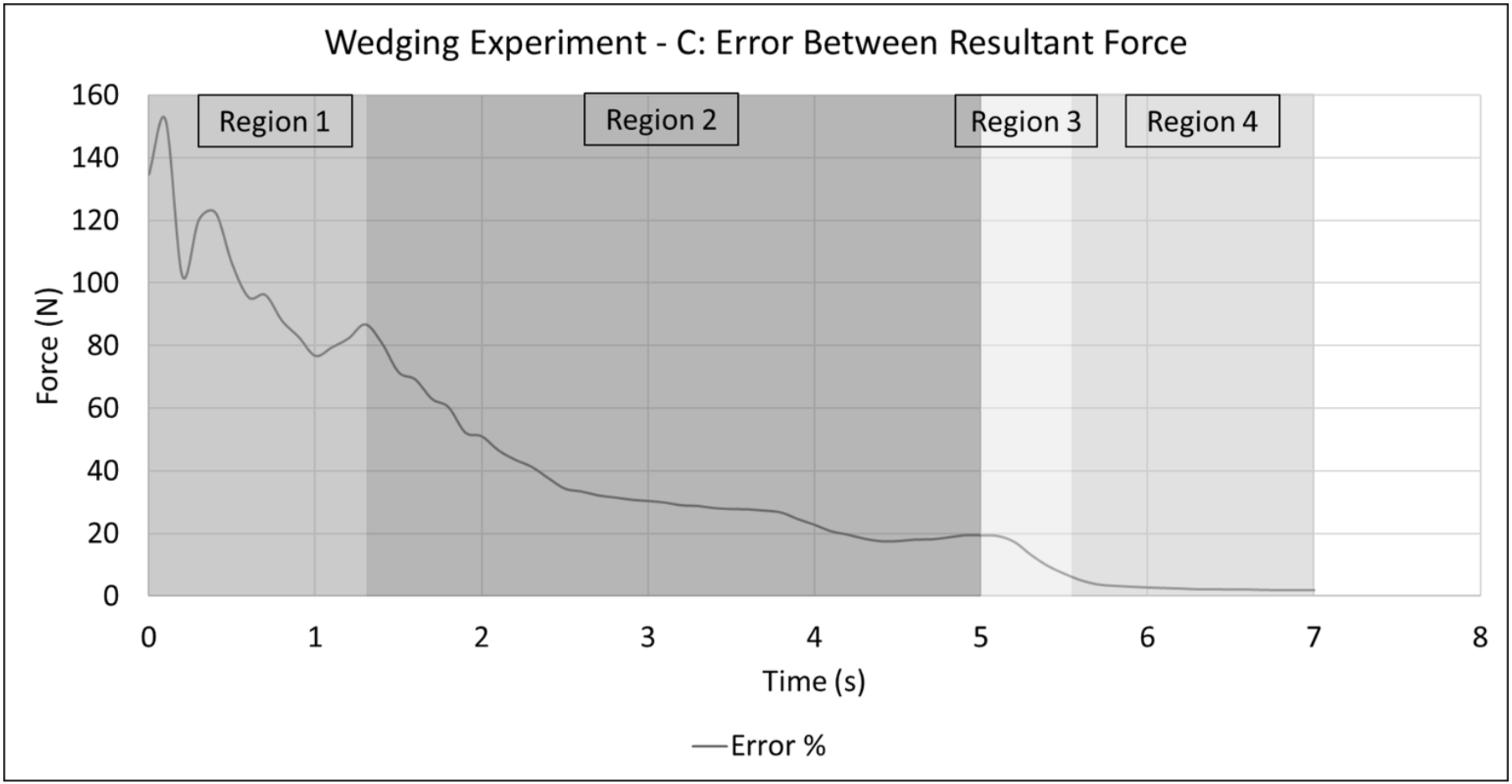

Figure A - 10. Wedging Experiment - C: Error between resultant forces

Appendix B: Dislodging a Peg Using Impulses

Table A - 5. Frame number when the peg is dislodged - Case 1: 7 mm.

		Pulling force magnitude (N)											
		20.20	**20.21**	**20.22**	**20.23**	**20.24**	**20.25**	**20.26**	**20.27**	**20.28**	**20.29**	**20.30**	**20.35**
Frequency (Hz)	**Continuous**	3	3	3	3	3	3	3	3	3	3	3	3
	50 Hz	15	11	11	7	7	7	7	7	7	3	3	3
	40 Hz	18	13	13	8	8	8	8	8	8	3	3	3
	30 Hz		16	16	9	9	9	9	9	9	3	3	3
	20 Hz				13	13	13	13	13	13	3	3	3
	10 Hz										3	3	3
		Pulling force magnitude (N)											
		20.40	**20.50**	**20.70**	**21.00**	**21.50**	**21.51**	**21.52**	**21.55**	**21.60**	**22.00**	**22.50**	**23.00**
Frequency (Hz)	**Continuous**	3	3	3	3	3	2	2	2	2	2	2	2
	50 Hz	3	3	3	3	3	2	2	2	2	2	2	2
	40 Hz	3	3	3	3	3	2	2	2	2	2	2	2
	30 Hz	3	3	3	3	3	2	2	2	2	2	2	2
	20 Hz	3	3	3	3	3	2	2	2	2	2	2	2
	10 Hz	3	3	3	3	3	2	2	2	2	2	2	2

Table A - 6. Impulse required to dislodge the peg - Case 1: 7 mm.

		Pulling force magnitude (N)											
		20.20	**20.21**	**20.22**	**20.23**	**20.24**	**20.25**	**20.26**	**20.27**	**20.28**	**20.29**	**20.30**	**20.35**
Frequency (Hz)	**Continuous**	0.2020	0.2021	0.2022	0.2023	0.2024	0.2025	0.2028	0.2028	0.2028	0.2029	0.2030	0.2035
	50 Hz	0.7828	0.5810	0.5813	0.3793	0.3795	0.3797	0.3803	0.3803	0.3803	0.1775	0.1776	0.1781
	40 Hz	0.7828	0.5810	0.5813	0.3793	0.3795	0.3797	0.3803	0.3803	0.3803	0.1775	0.1776	0.1781
	30 Hz		0.5611	0.5614	0.3399	0.3400	0.3402	0.3407	0.3407	0.3407	0.1775	0.1776	0.1781
	20 Hz				0.3793	0.3795	0.3797	0.3803	0.3803	0.3803	0.1775	0.1776	0.1781
	10 Hz										0.1775	0.1776	0.1781
		Pulling force magnitude (N)											
Frequency (Hz)		**20.40**	**20.50**	**20.70**	**21.00**	**21.50**	**21.51**	**21.52**	**21.55**	**21.60**	**22.00**	**22.50**	**23.00**
	Continuous	0.2040	0.2050	0.2070	0.2100	0.2150	0.1076	0.1076	0.1078	0.1080	0.1100	0.1125	0.1150
	50 Hz	0.1785	0.1794	0.1811	0.1838	0.1881	0.1076	0.1076	0.1078	0.1080	0.1100	0.1125	0.1150
	40 Hz	0.1785	0.1794	0.1811	0.1838	0.1881	0.1076	0.1076	0.1078	0.1080	0.1100	0.1125	0.1150
	30 Hz	0.1785	0.1794	0.1811	0.1838	0.1881	0.1076	0.1076	0.1078	0.1080	0.1100	0.1125	0.1150
	20 Hz	0.1785	0.1794	0.1811	0.1838	0.1881	0.1076	0.1076	0.1078	0.1080	0.1100	0.1125	0.1150
	10 Hz	0.1785	0.1794	0.1811	0.1838	0.1881	0.1076	0.1076	0.1078	0.1080	0.1100	0.1125	0.1150

Table A - 7. Frame number when the peg is dislodged - Case 2: 8 mm.

		Pulling force magnitude (N)												
		22.50	**22.55**	**22.56**	**22.57**	**22.58**	**22.59**	**22.60**	**22.61**	**22.62**	**22.63**	**22.64**	**22.65**	**22.66**
Frequency (Hz)	**Continuous**	3	3	3	3	3	3	3	3	3	3	3	3	3
	50 Hz		19	15	15	11	11	11	7	7	7	7	7	7
	40 Hz			18	18	13	13	13	8	8	8	8	8	8
	30 Hz					16	16	16	9	9	9	9	9	9
	20 Hz								13	13	13	13	13	13
	10 Hz													
			Pulling force magnitude (N)											
		22.67	**22.70**	**22.75**	**22.80**	**22.90**	**23.00**	**23.50**	**23.85**	**23.89**	**23.90**	**24.00**	**24.50**	**25.00**
Frequency (Hz)	**Continuous**	3	3	3	3	3	3	3	3	3	2	2	2	2
	50 Hz	3	3	3	3	3	3	3	3	3	2	2	2	2
	40 Hz	3	3	3	3	3	3	3	3	3	2	2	2	2
	30 Hz	3	3	3	3	3	3	3	3	3	2	2	2	2
	20 Hz	3	3	3	3	3	3	3	3	3	2	2	2	2
	10 Hz	3	3	3	3	3	3	3	3	3	2	2	2	2

Table A - 8. Impulse required to dislodge the peg - Case 2: 8 mm.

		Pulling force magnitude (N)												
		22.50	**22.55**	**22.56**	**22.57**	**22.58**	**22.59**	**22.60**	**22.61**	**22.62**	**22.63**	**22.64**	**22.65**	**22.66**
Frequency (Hz)	**Continuous**	0.2250	0.2255	0.2256	0.2257	0.2258	0.2259	0.2260	0.2261	0.2262	0.2263	0.2264	0.2265	0.2266
	50 Hz				0.8746	0.6492	0.6495	0.6498	0.4239	0.4241	0.4243	0.4245	0.4247	0.4249
	40 Hz				0.8746	0.6492	0.6495	0.6498	0.4239	0.4241	0.4243	0.4245	0.4247	0.4249
	30 Hz					0.6269	0.6272	0.6278	0.3799	0.3800	0.3802	0.3800	0.3805	0.3807
	20 Hz								0.4239	0.4241	0.4243	0.4245	0.4247	0.4249
	10 Hz													
		Pulling force magnitude (N)												
		22.67	**22.70**	**22.75**	**22.80**	**22.90**	**23.00**	**23.50**	**23.85**	**23.89**	**23.90**	**24.00**	**24.50**	**25.00**
Frequency (Hz)	**Continuous**	0.2267	0.2270	0.2275	0.2280	0.2290	0.2300	0.2350	0.2385	0.2389	0.1195	0.1200	0.1225	0.1250
	50 Hz	0.1984	0.1986	0.1991	0.1995	0.2004	0.2013	0.2350	0.2385	0.2389	0.1195	0.1200	0.1225	0.1250
	40 Hz	0.1984	0.1986	0.1991	0.1995	0.2004	0.2013	0.2350	0.2385	0.2389	0.1195	0.1200	0.1225	0.1250
	30 Hz	0.1984	0.1986	0.1991	0.1995	0.2004	0.2013	0.2350	0.2385	0.2389	0.1195	0.1200	0.1225	0.1250
	20 Hz	0.1984	0.1986	0.1991	0.1995	0.2004	0.2013	0.2350	0.2385	0.2389	0.1195	0.1200	0.1225	0.1250
	10 Hz	0.1984	0.1986	0.1991	0.1995	0.2004	0.2013	0.2350	0.2385	0.2389	0.1195	0.1200	0.1225	0.1250

Appendix C: The Passive Compliant Gough-Whitehall-Stewart Mechanism for Peg-Hole Assembly and Disassembly.

Table A - 9 to Table A - 20 are the full results for the first comparison between the approximation matrix and numerical validation model from Chapter 5.2.3 with the variables below:

$$b = 50\ mm$$
$$L = 50mm\ Vs.\ 60mm$$
$$\theta_L = \ 70\ °$$
$$k = 200\ N/m$$

Table A - 9. Complete results of the first comparison for translation for $L = 50mm$: X – Translation.

X Translation (mm)	Approximation Matrix						Numerical Validation Model						Error (%)
	ΣFx	ΣFy	ΣFz	ΣMx	ΣMy	ΣMz	ΣFx	ΣFy	ΣFz	ΣMx	ΣMy	ΣMz	
0.1	7.0187	0	0	0	0	0	7.0187	0	0.0500	0.1536	-0.0079	0	0
0.2	14.037	0	0	0	0	0	14.038	0	0.2000	0.6143	-0.0629	-0.0011	0.0029
0.3	21.056	0	0	0	0	0	21.057	0	0.4500	1.3821	-0.2122	-0.0038	0.0062
0.4	28.075	0	0	0	0	0	28.078	0	0.8000	2.4571	-0.5031	-0.0091	0.0107
0.5	35.093	0	0	0	0	0	35.090	0	1.2499	3.8391	-0.9826	-0.0177	0.0168
0.6	42.112	0	0	0	0	0	42.122	0	1.7999	5.5282	-1.6979	-0.0306	0.0234
0.7	49.131	0	0	0	0	0	49.147	0	2.4498	7.5242	-2.6962	-0.0485	0.0326
0.8	56.149	0	0	0	0	0	56.173	0	3.1997	9.8272	-4.0246	-0.0724	0.0427
0.9	63.168	0	0	0	0	0	63.202	0	4.0496	12.437	-5.7304	-0.1031	0.054
1	70.187	0	0	0	0	0	70.234	0	4.9995	15.354	-7.8605	-0.1415	0.0667

Table A - 10. Complete results of the first comparison for translation for $L = 50mm$: Y – Translation.

Y Translation (mm)	Approximation Matrix						Numerical Validation Model						Error (%)
	ΣFx	ΣFy	ΣFz	ΣMx	ΣMy	ΣMz	ΣFx	ΣFy	ΣFz	ΣMx	ΣMy	ΣMz	
0.1	0	7.0187	0	0	0	0	0	7.0187	0.0500	-0.1457	0	0	0.0002
0.2	0	14.037	0	0	0	0	0	14.038	0.2000	-0.5514	0	0	0.0029
0.3	0	21.056	0	0	0	0	0	21.057	0.4500	-1.1699	0	0	0.006
0.4	0	28.075	0	0	0	0	0	28.078	0.8000	-1.954	0	0	0.0106
0.5	0	35.093	0	0	0	0	0	35.099	1.241	-2.8565	0	0	0.0168
0.6	0	42.112	0	0	0	0	0	42.122	1.7999	-3.8302	0	0	0.0240
0.7	0	49.131	0	0	0	0	0	49.147	2.4498	-4.8279	0	0	0.0326
0.8	0	56.149	0	0	0	0	0	56.173	3.1998	-5.8024	0	0	0.0428
0.9	0	63.168	0	0	0	0	0	63.202	4.0497	-6.7065	0	0	0.0540
1	0	70.187	0	0	0	0	0	70.234	4.9995	-7.4928	0	0	0.0667

Table A - 11. Complete results of the first comparison for translation for $L = 50mm$: Z – Translation.

Z Translation (mm)	Approximation Matrix						Numerical Validation Model						Error (%)
	ΣFx	ΣFy	ΣFz	ΣMx	ΣMy	ΣMz	ΣFx	ΣFy	ΣFz	ΣMx	ΣMy	ΣMz	
0.1	0	0	105.96	0	0	0	0	0	105.98	0	0	0	0.0200
0.2	0	0	211.93	0	0	0	0	0	212.00	0	0	0	0.0401
0.3	0	0	317.89	0	0	0	0	0	318.08	0	0	0	0.0600
0.4	0	0	423.85	0	0	0	0	0	424.19	0	0	0	0.0799
0.5	0	0	529.81	0	0	0	0	0	530.34	0	0	0	0.0998
0.6	0	0	635.78	0	0	0	0	0	636.54	0	0	0	0.1196
0.7	0	0	741.74	0	0	0	0	0	742.77	0	0	0	0.1393
0.8	0	0	847.70	0	0	0	0	0	849.05	0	0	0	0.1590
0.9	0	0	953.66	0	0	0	0	0	955.37	0	0	0	0.1787
1	0	0	1059.6	0	0	0	0	0	1061.7	0	0	0	0.1982

Table A - 12. Complete results of the first comparison for translation for $L = 50mm$: X – Rotation.

X Rotation (rad)	Approximation Matrix						Numerical Validation Model						Error (%)
	ΣFx	ΣFy	ΣFz	ΣMx	ΣMy	ΣMz	ΣFx	ΣFy	ΣFz	ΣMx	ΣMy	ΣMz	
0.005	0	0	0	2207.6	0	0	0	-0.0245	1.1324	2210.6	0	0	0.1345
0.01	0	0	0	4415.1	0	0	0	-0.0877	4.5294	4428.6	0	0	0.3048
0.02	0	0	0	8830.2	0	0	0	-0.2668	18.116	8895.1	0	0	0.7348
0.03	0	0	0	13245	0	0	0	-0.4119	40.754	13416	0	0	1.2919
0.04	0	0	0	17660	0	0	0	-0.398	72.434	18008	0	0	1.9707
0.05	0	0	0	22076	0	0	0	-0.1004	113.14	22687	0	0	2.7678

Table A - 13. Complete results of the first comparison for translation for $L = 50mm$: Y – Rotation.

Y Rotation (rad)	Approximation Matrix						Numerical Validation Model						Error (%)
	ΣFx	ΣFy	ΣFz	ΣMx	ΣMy	ΣMz	ΣFx	ΣFy	ΣFz	ΣMx	ΣMy	ΣMz	
0.005	0	0	0	0	2207.6	0	-0.0026	0.0272	1.1324	-2.6664	2207.9	-0.014	0.0138
0.01	0	0	0	0	4415.1	0	-0.021	0.1087	4.5294	-10.664	4417.9	-0.1118	0.0633
0.02	0	0	0	0	8830.2	0	-0.1678	0.4343	18.116	-42.633	8852.5	-0.8939	0.2525
0.03	0	0	0	0	13245	0	-0.5661	0.9768	40.753	-95.835	13320	-3.0147	0.57
0.04	0	0	0	0	17660	0	-1.3413	1.7354	72.431	-170.15	17838	-7.1387	1.0109
0.05	0	0	0	0	22076	0	-2.6183	2.7092	113.14	-265.42	22423	-13.925	1.5727

Table A - 14. Complete results of the first comparison for translation for $L = 50mm$: Z – Rotation.

Z Rotation (rad)	Approximation Matrix						Numerical Validation Model						Error (%)
	ΣFx	ΣFy	ΣFz	ΣMx	ΣMy	ΣMz	ΣFx	ΣFy	ΣFz	ΣMx	ΣMy	ΣMz	
0.005	0	0	0	0	0	584.89	0	0	0.2199	0	0	584.9	0.0014
0.01	0	0	0	0	0	1169.8	0	0	0.8797	0	0	1169.8	0.0037
0.02	0	0	0	0	0	2339.6	0	0	3.5188	0	0	2340.1	0.0205
0.03	0	0	0	0	0	3509.3	0	0	7.9168	0	0	3511.1	0.0513
0.04	0	0	0	0	0	4679.1	0	0	14.073	0	0	4683.3	0.0898
0.05	0	0	0	0	0	5848.9	0	0	21.987	0	0	5857.1	0.1397

Table A - 15. Complete results of the first comparison for translation for $L = 60mm$: X – Translation.

X Translation (mm)	Approximation Matrix						Numerical Validation Model						Error (%)
	ΣFx	ΣFy	ΣFz	ΣMx	ΣMy	ΣMz	ΣFx	ΣFy	ΣFz	ΣMx	ΣMy	ΣMz	
0.1	7.0187	0	0	0	0	0	7.0187	0	0.0565	0.1734	-0.0100	0	0
0.2	14.037	0	0	0	0	0	14.038	0	0.2258	0.6937	-0.080	-0.0014	0.0036
0.3	21.056	0	0	0	0	0	21.058	0	0.5081	1.5607	-0.2707	-0.0049	0.0076
0.4	28.075	0	0	0	0	0	28.079	0	0.9033	2.7746	-0.6415	-0.0115	0.0135
0.5	35.093	0	0	0	0	0	35.101	0	1.4115	4.3352	-1.253	-0.0226	0.0214
0.6	42.112	0	0	0	0	0	42.125	0	2.0325	6.2425	-2.1652	-0.039	0.0306
0.7	49.131	0	0	0	0	0	49.151	0	2.7664	8.4964	-3.4382	-0.0619	0.0415
0.8	56.149	0	0	0	0	0	56.180	0	3.6133	11.097	-5.1321	-0.0924	0.0545
0.9	63.168	0	0	0	0	0	63.212	0	4.573	14.044	-7.3072	-0.1315	0.0689
1	70.187	0	0	0	0	0	70.246	0	5.6456	17.337	-10.023	-0.1804	0.0851

Table A - 16. Complete results of the first comparison for translation for $L = 60mm$: Y – Translation.

Y Translation (mm)	Approximation Matrix						Numerical Validation Model						Error (%)
	ΣFx	ΣFy	ΣFz	ΣMx	ΣMy	ΣMz	ΣFx	ΣFy	ΣFz	ΣMx	ΣMy	ΣMz	
0.1	0	7.0187	0	0	0	0	0	7.0187	0.0565	-0.1634	0	0	0.0004
0.2	0	14.037	0	0	0	0	0	14.038	0.2258	-0.6135	0	0	0.0036
0.3	0	21.056	0	0	0	0	0	21.058	0.5081	-1.2901	0	0	0.0077
0.4	0	28.075	0	0	0	0	0	28.079	0.9033	-2.1331	0	0	0.0135
0.5	0	35.093	0	0	0	0	0	35.101	1.4115	-3.0822	0	0	0.0214
0.6	0	42.112	0	0	0	0	0	42.125	2.0325	-4.0772	0	0	0.0306
0.7	0	49.131	0	0	0	0	0	49.151	2.7664	-5.0581	0	0	0.0416
0.8	0	56.149	0	0	0	0	0	56.180	3.6133	-5.9645	0	0	0.0545
0.9	0	63.168	0	0	0	0	0	63.212	4.5730	-6.7362	0	0	0.0689
1	0	70.187	0	0	0	0	0	70.246	5.6456	-7.3129	0	0	0.0850

Table A - 17. Complete results of the first comparison for translation for $L = 60mm$: Z – Translation.

Z Translation (mm)	Approximation Matrix						Numerical Validation Model						Error (%)
	ΣFx	ΣFy	ΣFz	ΣMx	ΣMy	ΣMz	ΣFx	ΣFy	ΣFz	ΣMx	ΣMy	ΣMz	
0.1	0	0	105.96	0	0	0	0	0	105.99	0	0	0	0.0226
0.2	0	0	211.93	0	0	0	0	0	212.02	0	0	0	0.0452
0.3	0	0	317.89	0	0	0	0	0	318.10	0	0	0	0.0677
0.4	0	0	423.85	0	0	0	0	0	424.23	0	0	0	0.0902
0.5	0	0	529.81	0	0	0	0	0	530.41	0	0	0	0.1126
0.6	0	0	635.78	0	0	0	0	0	636.63	0	0	0	0.1349
0.7	0	0	741.74	0	0	0	0	0	742.90	0	0	0	0.1571
0.8	0	0	847.70	0	0	0	0	0	849.22	0	0	0	0.1793
0.9	0	0	953.66	0	0	0	0	0	955.59	0	0	0	0.2014
1	0	0	1059.6	0	0	0	0	0	1062.0	0	0	0	0.2260

Table A - 18. Complete results of the first comparison for translation for $L = 60mm$: X – Rotation.

X Rotation (rad)	Approximation Matrix						Numerical Validation Model						Error (%)
	ΣFx	ΣFy	ΣFz	ΣMx	ΣMy	ΣMz	ΣFx	ΣFy	ΣFz	ΣMx	ΣMy	ΣMz	
0.005	0	0	0	2207.6	0	0	0	-0.0272	1.5295	2211.9	0	0	0.1964
0.01	0	0	0	4415.1	0	0	0	-0.0884	6.1176	4435.4	0	0	0.4598
0.02	0	0	0	8830.2	0	0	0	-0.1907	24.467	8933.5	0	0	1.1699
0.03	0	0	0	13245	0	0	0	-0.0627	55.035	13527	0	0	2.1311
0.04	0	0	0	17660	0	0	0	0.5383	97.802	18249	0	0	3.3374
0.05	0	0	0	22076	0	0	0	1.8539	152.74	23132	0	0	4.7841

Table A - 19. Complete results of the first comparison for translation for $L = 60mm$: Y – Rotation.

Y Rotation (rad)	Approximation Matrix						Numerical Validation Model						Error (%)
	ΣFx	ΣFy	ΣFz	ΣMx	ΣMy	ΣMz	ΣFx	ΣFy	ΣFz	ΣMx	ΣMy	ΣMz	
0.005	0	0	0	0	2207.6	0	-0.0051	0.0323	1.5295	-3.6854	2208.3	-0.0228	0.0295
0.01	0	0	0	0	4415.1	0	-0.0408	0.1292	6.1176	-14.739	4420.7	-0.1825	0.1261
0.02	0	0	0	0	8830.2	0	-0.3263	0.5165	24.466	-58.91	8874.7	-1.4588	0.5035
0.03	0	0	0	0	13245	0	-1.1008	1.1613	55.033	-132.38	13395	-4.9182	1.1344
0.04	0	0	0	0	17660	0	-2.6076	2.0625	97.798	-234.91	18016	-11.64	2.0136
0.05	0	0	0	0	22076	0	-5.0888	3.2182	152.73	-366.2	22769	-22.692	3.1378

Table A - 20. Complete results of the first comparison for translation for $L = 60mm$: Z – Rotation.

Z Rotation (rad)	Approximation Matrix						Numerical Validation Model						Error (%)
	ΣFx	ΣFy	ΣFz	ΣMx	ΣMy	ΣMz	ΣFx	ΣFy	ΣFz	ΣMx	ΣMy	ΣMz	
0.005	0	0	0	0	0	584.89	0	0	0.2795	0	0	584.91	0.0033
0.01	0	0	0	0	0	1169.8	0	0	1.118	0	0	1169.9	0.0113
0.02	0	0	0	0	0	2339.6	0	0	4.4719	0	0	2340.9	0.051
0.03	0	0	0	0	0	3509.3	0	0	10.061	0	0	3513.5	0.1199
0.04	0	0	0	0	0	4679.1	0	0	17.884	0	0	4689	0.2116
0.05	0	0	0	0	0	5848.9	0	0	27.939	0	0	5868.2	0.3300

Table A - 21 to Table A - 26 are the full results for the second comparison between the approximation matrix and the numerical validation model from Chapter 5.2.3 with the variables below:

$$b = 50\ mm$$
$$L = 50mm$$
$$\theta_L = \ 60\ ° Vs. 70\ °$$
$$k = 200\ N/mm$$

However, the results when $\theta_L = \ 70\ °$ have been shown from Table A - 9 to Table A - 14, hence, will not be shown again.

Table A - 21. Complete results of the second comparison for translation for $\theta_L = 60\ °$: X – Translation.

X Translation (mm)	Approximation Matrix						Numerical Validation Model						Error (%)
	ΣFx	ΣFy	ΣFz	ΣMx	ΣMy	ΣMz	ΣFx	ΣFy	ΣFz	ΣMx	ΣMy	ΣMz	
0.1	15	0	0	0	0	0	15.000	0	0.0768	0.6654	-0.0182	-0.0011	0.0008
0.2	30	0	0	0	0	0	30.001	0	0.3074	2.6617	-0.1454	-0.0085	0.0033
0.3	45	0	0	0	0	0	45.003	0	0.6916	5.9885	-0.4909	-0.0286	0.0074
0.4	60	0	0	0	0	0	60.008	0	1.2294	10.646	-1.1635	-0.067	0.0132
0.5	75	0	0	0	0	0	75.015	0	1.921	16.632	-2.2725	-0.1326	0.0206
0.6	90	0	0	0	0	0	90.027	0	2.7662	23.948	-3.9269	-0.229	0.0296
0.7	105	0	0	0	0	0	105.04	0	3.7651	32.593	-6.2358	-0.3637	0.0403
0.8	120	0	0	0	0	0	120.06	0	4.9176	42.564	-9.308	-0.5428	0.0526
0.9	135	0	0	0	0	0	135.09	0	6.223	53.862	-13.253	-0.7728	0.066
1	150	0	0	0	0	0	150.1	0	7.6838	66.48	-18.18	-1.06	0.0822

Table A - 22. Complete results of the second comparison for translation for $\theta_L = 60$ °: Y – Translation.

Y Translation (mm)	Approximation Matrix						Numerical Validation Model						Error (%)
	ΣFx	ΣFy	ΣFz	ΣMx	ΣMy	ΣMz	ΣFx	ΣFy	ΣFz	ΣMx	ΣMy	ΣMz	
0.1	0	15	0	0	0	0	0	15.001	0.0768	-0.6473	0	0	0.0008
0.2	0	30	0	0	0	0	0	30.001	0.3074	-2.5162	0	0	0.0033
0.3	0	45	0	0	0	0	0	45.003	0.6916	-5.4976	0	0	0.0074
0.4	0	60	0	0	0	0	0	60.008	1.2294	-9.4817	0	0	0.0131
0.5	0	75	0	0	0	0	0	75.015	1.921	-14.359	0	0	0.0206
0.6	0	90	0	0	0	0	0	90.027	2.7662	-20.02	0	0	0.0296
0.7	0	105	0	0	0	0	0	105.04	3.7651	-26.354	0	0	0.0403
0.8	0	120	0	0	0	0	0	120.06	4.9176	-33.251	0	0	0.0526
0.9	0	135	0	0	0	0	0	135.09	6.2239	-40.6	0	0	0.0666
1	0	150	0	0	0	0	0	150.12	7.6838	-48.292	0	0	0.0822

Table A - 23. Complete results of the second comparison for translation for $\theta_L = 60\ °$: Z – Translation.

Z Translation (mm)	Approximation Matrix						Numerical Validation Model						Error (%)
	ΣFx	ΣFy	ΣFz	ΣMx	ΣMy	ΣMz	ΣFx	ΣFy	ΣFz	ΣMx	ΣMy	ΣMz	
0.1	0	0	90	0	0	0	0	0	90.092	0	0	0	0.1022
0.2	0	0	180	0	0	0	0	0	180.37	0	0	0	0.2039
0.3	0	0	270	0	0	0	0	0	270.82	0	0	0	0.3051
0.4	0	0	360	0	0	0	0	0	361.46	0	0	0	0.4057
0.5	0	0	450	0	0	0	0	0	452.28	0	0	0	0.5059
0.6	0	0	540	0	0	0	0	0	543.27	0	0	0	0.6056
0.7	0	0	630	0	0	0	0	0	634.44	0	0	0	0.7048
0.8	0	0	720	0	0	0	0	0	725.79	0	0	0	0.8035
0.9	0	0	810	0	0	0	0	0	817.3	0	0	0	0.9017
1	0	0	900	0	0	0	0	0	909.0	0	0	0	0.9994

Table A - 24. Complete results of the second comparison for translation for $\theta_L = 60\ °$: X – Rotation.

X Rotation (rad)	Approximation Matrix						Numerical Validation Model						Error (%)
	ΣFx	ΣFy	ΣFz	ΣMx	ΣMy	ΣMz	ΣFx	ΣFy	ΣFz	ΣMx	ΣMy	ΣMz	
0.005	0	0	0	1875	0	0	0	-0.0917	1.649	1884.4	0	0	0.4844
0.01	0	0	0	3750	0	0	0	-0.3295	6.5966	3789.8	0	0	1.0604
0.02	0	0	0	7500	0	0	0	-1.0202	26.386	7686.3	0	0	2.4844
0.03	0	0	0	11250	0	0	0	-1.6272	59.35	11730	0	0	4.2656
0.04	0	0	0	15000	0	0	0	-1.7088	105.45	15960	0	0	6.3972
0.05	0	0	0	18750	0	0	0	-0.8279	164.62	20413	0	0	8.872

Table A - 25. Complete results of the second comparison for translation for $\theta_L = 60\ °$: Y – Rotation.

Y Rotation (rad)	Approximation Matrix						Numerical Validation Model						Error (%)
	ΣFx	ΣFy	ΣFz	ΣMx	ΣMy	ΣMz	ΣFx	ΣFy	ΣFz	ΣMx	ΣMy	ΣMz	
0.005	0	0	0	0	1875	0	-0.0093	0.101	1.6487	-8.2174	1875.9	-0.0648	0.0462
0.01	0	0	0	0	3750	0	-0.0745	0.4039	6.5941	-32.857	3757	-0.5179	0.1847
0.02	0	0	0	0	7500	0	-0.5961	1.6144	26.365	-131.22	7555.4	-4.1393	0.7384
0.03	0	0	0	0	11250	0	-2.01	3.6276	59.281	-294.47	11437	-13.949	1.6601
0.04	0	0	0	0	15000	0	-4.758	6.4374	105.29	-521.59	15442	-32.992	2.9484
0.05	0	0	0	0	18750	0	-9.2807	10.035	164.3	-811.16	1961	-64.259	4.6011

Table A - 26. Complete results of the second comparison for translation for $\theta_L = 60\ °$: Z – Rotation.

Z Rotation (rad)	Approximation Matrix						Numerical Validation Model						Error (%)
	ΣFx	ΣFy	ΣFz	ΣMx	ΣMy	ΣMz	ΣFx	ΣFy	ΣFz	ΣMx	ΣMy	ΣMz	
0.005	0	0	0	0	0	1250	0	0	0.5077	0	0	1250.1	0.0069
0.01	0	0	0	0	0	2500	0	0	2.0306	0	0	2500.7	0.0277
0.02	0	0	0	0	0	5000	0	0	8.1219	0	0	5005.5	0.1106
0.03	0	0	0	0	0	7500	0	0	18.272	0	0	7518.7	0.249
0.04	0	0	0	0	0	10000	0	0	32.478	0	0	10044	0.4428
0.05	0	0	0	0	0	12500	0	0	50.737	0	0	12586	0.6921

Table A - 27 to Table A - 50 are the results for the sensitivity analysis from Chapter 5.3 with the variables below.

$$b = 50\ mm$$

$$\theta_L = 70\ °$$

$$k = 200\ N/mm$$

$$L_{Approx.} = 50\ mm$$

$$L_{Num.Val.} = 47\ mm, 49\ mm, 51\ mm\ \&\ 53\ mm$$

Table A - 27. Complete results of the sensitivity analysis for L= 47 mm: X – Translation.

X Translation (mm)	Approximation Matrix						Numerical Validation Model						Error (%)
	ΣFx	ΣFy	ΣFz	ΣMx	ΣMy	ΣMz	ΣFx	ΣFy	ΣFz	ΣMx	ΣMy	ΣMz	
0.1	7.0187	0	0	0	0	0	7.0187	0	0.05	0.1536	21.048	0	0
0.2	14.037	0	0	0	0	0	14.038	0	0.2	0.6143	42.05	-0.0011	0.0029
0.3	21.056	0	0	0	0	0	21.057	0	0.45	1.3821	62.96	-0.0038	0.0062
0.4	28.075	0	0	0	0	0	28.078	0	0.8	2.4571	83.73	-0.0091	0.0107
0.5	35.093	0	0	0	0	0	35.1	0	1.2499	3.8391	104.32	-0.0177	0.0168
0.6	42.112	0	0	0	0	0	42.122	0	1.7999	5.5282	124.67	-0.0306	0.024
0.7	49.131	0	0	0	0	0	49.147	0	2.4498	7.5242	144.74	-0.0485	0.0326
0.8	56.149	0	0	0	0	0	56.173	0	3.1997	9.8272	164.5	-0.0724	0.0427
0.9	63.168	0	0	0	0	0	63.202	0	4.0496	12.437	183.88	-0.1031	0.054
1	70.187	0	0	0	0	0	70.234	0	4.9995	15.354	202.84	-0.1415	0.0667

Table A - 28. Complete results of the sensitivity analysis for L= 47 mm: Y – Translation.

Y Translation (mm)	Approximation Matrix						Numerical Validation Model						Error (%)
	ΣFx	ΣFy	ΣFz	ΣMx	ΣMy	ΣMz	ΣFx	ΣFy	ΣFz	ΣMx	ΣMy	ΣMz	
0.1	0	7.0187	0	0	0	0	0	7.0187	0.05	-21.202	0	0	0
0.2	0	14.037	0	0	0	0	0	14.038	0.2	-42.665	0	0	0.0029
0.3	0	21.056	0	0	0	0	0	21.057	0.45	-64.342	0	0	0.0062
0.4	0	28.075	0	0	0	0	0	28.078	0.8	-86.187	0	0	0.0107
0.5	0	35.093	0	0	0	0	0	35.099	1.2499	-108.15	0	0	0.0168
0.6	0	42.112	0	0	0	0	0	42.122	1.7999	-130.2	0	0	0.024
0.7	0	49.131	0	0	0	0	0	49.147	2.4498	-152.27	0	0	0.0326
0.8	0	56.149	0	0	0	0	0	56.173	3.1997	-174.32	0	0	0.0427
0.9	0	63.168	0	0	0	0	0	63.202	4.0496	-196.31	0	0	0.0534
1	0	70.187	0	0	0	0	0	70.234	4.9995	-218.19	0	0	0.0667

Table A - 29. Complete results of the sensitivity analysis for L= 47 mm: Z – Translation.

Z Translation (mm)	Approximation Matrix						Numerical Validation Model						Error (%)
	ΣFx	ΣFy	ΣFz	ΣMx	ΣMy	ΣMz	ΣFx	ΣFy	ΣFz	ΣMx	ΣMy	ΣMz	
0.1	0	0	105.96	0	0	0	0	0	105.98	0	0	0	0.02
0.2	0	0	211.93	0	0	0	0	0	212.01	0	0	0	0.04
0.3	0	0	317.89	0	0	0	0	0	318.08	0	0	0	0.06
0.4	0	0	423.85	0	0	0	0	0	424.19	0	0	0	0.0799
0.5	0	0	529.81	0	0	0	0	0	530.34	0	0	0	0.0998
0.6	0	0	635.78	0	0	0	0	0	636.54	0	0	0	0.1196
0.7	0	0	741.74	0	0	0	0	0	742.77	0	0	0	0.1393
0.8	0	0	847.7	0	0	0	0	0	849.05	0	0	0	0.159
0.9	0	0	953.66	0	0	0	0	0	955.37	0	0	0	0.1787
1	0	0	1059.6	0	0	0	0	0	1061.7	0	0	0	0.1982

Table A - 30. Complete results of the sensitivity analysis for L= 47 mm: X – Rotation.

X Rotation (rad)	Approximation Matrix						Numerical Validation Model						Error (%)
	ΣFx	ΣFy	ΣFz	ΣMx	ΣMy	ΣMz	ΣFx	ΣFy	ΣFz	ΣMx	ΣMy	ΣMz	
0.005	0	0	0	2207.6	0	0	0	-1.0754	1.0513	2213.9	0	0	0.2854
0.01	0	0	0	4415.1	0	0	0	-2.187	4.205	4435.3	0	0	0.4579
0.02	0	0	0	8830.2	0	0	0	-4.4651	16.818	8907.5	0	0	0.8754
0.03	0	0	0	13245	0	0	0	-6.7266	37.833	13430	0	0	1.3977
0.04	0	0	0	17660	0	0	0	-8.8645	67.242	18016	0	0	2.0192
0.05	0	0	0	22076	0	0	0	-10.772	105.03	22680	0	0	2.737

Table A - 31. Complete results of the sensitivity analysis for $L = 47mm$: Y – Rotation.

Y Rotation (rad)	Approximation Matrix						Numerical Validation Model						Error (%)
	ΣFx	ΣFy	ΣFz	ΣMx	ΣMy	ΣMz	ΣFx	ΣFy	ΣFz	ΣMx	ΣMy	ΣMz	
0.005	0	0	0	0	2207.6	0	1.0506	0.0249	1.0513	-2.9004	2211	-0.0119	0.154
0.01	0	0	0	0	4415.1	0	2.0876	0.0994	4.2051	-11.6	4423.7	-0.0951	0.1952
0.02	0	0	0	0	8830.2	0	4.0673	0.3975	16.819	-46.377	8861.2	-0.7603	0.3507
0.03	0	0	0	0	13245	0	5.8313	0.8941	37.836	-104.26	13326	-2.5642	0.612
0.04	0	0	0	0	17660	0	7.272	1.5887	67.249	-185.12	17832	-6.0727	0.9745
0.05	0	0	0	0	22076	0	8.2821	2.4807	105.05	-288.81	22393	-11.847	1.4357

Table A - 32. Complete results of the sensitivity analysis for L= 47 mm: Z – Rotation.

Z Rotation (rad)	Approximation Matrix						Numerical Validation Model						Error (%)
	ΣFx	ΣFy	ΣFz	ΣMx	ΣMy	ΣMz	ΣFx	ΣFy	ΣFz	ΣMx	ΣMy	ΣMz	
0.005	0	0	0	0	0	584.89	0	0	0.2199	0	0	584.9	0.0014
0.01	0	0	0	0	0	1169.8	0	0	0.8797	0	0	1169.8	0.0037
0.02	0	0	0	0	0	2339.6	0	0	3.5188	0	0	2340.1	0.0205
0.03	0	0	0	0	0	3509.3	0	0	7.9168	0	0	3511.1	0.0513
0.04	0	0	0	0	0	4679.1	0	0	14.073	0	0	4683.3	0.0898
0.05	0	0	0	0	0	5848.9	0	0	21.987	0	0	5857.1	0.1397

Table A - 33. Complete results of the sensitivity analysis for L= 49 mm: X – Translation.

X Translation (mm)	Approximation Matrix						Numerical Validation Model						Error (%)
	ΣFx	ΣFy	ΣFz	ΣMx	ΣMy	ΣMz	ΣFx	ΣFy	ΣFz	ΣMx	ΣMy	ΣMz	
0.1	7.0187	0	0	0	0	0	7.0187	0	0.05	0.1536	7.0109	0	0
0.2	14.037	0	0	0	0	0	14.038	0	0.2	0.6143	13.975	-0.0011	0.0029
0.3	21.056	0	0	0	0	0	21.057	0	0.45	1.3821	20.845	-0.0038	0.0062
0.4	28.075	0	0	0	0	0	28.078	0	0.8	2.4571	27.575	-0.0091	0.0107
0.5	35.093	0	0	0	0	0	35.1	0	1.2499	3.8391	34.117	-0.0177	0.0168
0.6	42.112	0	0	0	0	0	42.122	0	1.7999	5.5282	40.424	-0.0306	0.024
0.7	49.131	0	0	0	0	0	49.147	0	2.4498	7.5242	46.451	-0.0485	0.0326
0.8	56.149	0	0	0	0	0	56.173	0	3.1997	9.8272	52.149	-0.0724	0.0427
0.9	63.168	0	0	0	0	0	63.202	0	4.0496	12.437	57.472	-0.1031	0.054
1	70.187	0	0	0	0	0	70.234	0	4.9995	15.354	62.373	-0.1415	0.0667

Table A - 34. Complete results of the sensitivity analysis for L= 49 mm: Y – Translation.

Y Translation (mm)	Approximation Matrix						Numerical Validation Model						Error (%)
	ΣFx	ΣFy	ΣFz	ΣMx	ΣMy	ΣMz	ΣFx	ΣFy	ΣFz	ΣMx	ΣMy	ΣMz	
0.1	0	7.0187	0	0	0	0	0	7.0187	0.05	-7.1644	0	0	0
0.2	0	14.037	0	0	0	0	0	14.038	0.2	-14.589	0	0	0.0029
0.3	0	21.056	0	0	0	0	0	21.057	0.45	-22.227	0	0	0.0062
0.4	0	28.075	0	0	0	0	0	28.078	0.8	-30.032	0	0	0.0107
0.5	0	35.093	0	0	0	0	0	35.099	1.2499	-37.956	0	0	0.0168
0.6	0	42.112	0	0	0	0	0	42.122	1.7999	-45.952	0	0	0.024
0.7	0	49.131	0	0	0	0	0	49.147	2.4498	-53.975	0	0	0.0326
0.8	0	56.149	0	0	0	0	0	56.173	3.1997	-61.976	0	0	0.0427
0.9	0	63.168	0	0	0	0	0	63.202	4.0496	-69.909	0	0	0.0534
1	0	70.187	0	0	0	0	0	70.234	4.9995	-77.726	0	0	0.0667

Table A - 35. Complete results of the sensitivity analysis for L= 49 mm: Z – Translation.

Z Translation (mm)	Approximation Matrix						Numerical Validation Model						Error (%)
	ΣFx	ΣFy	ΣFz	ΣMx	ΣMy	ΣMz	ΣFx	ΣFy	ΣFz	ΣMx	ΣMy	ΣMz	
0.1	0	0	105.96	0	0	0	0	0	105.98	0	0	0	0.02
0.2	0	0	211.93	0	0	0	0	0	212.01	0	0	0	0.04
0.3	0	0	317.89	0	0	0	0	0	318.08	0	0	0	0.06
0.4	0	0	423.85	0	0	0	0	0	424.19	0	0	0	0.0799
0.5	0	0	529.81	0	0	0	0	0	530.34	0	0	0	0.0998
0.6	0	0	635.78	0	0	0	0	0	636.54	0	0	0	0.1196
0.7	0	0	741.74	0	0	0	0	0	742.77	0	0	0	0.1393
0.8	0	0	847.7	0	0	0	0	0	849.05	0	0	0	0.159
0.9	0	0	953.66	0	0	0	0	0	955.37	0	0	0	0.1787
1	0	0	1059.6	0	0	0	0	0	1061.7	0	0	0	0.1982

Table A - 36. Complete results of the sensitivity analysis for L= 49 mm: X – Rotation.

X Rotation (rad)	Approximation Matrix						Numerical Validation Model						Error (%)
	ΣFx	ΣFy	ΣFz	ΣMx	ΣMy	ΣMz	ΣFx	ΣFy	ΣFz	ΣMx	ΣMy	ΣMz	
0.005	0	0	0	2207.6	0	0	0	-0.3748	1.1051	2211	0	0	0.1531
0.01	0	0	0	4415.1	0	0	0	-0.7875	4.4203	4429.4	0	0	0.3241
0.02	0	0	0	8830.2	0	0	0	-1.6664	17.679	8896.4	0	0	0.7498
0.03	0	0	0	13245	0	0	0	-2.5176	39.771	13416.5	0	0	1.2948
0.04	0	0	0	17660	0	0	0	-3.2219	70.687	18005.	0	0	1.9537
0.05	0	0	0	22076	0	0	0	-3.661	110.41	22677	0	0	2.7233

Table A - 37. Complete results of the sensitivity analysis for L= 49 mm: Y – Rotation.

Y Rotation (rad)	Approximation Matrix						Numerical Validation Model						Error (%)
	ΣFx	ΣFy	ΣFz	ΣMx	ΣMy	ΣMz	ΣFx	ΣFy	ΣFz	ΣMx	ΣMy	ΣMz	
0.005	0	0	0	2207.6	0	0	0.3484	0.0264	1.1051	-2.7467	2208.2	-0.0133	0.0287
0.01	0	0	0	4415.1	0	0	0.6819	0.1056	4.4203	-10.985	4418.4	-0.1061	0.0753
0.02	0	0	0	8830.2	0	0	1.2441	0.4221	17.679	-43.918	8852.5	-0.8487	0.2529
0.03	0	0	0	13245	0	0	1.5671	0.9492	39.772	-98.725	13318	-2.8624	0.5509
0.04	0	0	0	17660	0	0	1.5315	1.6865	70.688	-175.29	17830	-6.7783	0.9648
0.05	0	0	0	22076	0	0	1.0185	2.6331	110.42	-273.44	22405	-13.223	1.4918

Table A - 38. Complete results of the sensitivity analysis for L= 49 mm: Z – Rotation.

Z Rotation (rad)	Approximation Matrix						Numerical Validation Model						Error (%)
	ΣFx	ΣFy	ΣFz	ΣMx	ΣMy	ΣMz	ΣFx	ΣFy	ΣFz	ΣMx	ΣMy	ΣMz	
0.005	0	0	0	0	0	584.89	0	0	0.2199	0	0	584.9	0.0014
0.01	0	0	0	0	0	1169.8	0	0	0.8797	0	0	1169.8	0.0037
0.02	0	0	0	0	0	2339.6	0	0	3.5188	0	0	2340.1	0.0205
0.03	0	0	0	0	0	3509.3	0	0	7.9168	0	0	3511.1	0.0513
0.04	0	0	0	0	0	4679.1	0	0	14.073	0	0	4683.3	0.0898
0.05	0	0	0	0	0	5848.9	0	0	21.987	0	0	5857.1	0.1397

Table A - 39. Complete results of the sensitivity analysis for L= 51 mm: X – Translation.

X Translation (mm)	Approximation Matrix						Numerical Validation Model						Error (%)
	ΣFx	ΣFy	ΣFz	ΣMx	ΣMy	ΣMz	ΣFx	ΣFy	ΣFz	ΣMx	ΣMy	ΣMz	
0.1	7.0187	0	0	0	0	0	7.0187	0	0.05	0.1536	-7.0266	0	0
0.2	14.037	0	0	0	0	0	14.038	0	0.2	0.6143	-14.101	-0.0011	0.0029
0.3	21.056	0	0	0	0	0	21.057	0	0.45	1.3821	-21.27	-0.0038	0.0062
0.4	28.075	0	0	0	0	0	28.078	0	0.8	2.4571	-28.581	-0.0091	0.0107
0.5	35.093	0	0	0	0	0	35.1	0	1.2499	3.8391	-36.082	-0.0177	0.0168
0.6	42.112	0	0	0	0	0	42.122	0	1.7999	5.5282	-43.82	-0.0306	0.024
0.7	49.131	0	0	0	0	0	49.147	0	2.4498	7.5242	-51.843	-0.0485	0.0326
0.8	56.149	0	0	0	0	0	56.173	0	3.1997	9.8272	-60.198	-0.0724	0.0427
0.9	63.168	0	0	0	0	0	63.202	0	4.0496	12.437	-68.933	-0.1031	0.054
1	70.187	0	0	0	0	0	70.234	0	4.9995	15.354	-78.094	-0.1415	0.0667

Table A - 40. Complete results of the sensitivity analysis for L= 51 mm: Y – Translation.

Y Translation (mm)	Approximation Matrix						Numerical Validation Model						Error (%)
	ΣFx	ΣFy	ΣFz	ΣMx	ΣMy	ΣMz	ΣFx	ΣFy	ΣFz	ΣMx	ΣMy	ΣMz	
0.1	0	7.0187	0	0	0	0	0	7.0187	0.05	6.873	0	0	0
0.2	0	14.037	0	0	0	0	0	14.038	0.2	13.486	0	0	0.0029
0.3	0	21.056	0	0	0	0	0	21.057	0.45	19.887	0	0	0.0062
0.4	0	28.075	0	0	0	0	0	28.078	0.8	26.124	0	0	0.0107
0.5	0	35.093	0	0	0	0	0	35.099	1.2499	32.243	0	0	0.0168
0.6	0	42.112	0	0	0	0	0	42.122	1.7999	38.292	0	0	0.024
0.7	0	49.131	0	0	0	0	0	49.147	2.4498	44.319	0	0	0.0326
0.8	0	56.149	0	0	0	0	0	56.173	3.1997	50.371	0	0	0.0427
0.9	0	63.168	0	0	0	0	0	63.202	4.0496	56.496	0	0	0.0534
1	0	70.187	0	0	0	0	0	70.234	4.9995	62.741	0	0	0.0667

Table A - 41. Complete results of the sensitivity analysis for L= 51 mm: Z – Translation.

Z Translation (mm)	Approximation Matrix						Numerical Validation Model						Error (%)
	ΣFx	ΣFy	ΣFz	ΣMx	ΣMy	ΣMz	ΣFx	ΣFy	ΣFz	ΣMx	ΣMy	ΣMz	
0.1	0	0	105.96	0	0	0	0	0	105.98	0	0	0	0.02
0.2	0	0	211.93	0	0	0	0	0	212.01	0	0	0	0.04
0.3	0	0	317.89	0	0	0	0	0	318.08	0	0	0	0.06
0.4	0	0	423.85	0	0	0	0	0	424.19	0	0	0	0.0799
0.5	0	0	529.81	0	0	0	0	0	530.34	0	0	0	0.0998
0.6	0	0	635.78	0	0	0	0	0	636.54	0	0	0	0.1196
0.7	0	0	741.74	0	0	0	0	0	742.77	0	0	0	0.1393
0.8	0	0	847.7	0	0	0	0	0	849.05	0	0	0	0.159
0.9	0	0	953.66	0	0	0	0	0	955.37	0	0	0	0.1787
1	0	0	1059.6	0	0	0	0	0	1061.7	0	0	0	0.1982

Table A - 42. Complete results of the sensitivity analysis for L= 51 mm: X – Rotation.

X Rotation (rad)	Approximation Matrix						Numerical Validation Model						Error (%)
	ΣFx	ΣFy	ΣFz	ΣMx	ΣMy	ΣMz	ΣFx	ΣFy	ΣFz	ΣMx	ΣMy	ΣMz	
0.005	0	0	0	2207.6	0	0	0	0.3258	1.1599	2210.9	0	0	0.1477
0.01	0	0	0	4415.1	0	0	0	0.6122	4.6396	4429.1	0	0	0.3172
0.02	0	0	0	8830.2	0	0	0	1.1331	18.557	8896.6	0	0	0.7519
0.03	0	0	0	13245	0	0	0	1.6944	41.746	13420	0	0	1.3216
0.04	0	0	0	17660	0	0	0	2.4277	74.197	18017	0	0	2.0209
0.05	0	0	0	22076	0	0	0	3.4637	115.9	22704	0	0	2.8466

Table A - 43. Complete results of the sensitivity analysis for L= 51 mm: Y – Rotation.

Y Rotation (rad)	Approximation Matrix						Numerical Validation Model						Error (%)
	ΣFx	ΣFy	ΣFz	ΣMx	ΣMy	ΣMz	ΣFx	ΣFy	ΣFz	ΣMx	ΣMy	ΣMz	
0.005	0	0	0	0	2207.6	0	-0.3537	0.0279	1.1599	-2.5838	2208.5	-0.0147	0.0307
0.01	0	0	0	0	4415.1	0	-0.7239	0.1117	4.6395	-10.334	4418.8	-0.1175	0.0832
0.02	0	0	0	0	8830.2	0	-1.5799	0.4466	18.556	-41.311	8855.3	-0.9397	0.2845
0.03	0	0	0	0	13245	0	-2.7	1.0044	41.743	-92.861	13327	-3.1691	0.622
0.04	0	0	0	0	17660	0	-4.2158	1.7843	74.191	-164.87	17853	-7.5041	1.0911
0.05	0	0	0	0	22076	0	-6.2585	2.7854	115.89	-257.17	22449	-14.637	1.6889

Table A - 44. Complete results of the sensitivity analysis for L= 51 mm: Z – Rotation.

Z Rotation (rad)	Approximation Matrix						Numerical Validation Model						Error (%)
	ΣFx	ΣFy	ΣFz	ΣMx	ΣMy	ΣMz	ΣFx	ΣFy	ΣFz	ΣMx	ΣMy	ΣMz	
0.005	0	0	0	0	0	584.89	0	0	0.2199	0	0	584.9	0.0014
0.01	0	0	0	0	0	1169.8	0	0	0.8797	0	0	1169.8	0.0037
0.02	0	0	0	0	0	2339.6	0	0	3.5188	0	0	2340.1	0.0205
0.03	0	0	0	0	0	3509.3	0	0	7.9168	0	0	3511.1	0.0513
0.04	0	0	0	0	0	4679.1	0	0	14.073	0	0	4683.3	0.0898
0.05	0	0	0	0	0	5848.9	0	0	21.987	0	0	5857.1	0.1397

Table A - 45. Complete results of the sensitivity analysis for L= 53 mm: X – Translation.

X Translation (mm)	Approximation Matrix						Numerical Validation Model						Error (%)
	ΣFx	ΣFy	ΣFz	ΣMx	ΣMy	ΣMz	ΣFx	ΣFy	ΣFz	ΣMx	ΣMy	ΣMz	
0.1	7.0187	0	0	0	0	0	7.0187	0	0.05	0.1536	-21.064	0	0
0.2	14.037	0	0	0	0	0	14.038	0	0.2	0.6143	-42.176	-0.0011	0.0029
0.3	21.056	0	0	0	0	0	21.057	0	0.45	1.3821	-63.384	-0.0038	0.0062
0.4	28.075	0	0	0	0	0	28.078	0	0.8	2.4571	-84.736	-0.0091	0.0107
0.5	35.093	0	0	0	0	0	35.1	0	1.2499	3.8391	-106.28	-0.0177	0.0168
0.6	42.112	0	0	0	0	0	42.122	0	1.7999	5.5282	-128.06	-0.0306	0.024
0.7	49.131	0	0	0	0	0	49.147	0	2.4498	7.5242	-150.14	-0.0485	0.0326
0.8	56.149	0	0	0	0	0	56.173	0	3.1997	9.8272	-172.55	-0.0724	0.0427
0.9	63.168	0	0	0	0	0	63.202	0	4.0496	12.437	-195.34	-0.1031	0.054
1	70.187	0	0	0	0	0	70.234	0	4.9995	15.354	-218.56	-0.1415	0.0667

Table A - 46. Complete results of the sensitivity analysis for L= 53 mm: Y – Translation.

Y Translation (mm)	Approximation Matrix						Numerical Validation Model						Error (%)
	ΣFx	ΣFy	ΣFz	ΣMx	ΣMy	ΣMz	ΣFx	ΣFy	ΣFz	ΣMx	ΣMy	ΣMz	
0.1	0	7.0187	0	0	0	0	0	7.0187	0.05	20.91	0	0	0
0.2	0	14.037	0	0	0	0	0	14.038	0.2	41.562	0	0	0.0029
0.3	0	21.056	0	0	0	0	0	21.057	0.45	62.002	0	0	0.0062
0.4	0	28.075	0	0	0	0	0	28.078	0.8	82.279	0	0	0.0107
0.5	0	35.093	0	0	0	0	0	35.099	1.2499	102.44	0	0	0.0168
0.6	0	42.112	0	0	0	0	0	42.122	1.7999	122.54	0	0	0.024
0.7	0	49.131	0	0	0	0	0	49.147	2.4498	142.61	0	0	0.0326
0.8	0	56.149	0	0	0	0	0	56.173	3.1997	162.72	0	0	0.0427
0.9	0	63.168	0	0	0	0	0	63.202	4.0496	182.9	0	0	0.0534
1	0	70.187	0	0	0	0	0	70.234	4.9995	203.21	0	0	0.0667

Table A - 47. Complete results of the sensitivity analysis for L= 53 mm: Z – Translation.

Z Translation (mm)	Approximation Matrix						Numerical Validation Model						Error (%)
	ΣFx	ΣFy	ΣFz	ΣMx	ΣMy	ΣMz	ΣFx	ΣFy	ΣFz	ΣMx	ΣMy	ΣMz	
0.1	0	0	105.96	0	0	0	0	0	105.98	0	0	0	0.02
0.2	0	0	211.93	0	0	0	0	0	212.01	0	0	0	0.04
0.3	0	0	317.89	0	0	0	0	0	318.08	0	0	0	0.06
0.4	0	0	423.85	0	0	0	0	0	424.19	0	0	0	0.0799
0.5	0	0	529.81	0	0	0	0	0	530.34	0	0	0	0.0998
0.6	0	0	635.78	0	0	0	0	0	636.54	0	0	0	0.1196
0.7	0	0	741.74	0	0	0	0	0	742.77	0	0	0	0.1393
0.8	0	0	847.7	0	0	0	0	0	849.05	0	0	0	0.159
0.9	0	0	953.66	0	0	0	0	0	955.37	0	0	0	0.1787
1	0	0	1059.6	0	0	0	0	0	1061.7	0	0	0	0.1982

Table A - 48. Complete results of the sensitivity analysis for L= 53 mm: X – Rotation.

X Rotation (rad)	Approximation Matrix						Numerical Validation Model						Error (%)
	ΣFx	ΣFy	ΣFz	ΣMx	ΣMy	ΣMz	ΣFx	ΣFy	ΣFz	ΣMx	ΣMy	ΣMz	
0.005	0	0	0	2207.6	0	0	0	1.0264	1.2157	2213.5	0	0	0.2692
0.01	0	0	0	4415.1	0	0	0	2.012	4.8629	4434.4	0	0	0.4373
0.02	0	0	0	8830.2	0	0	0	3.9334	19.45	8908.1	0	0	0.8818
0.03	0	0	0	13245	0	0	0	5.9094	43.756	13441	0	0	1.4783
0.04	0	0	0	17660	0	0	0	8.0843	77.77	18052	0	0	2.2213
0.05	0	0	0	22076	0	0	0	10.602	121.48	22762	0	0	3.1075

Table A - 49. Complete results of the sensitivity analysis for L= 53 mm: Y – Rotation.

Y Rotation (rad)	Approximation Matrix						Numerical Validation Model						Error (%)
	ΣFx	ΣFy	ΣFz	ΣMx	ΣMy	ΣMz	ΣFx	ΣFy	ΣFz	ΣMx	ΣMy	ΣMz	
0.005	0	0	0	0	2207.6	0	-1.0558	0.0295	1.2157	-2.4116	2211.1	-0.0162	0.16
0.01	0	0	0	0	4415.1	0	-2.1298	0.1178	4.8627	-9.6451	4424.8	-0.1292	0.2189
0.02	0	0	0	0	8830.2	0	-4.4048	0.4711	19.448	-38.557	8869.6	-1.0331	0.4456
0.03	0	0	0	0	13245	0	-6.9701	1.0595	43.751	-86.668	13354	-3.4842	0.8255
0.04	0	0	0	0	17660	0	-9.9702	1.882	77.758	-153.86	17899	-8.2497	1.3538
0.05	0	0	0	0	22076	0	-13.549	2.9376	121.45	-239.98	22524	-16.09	2.0278

Table A - 50. Complete results of the sensitivity analysis for L= 53 mm: Z – Rotation.

Z Rotation (rad)	Approximation Matrix						Numerical Validation Model						Error (%)
	ΣFx	ΣFy	ΣFz	ΣMx	ΣMy	ΣMz	ΣFx	ΣFy	ΣFz	ΣMx	ΣMy	ΣMz	
0.005	0	0	0	0	0	584.89	0	0	0.2199	0	0	584.9	0.0014
0.01	0	0	0	0	0	1169.8	0	0	0.8797	0	0	1169.8	0.0037
0.02	0	0	0	0	0	2339.6	0	0	3.5188	0	0	2340.1	0.0205
0.03	0	0	0	0	0	3509.3	0	0	7.9168	0	0	3511.1	0.0513
0.04	0	0	0	0	0	4679.1	0	0	14.073	0	0	4683.3	0.0898
0.05	0	0	0	0	0	5848.9	0	0	21.987	0	0	5857.1	0.1397

Table A - 51 to Table A - 56 are the results for Chapter 5.4, where forces and moments were applied and the translations and rotations of the peg were calculated using the approximation model and measured in Simscape simulation.

Approximation model parameters:

$$b = 43.3\ mm$$
$$L = 25\ mm$$
$$h = 50\ mm$$
$$\theta_L = 60\ °$$
$$K = 30\ N/mm$$
$$l_o = 57.7530\ m$$
$$q = 28.8675\ mm$$

Simscape parameters:

$$b = 43.3\ mm$$
$$L = 25\ mm$$
$$h = 30\ mm$$
$$T = 20\ mm$$
$$\theta_L = 60\ °$$
$$K = 30\ N/mm$$

Table A - 51. Full results of translations and rotations of pegs under the influence of forces on the X-axis.

Force (N)	Approximation Matrix						Simscape Model						Error (%)
	dx (mm)	dy (mm)	dz (mm)	Rx (Rad)	Ry (Rad)	Rz (Rad)	dx (mm)	dy (mm)	dz (mm)	Rx (Rad)	Ry (Rad)	Rz (Rad)	
-100	-4.444	0	0	0	0	0	-4.472	-0.001	-0.21	-0.005	0	0.0004	0.616
-70	-3.111	0	0	0	0	0	-3.121	0	-0.1	-0.002	0	0.0002	0.317
-50	-2.222	0	0	0	0	0	-2.226	0	-0.05	-0.001	0	0	0.170
-30	-1.333	0	0	0	0	0	-1.334	0	-0.02	0	0	0	0.05
-10	-0.444	0	0	0	0	0	-0.445	0	0	0	0	0	0.013
10	0.4444	0	0	0	0	0	0.4445	0	0	0	0	0	0.013
30	1.3332	0	0	0	0	0	1.334	0	-0.02	0	0	0	0.050
50	2.2222	0	0	0	0	0	2.226	0	-0.05	-0.001	0	0	0.167
70	3.1111	0	0	0	0	0	3.121	0	-0.1	-0.002	0	0	0.317
100	4.4444	0	0	0	0	0	4.472	-0.001	-0.21	-0.005	0	-0.001	0.616

Table A - 52. Full results of translations and rotations of pegs under the influence of forces on the Y-axis.

Force (N)	Approximation Matrix						Simscape Model						Error (%)
	dx (mm)	dy (mm)	dz (mm)	Rx (Rad)	Ry (Rad)	Rz (Rad)	dx (mm)	dy (mm)	dz (mm)	Rx (Rad)	Ry (Rad)	Rz (Rad)	
-100	0	-4.444	0	0	0	0	0	-4.475	-0.2	0.0049	0	0	0.683
-70	0	-3.111	0	0	0	0	0	-3.121	-0.1	0.0024	0	0	0.317
-50	0	-2.222	0	0	0	0	0	-2.226	-0.05	0.0012	0	0	0.170
-30	0	-1.333	0	0	0	0	0	-1.334	-0.02	0.0004	0	0	0.050
-10	0	-0.444	0	0	0	0	0	-0.445	0	0	0	0	0.013
10	0	0.4444	0	0	0	0	0	0.4445	0	0	0	0	0.013
30	0	1.3333	0	0	0	0	0	1.334	-0.02	0.0004	0	0	0.050
50	0	2.2222	0	0	0	0	0	2.225	-0.05	0.0012	0	0	0.125
70	0	3.1111	0	0	0	0	0	3.119	-0.11	0.0024	0	0	0.253
100	0	4.4444	0	0	0	0	0	4.467	-0.22	0.0048	0	0	0.505

Table A - 53. Full results of translations and rotations of pegs under the influence of forces on the Z-axis.

Force (N)	Approximation Matrix						Simscape Model						Error (%)
	dx (mm)	dy (mm)	dz (mm)	Rx (Rad)	Ry (Rad)	Rz (Rad)	dx (mm)	dy (mm)	dz (mm)	Rx (Rad)	Ry (Rad)	Rz (Rad)	
-100	0	0	-0.741	0	0	0	0	0	-0.75	0	0	0	1.184
-70	0	0	-0.519	0	0	0	0	0	-0.52	0	0	0	0.235
-50	0	0	-0.371	0	0	0	0	0	-0.37	0	0	0	0.150
-30	0	0	-0.222	0	0	0	0	0	-0.22	0	0	0	1.061
-10	0	0	-0.074	0	0	0	0	0	-0.07	0	0	0	5.873
10	0	0	0.0741	0	0	0	0	0	0.07	0	0	0	5.873
30	0	0	0.2223	0	0	0	0	0	0.22	0	0	0	1.061
50	0	0	0.3706	0	0	0	0	0	0.37	0	0	0	0.150
70	0	0	0.5188	0	0	0	0	0	0.52	0	0	0	0.235
100	0	0	0.7411	0	0	0	0	0	0.73	0	0	0	1.522

Table A - 54. Full results of translations and rotations of peg under the influence of moment about the X-axis.

Moment (Nmm)	Approximation Matrix						Simscape Model						Error (%)
	dx (mm)	dy (mm)	dz (mm)	Rx (Rad)	Ry (Rad)	Rz (Rad)	dx (mm)	dy (mm)	dz (mm)	Rx (Rad)	Ry (Rad)	Rz (Rad)	
-1000	0	0	0	-0.024	0	0	0	0.0088	-0.02	-0.024	0	0	0.976
-700	0	0	0	-0.017	0	0	0	0.0044	-0.01	-0.017	0	0	0.799
-500	0	0	0	-0.012	0	0	0	0.0022	0	-0.012	0	0	0.560
-300	0	0	0	-0.007	0	0	0	0.0008	0	-0.007	0	0	0.000
-100	0	0	0	-0.002	0	0	0	0	0	-0.002	0	0	1.389
100	0	0	0	0.0024	0	0	0	0	0	0.0024	0	0	1.389
300	0	0	0	0.0071	0	0	0	0.0008	0	0.0071	0	0	0.000
500	0	0	0	0.0118	0	0	0	0.0024	0	0.0118	0	0	0.282
700	0	0	0	0.0166	0	0	0	0.0048	-0.01	0.0165	0	0	0.404
1000	0	0	0	0.0237	0	0	0	0.0101	-0.02	0.0236	0	0	0.282

Table A - 55. Full results of translations and rotations of peg under the influence of moment about the Y-axis.

Moment (Nmm)	Approximation Matrix						Simscape Model						Error (%)
	dx (mm)	dy (mm)	dz (mm)	Rx (Rad)	Ry (Rad)	Rz (Rad)	dx (mm)	dy (mm)	dz (mm)	Rx (Rad)	Ry (Rad)	Rz (Rad)	
-1000	0	0	0	0	-0.024	0	0.0006	-0.009	-0.02	0.0002	-0.024	0	0.560
-700	0	0	0	0	-0.017	0	0.0002	-0.005	-0.01	0	-0.017	0	0.201
-500	0	0	0	0	-0.012	0	0	-0.002	0	0	-0.012	0	0.560
-300	0	0	0	0	-0.007	0	0	-0.001	0	0	-0.007	0	0.000
-100	0	0	0	0	-0.002	0	0	0	0	0	-0.002	0	1.389
100	0	0	0	0	0.002	0	0	0	0	0	0.0024	0	1.389
300	0	0	0	0	0.0071	0	0	-0.001	0	0	0.0071	0	0.000
500	0	0	0	0	0.0118	0	0	-0.002	0	0	0.0119	0	0.560
700	0	0	0	0	0.0166	0	0	-0.005	-0.01	0	0.0166	0	0.201
1000	0	0	0	0	0.0237	0	-0.001	-0.009	-0.02	0.0002	0.0238	0	0.560

Table A - 56. Full results of translations and rotations of peg under the influence of moment about the Z-axis.

Moment (Nmm)	Approximation Matrix						Simscape Model						Error (%)
	dx (mm)	dy (mm)	dz (mm)	Rx (Rad)	Ry (Rad)	Rz (Rad)	dx (mm)	dy (mm)	dz (mm)	Rx (Rad)	Ry (Rad)	Rz (Rad)	
-1000	0	0	0	0	0	-0.036	0	0	-0.01	0	0	-0.036	0.405
-700	0	0	0	0	0	-0.025	0	0	-0.01	0	0	-0.025	0.045
-500	0	0	0	0	0	-0.018	0	0	0	0	0	-0.018	0.125
-300	0	0	0	0	0	-0.011	0	0	0	0	0	-0.011	0.312
-100	0	0	0	0	0	-0.004	0	0	0	0	0	-0.004	1.235
100	0	0	0	0	0	0.0035	0	0	0	0	0	0.0036	1.235
300	0	0	0	0	0	0.0107	0	0	0	0	0	0.0107	0.312
500	0	0	0	0	0	0.0142	0	0	0	0	0	0.0142	0.156
700	0	0	0	0	0	0.0178	0	0	0	0	0	0.0178	0.125
1000	0	0	0	0	0	0.0249	0	0	-0.01	0	0	0.0249	0.045

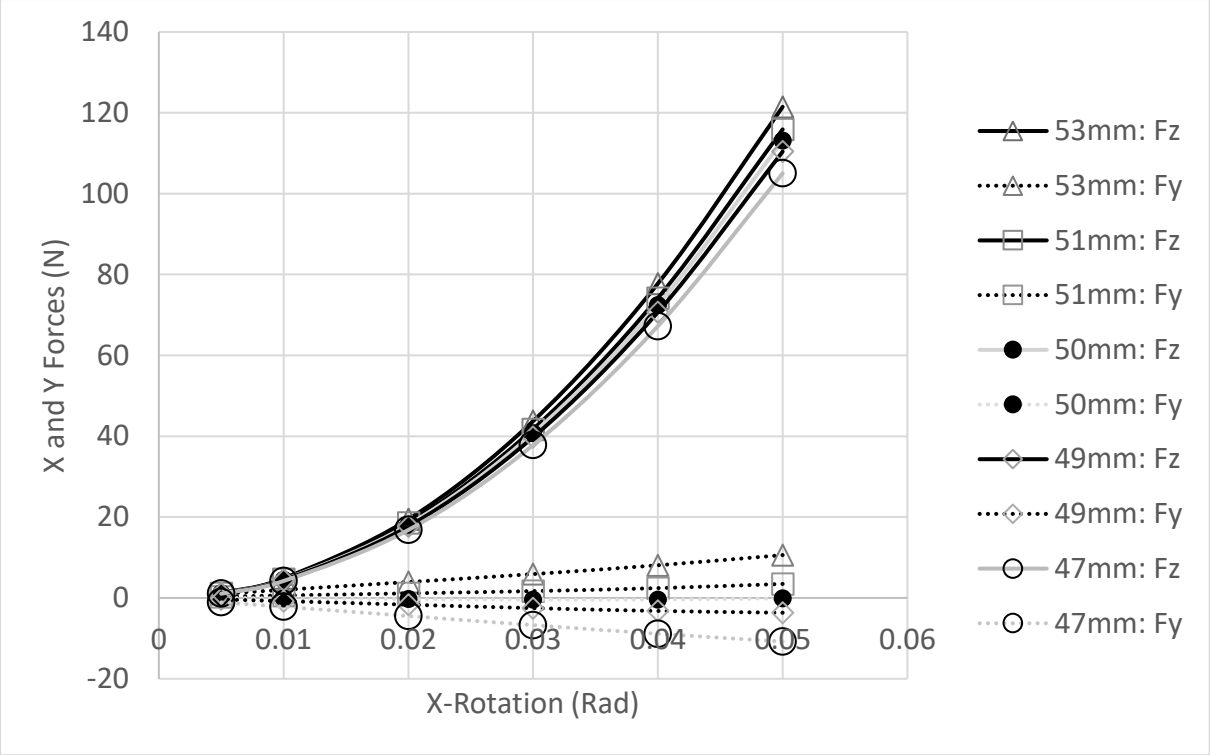

Figure A - 11. Change of forces when the compliance centre is rotated about the X-axis.

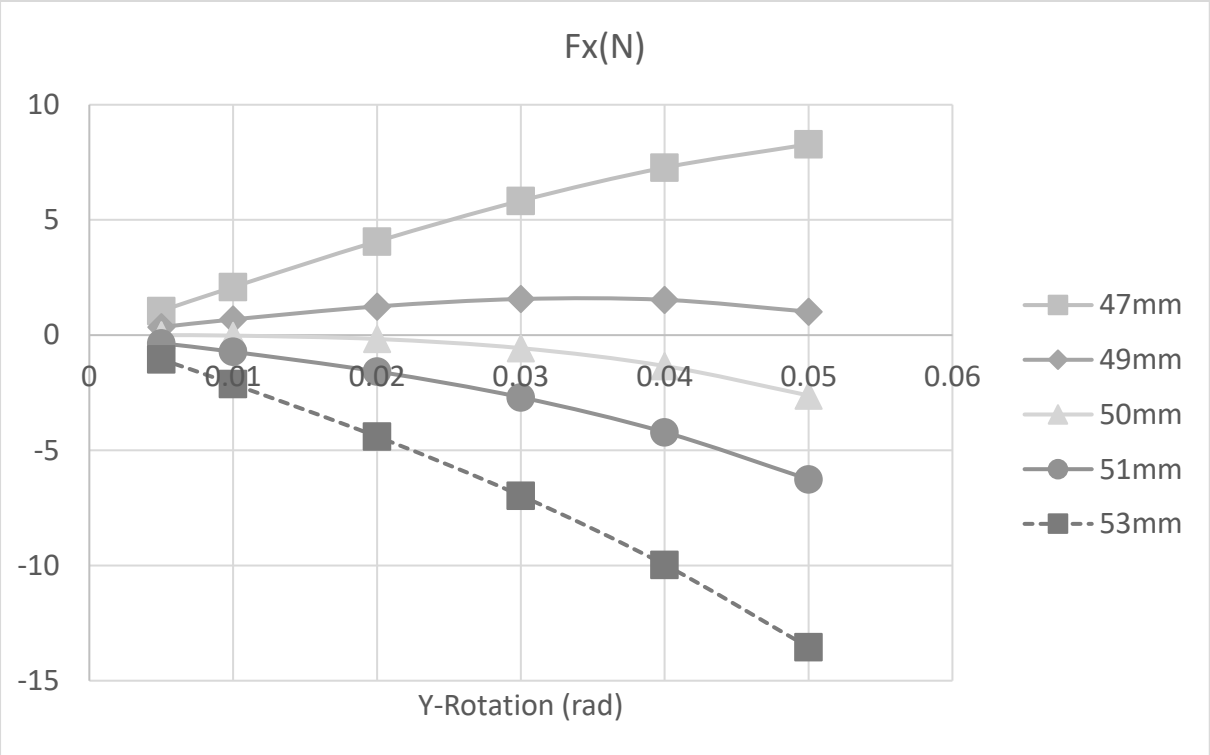

Figure A - 12. Change of X-Forces when the compliance centre is rotated about the Y-axis.

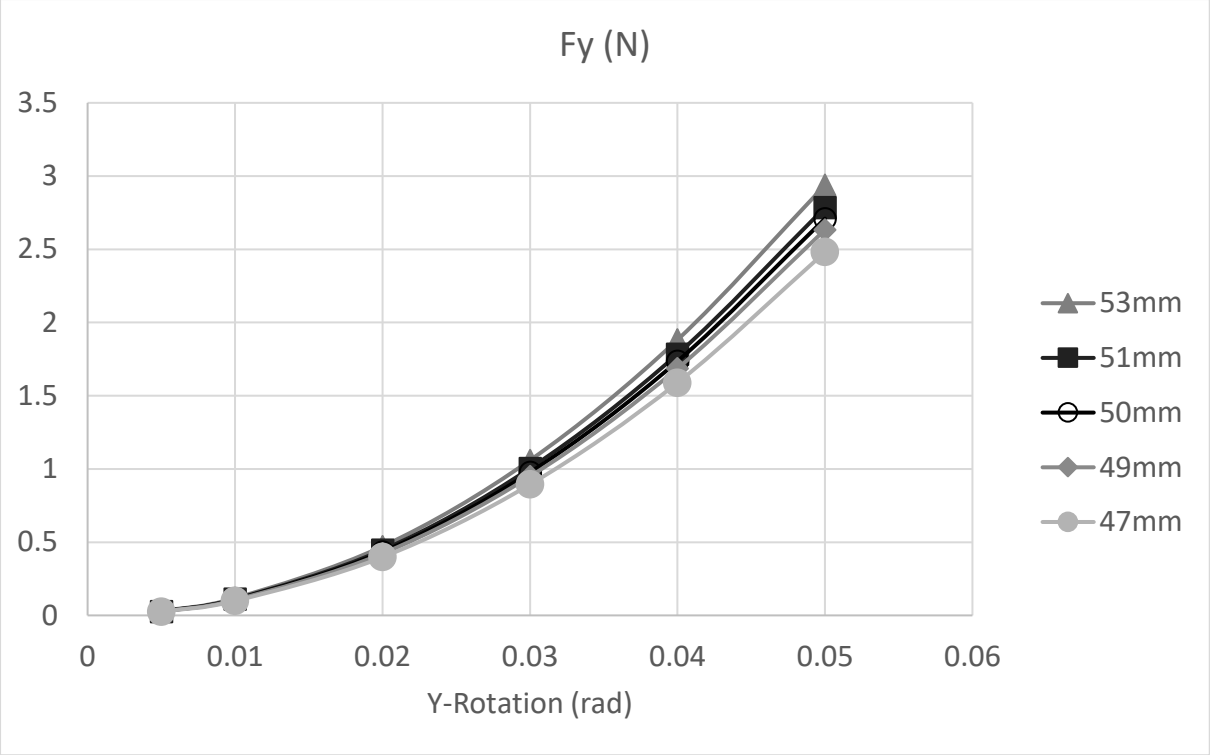

Figure A - 13. Change of Y-Forces when the compliance centre is rotated about the Y-axis.

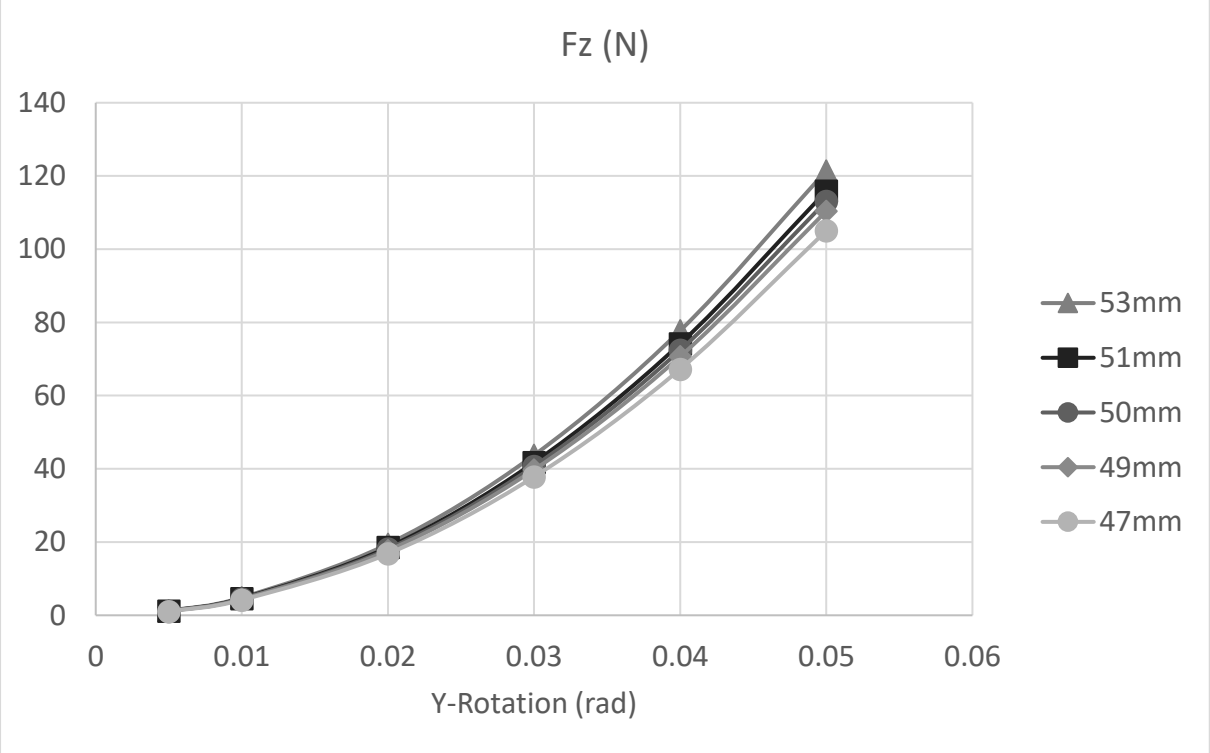

Figure A - 14. Change of Z-Forces when the compliance centre is rotated about the Y-axis.

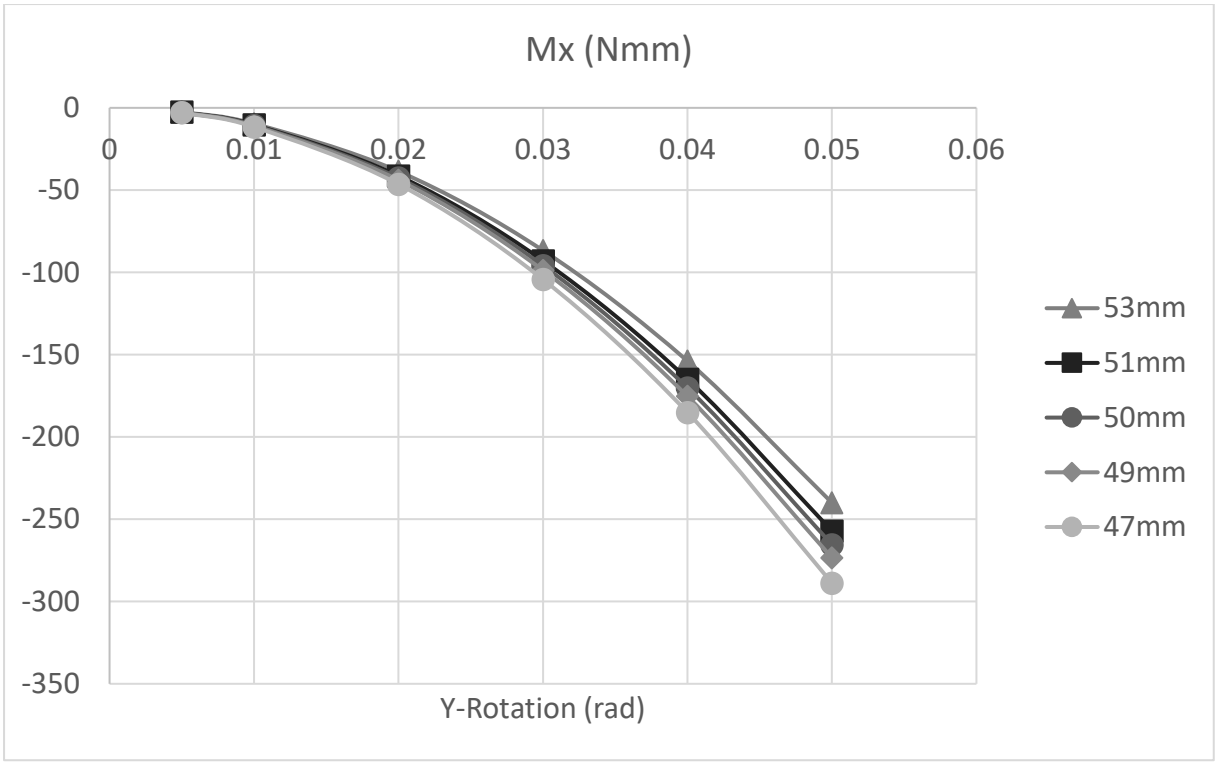

Figure A - 15. Change of X-Moments when the compliance centre is rotated about the Y-axis.

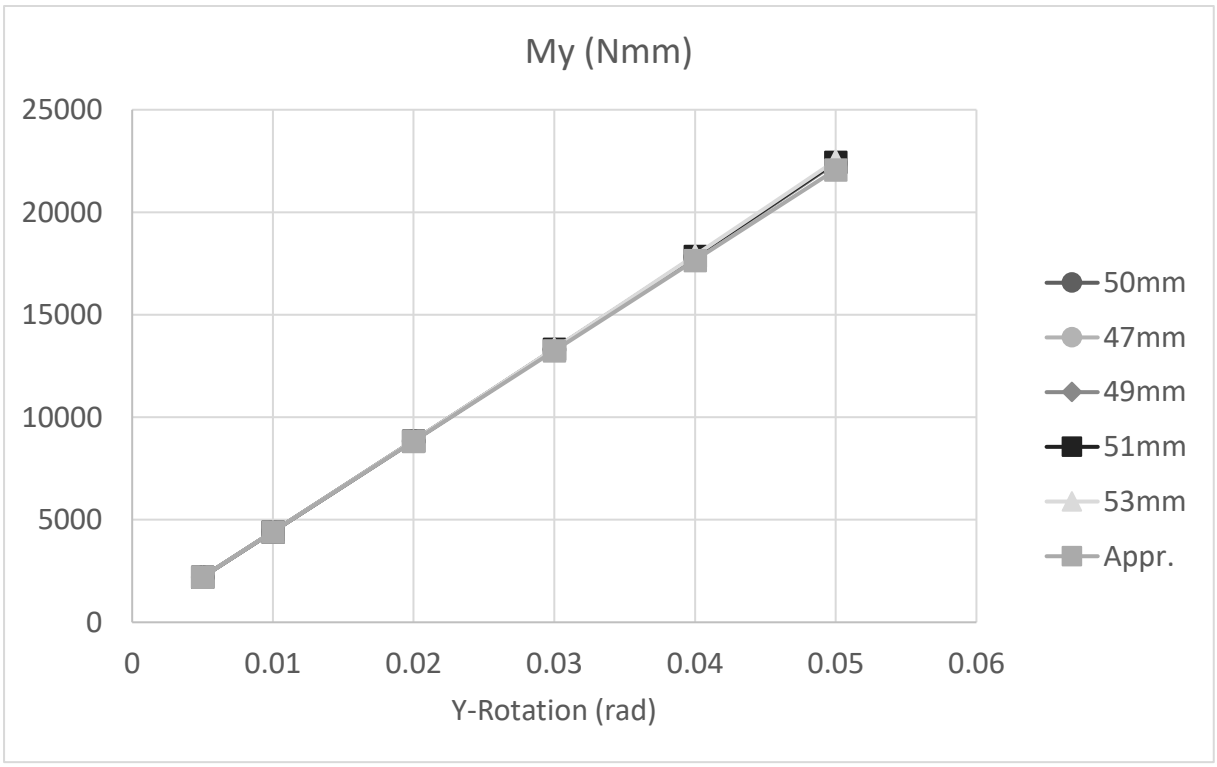

Figure A - 16. Change of Y-Moments when the compliance centre is rotated about the Y-axis.

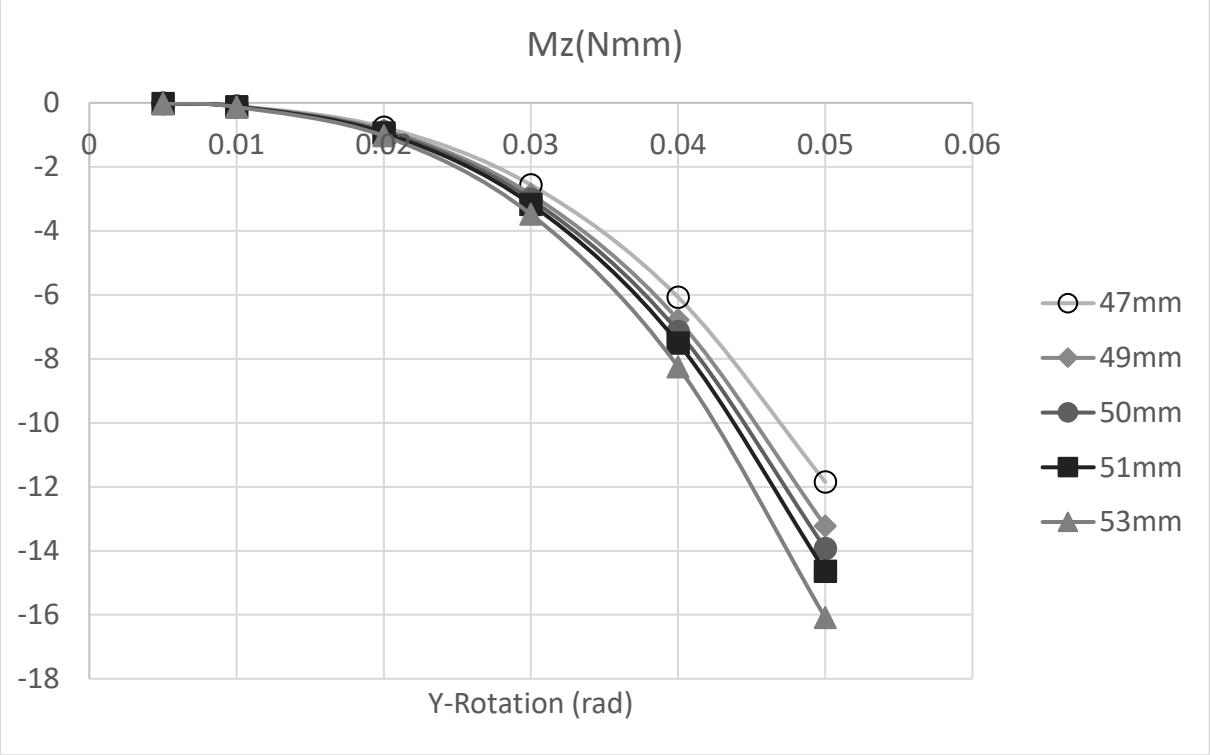

Figure A - 17. Change of Z-Moments when the compliance centre is rotated about the Y-axis.